8-2017

Radio-Frequency Sensors for Detection and Analysis of Chemical and Biological Substances

Yan Cui
Clemson University, cui4@clemson.edu

Recommended Citation

Cui, Yan, "Radio-Frequency Sensors for Detection and Analysis of Chemical and Biological Substances" (2017). *All Dissertations*. 2021.
https://tigerprints.clemson.edu/all_dissertations/2021

RADIO-FREQUENCY SENSORS FOR DETECTION AND ANALYSIS
OF CHEMICAL AND BIOLOGICAL SUBSTANCES

A Dissertation
Presented to
the Graduate School of
Clemson University

In Partial Fulfillment
of the Requirements for the Degree
Doctor of Philosophy
Electrical Engineering

---

by
Yan Cui
August 2017

Accepted by:
Dr. Pingshan Wang, Committee Chair
Dr. Emil Alexov
Dr. Eric G. Johnson
Dr. Goutam Koley
Dr. Guigen Zhang

ABSTRACT

Dielectric spectroscopy (DS) is an important technique for scientific and technological investigations in various areas. DS sensitivity and operating frequency ranges are critical for many applications, including lab-on-chip development where sample volumes are small with a wide range of dynamic processes to probe. In this dissertation, the design and operation considerations of radio-frequency (RF) interferometers that are based on power-dividers (PDs) and quadrature-hybrids (QHs) is presented. The effective quality factor (Q_{eff}) of the sensor is as high as $\sim 3.8 \times 10^6$ with $200 \, \mu$L of water samples. Such interferometers are proposed to address the sensitivity and frequency tuning challenges of current DS techniques. A high-sensitivity and stable QH-based interferometer is demonstrated by measuring glucose-water solution at a concentration level that is ten times lower than some recent RF sensors and DNA solution at $\sim 3 \times 10^{-15}$ mol/mL that is close to the previously reported lowest result while the sample volume is ~1 nL. Composition analysis of ternary mixture solutions are also demonstrated with a PD-based interferometer. Using a tunable liquid attenuator by accurately changing its liquid volume, the sensitivity of a RF interferometer is tuned automatically. The obtained Q_{eff} of the interferometer is up to 1×10^8 at ~5 GHz, i.e., ~100 times higher than previously reported results. When material-under-test, i.e., methanol-water solution in this work, is used for the tuning, a self-calibration and measurement process is demonstrated from 2 GHz to 7.5 GHz at a methanol concentration level down to 5×10^{-5} mole fraction, which is 100 times lower than previously reported results.

A microwave scanning technique is reported for the measurement of floating giant unilamellar vesicles (GUV) in a 25 μm wide and 18.8 μm high microfluidic channel. The measurement is conducted at 2.7 GHz and 7.9 GHz, at which a split ring resonator (SRR) operates at odd modes. A 500 nm wide and 100 μm long SRR split gap is used to scan GUVs that are slightly larger than 25 μm in diameter. The smaller fluidic channel induces flattened GUV membrane sections, which make close contact with the SRR gap surface. The used GUVs are synthesized with POPC (16:0-18:1 PC 1-palmitoyl-2-oleoyl-sn-glycero-3-phosphocholine), SM (16:0 Egg Sphingomyelin) and cholesterol at different molecular compositions. It is shown that SM and POPC bilayers have different dielectric permittivity values, which also change with measurement frequencies. The obtained membrane permittivity values, such as 73.64-j6.13 for POPC at 2.7 GHz, are more than 10 times larger than previously reported results. The discrepancy is likely due to the measurement of dielectric polarization responses that are parallel with, other than perpendicular to, the membrane surface. POPC and SM-rich GUV surface sections are also clearly identified from scanning measurement results. Further work is needed to enable accurate analysis of membrane composition and dynamics at high spatial resolutions.

DEDICATION

This dissertation is dedicated to my parents for their unconditional and unreserved love.

ACKNOWLEDGMENTS

TABLE OF CONTENTS

Table of Contents (Continued)

LIST OF TABLES

List of Tables (Continued)

Table   Page

LIST OF FIGURES

List of Figures (Continued)

List of Figures (Continued)

List of Figures (Continued)

Figure   Page

List of Figures (Continued)

List of Figures (Continued)

List of Figures (Continued)

List of Figures (Continued)

CHAPTER ONE

INTRODUCTION

Dielectric spectroscopy measures the complex permittivity of materials over a

broad frequency range. It is a powerful technique for scientific investigations and

technological developments in various areas, including chemistry, biology and micro-

total-analysis systems (μ-TAS) [1.1]. For chemistry, dielectric spectroscopy between 10^2

and 10^7 Hz has been developed to obtain mobile ion concentration level and ion mobility,

which are of great interest for developing secondary ion batteries and fuel-cell

membranes [1.2]. Dielectric spectroscopy between 1 MHz and 20 GHz has been used to

determine the dielectric constants of imida-zolium-based ionic liquids [1.3], which are

developed as environmentally benign solvents. The dielectric constant values are

important for solvent behavior modeling, which often depends on the dielectric

continuum models of the solvent. Furthermore, dielectric spectroscopy can investigate the

relaxation processes occurring in aqueous solutions in an extremely wide time range.

Thus, it is one of the most important methods for the study of polyelectrolyte-solution

structure and dynamics [1.4], such as the molecular structures of aqueous urea solutions

[1.5]. For biology, dielectric spectroscopy has been used to study the relaxation of DNA

aqueous solutions [1.6], to investigate the collective vibrational modes of proteins, DNAs

and oligonucleotides (from 60 GHz to 2 THz) [1.7], to help understand protein folding

and unfolding processes [1.8], to explore the dynamic processes at the protein-solvent

interface (from 300 kHz to 20 GHz) [1.9], to quantitatively assess the Debye dielectric

model of membrane lipid bi-layers [1.10] and to characterize tissues [1.11]. For μ-TAS

development, such as electronic flow-cytometers [1.12] for single cell detection and identification [1.13], [1.14], dielectric spectroscopy is promising to be a label-free method.

Sensitivity is critical for these applications. The strong interest in minimizing the volume and concentration level of chemical and biomedical samples has further emphasized the need for high sensitivity operations. Small volumes save materials. This is especially important for studying minute amounts of precious samples. Low concentration levels avoid the interactions among analyte molecules, which is important for potentially label-free molecular identifications [1.15] without using additional recognition molecules. Different approaches have been explored to improve sensitivities, including differential measurements of signals from electrode-pairs [1.12] and the development of nanometer electrodes. Among the efforts, resonance based methods achieved higher sensitivities. Examples include the recent planar resonator for single cell capture and measurement [1.16], the resonant circuit for single particle detection and counting [1.17] the resonant filters for biological and chemical sensing [1.18], the resonant structure for femtomolar DNA detection [1.19], the cavity-enabled microwave imaging for DNA sensing [1.20], and the whispering gallery mode resonator for aqueous solution measurement [1.21]. Nevertheless, these devices are still limited in sensitivity since their quality factors are modest except the whispering gallery mode resonators, which have an un-loaded Q as high as $\sim 1.1 \times 10^5$ [1.21]. Yet, the Q values degrade significantly when a lossy sample, e.g., water solutions, are introduced. Besides, dielectric resonators need sophisticated fabrication processes and more complicated

liquid handling procedures. As a result, it is of great interest to develop new and highly sensitive dielectric spectroscopy techniques.

Broadband measurements are also essential for many applications, such as those discussed in the first paragraph. Additionally, the potential resonant absorption of microwaves by molecules and viruses [1.22], [1.23], the potential electrical identification of individual cells [1.15], and the development of microwave microdosimetry [1.24] need broadband RF measurements. Straight transmission lines are very broadband, but with relatively low sensitivity [1.25]; tunable RF resonators [1.11], [1.26], [1.27], harmonic-frequency/multi-mode resonators, and whispering gallery mode resonators [1.28], can operate at a wide frequency range, but their sensitivities are still limited as discussed above.

In Chapter II of this dissertation, a RF interferometer system, which is able to simultaneously tune sensitivity and measurement frequency, as a result, addresses the challenges of current techniques, is proposed and demonstrated. Compared to the previous efforts made by our group [1.29], [1.30], the limited Q_{eff} and mostly operating at a single frequency point can be addressed. In the following chapters, the sensing component in the proposed interferometer system will be replaced by various microwave sensors, i.e, regular coplanar waveguide (CPW), conducted-backed CPW (GCPW), nanometer slotline. In Chapter III, using the proposed interferometer, glucose-water solution at a concentration level 10 times lower than some recent RF sensors [1.31] and pET21a (pE) DNA solution at 10 ng/mL, which is close to the lowest detectable concentration level [1.32], while the used sample volume is ~1 nL are measured by a

3

regular CPW-based sensing structure and its dielectric constant is extracted. Composition analysis of ternary mixture solutions on basis of GCPW or CPW are also demonstrated together. Chapter IV presents a technique that automatically tunes the sensitivity of a radio-frequency (RF) interferometer with a tunable liquid attenuator by accurately changing its liquid volume, which achieves fast measurements, is unnecessary to keep the interferometer stable over a long period of time, i.e., the work in Chapter III, and avoids the use of calibration liquids.

Giant unilamellar vesicles (GUVs) are biologically relevant models that are often used to study cell membrane structures, such as raft-like and non-raft microdomains [1.33], [1.34]. They are also used to study cells, such as red blood cells [1.35]-[1.37]. GUV molecular compositions and interior solutions can be controlled and GUV domain structures are well documented. Thus, GUVs are a good model system for cell sensor examinations. In Chapter V, the GUVs accompanied by different aqueous mediums inside and outside are detected over a range of GHz frequencies using a 100 nm slotline structure, which can concentrate RF fields, up to ~1.76×10^7 V/m, and the complex permittivities of these GUVs are extracted from measured S-parameters.

However, due to the limitation of sensitivity, the information of the lipid bilayer cannot be extracted from the measurement in Chapter V. Lipid plasma membrane heterogeneity, such as sphingomyelin (SM) and cholesterol (Chol)-rich raft-like domains, as shown in Fig. 1.1 [1.38], playing an essential and active role in various cellular functions, e.g., immune signaling [1.39], [1.40], host–pathogen interactions [1.41], [1.42], cancer [1.43], [1.44] and cardiovascular diseases [1.45], [1.46]. The property is also

4

critical for molecular simulation and understanding [1.47], [1.48] of biological membrane

organizations [1.49], dynamics and functions [1.50], [1.51]. It is shown that a small

dielectric property change can lead to significantly different membrane behavior [1.52].

Furthermore, membrane dielectric property determines cell responses to external electric

fields in dielectrophoresis [1.53], impedance spectroscopy [1.54] and electroporation

[1.55], which are important for scientific and technological development.
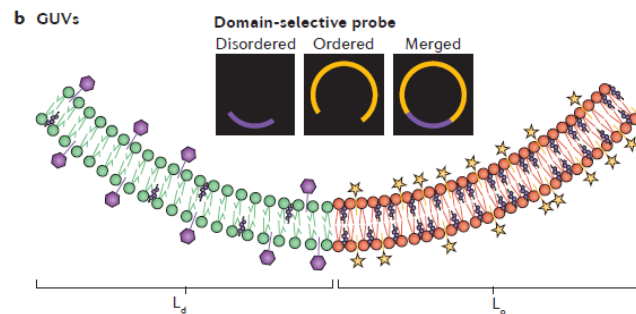
Fig. 1.1 Raft-like domain (Phase L_o) and non-raft domain (Phase L_α) on a fluorescently-
labeled GUV [1.38].

A commonly used technique for membrane dielectric property measurement is

scanning probe microscopy (SPM), which includes electrostatic force microscopy [1.56]-

[1.60] and microwave microscopy [1.61]. The technique has nanoscale resolution, and is

promising for investigating nanoscale dynamic membrane organizations, such as rafts

[1.62]. Nevertheless, SPM measurements are often conducted with supported lipid

bilayers in air, and only recently in aqueous solution [1.56]. In force-based measurement,

charges on membranes, among other factors, complicate data interpretation. The

microwave microscopy needs cell fixation [1.63] while its probe moves. The supporting substrate and the fixation process are likely to induce significant dielectric property changes in lipid bilayers and cell membranes. Other measurement methods include impedance spectroscopy [1.64], environment-sensitive fluorescent microscopy [1.65], electron paramagnetic resonance (EPR) [1.66], imaging ellipsometry [1.67], interferometry [1.68], and dielectrophoretic spectroscopy [1.69]. These less commonly used methods may also need supported membranes or fixed cells. Measuring floating cells and model membranes, such as a giant unilamellar vesicle (GUV), in native or near native environment is still a challenge [1.70]. In this work, we demonstrate a microwave technique to scan and quantify the dielectric property of floating GUV membranes in aqueous solution. We also show that the technique can clearly measure GUV membrane structures.

References

[1.1] F. Kremer and A. Schoönhals, *Broadband Dielectric Spectroscopy*. New York, NY: Springer, 2003, pp. 35-37.

[1.2] R. J. Klein, S. Zhang, S. Dou, B. H. Jones, R. H. Colby, and J. Runt, "Modeling electrode polarization in dielectric spectroscopy: Ion mobility and mobile ion concentration of single-ion polymer electrolytes," *J. Chem. Phys.*, vol. 124, no. 14, pp. 144903, Apr. 2006.

[1.3] C. Wakai, A. Oleinikova, M. Ott, and H. Weingartner, "How polar are ionic liquids? Determination of the static dielectric constant of an imidazolium-based ionic liquid by microwave dielectric spectroscopy," *J. Phys. Chem. B*, vol. 109, no. 36, pp. 17028-17030, Aug. 2005.

[1.4] F. Bordi, C. Cametti, and R. H. Colby, "Dielectric spectroscopy and conductivity of polyelectrolyte solutions," *J. Phys.: Condens. Matter*, vol. 16, no. 49, pp. R1423-R1463, Nov. 2004.

[1.5] Y. Hayashi, Y. Katsumoto, S. Omori, N. Kishii, and A. Yasuda, "Liquid structure of the urea-water system studied by dielectric spectroscopy," *J. Phys. Chem. B*, vol. 111, no. 5, pp. 1076-1080, Jan. 2007.

[1.6] S. Tomić, S. D. Babić, T. Vuletić, S. Krča, D. Ivanković, L. Griparić, and R. Podgornik, "Dielectric relaxation of DNA aqueous solutions," *Phys. Rev. E*, vol. 75, no. 2, pp. 021905, Feb. 2007.

[1.7] A. G. Markelz, A. Roitberg, and E. J. Heilweil, "Pulsed terahertz spectroscopy of DNA, bovine serum albumin and collagen between 0.1 and 2.0 THz," *Chem. Phys. Lett.*, vol. 320, no. 1, pp. 42-48, Mar. 2000.

[1.8] K. M. Taylor and D. W. van der Weide, "Ultra-sensitive detection of protein thermal unfolding and refolding using near-zone microwaves," *IEEE Trans. Microwave Theory and Techn.*, vol. 53, no. 5, pp. 1576-1586, May. 2005.

[1.9] A. Oleinikova, P. Sasisanker, and H. Weingertner, "What can really be learned from dielectric spectroscopy of protein solutions? A case study of ribonuclease A," *J. Phys. Chem. B*, vol. 108, no. 24, pp. 8467-8474, May. 2004.

[1.10] C. Merla, M. Liberti, F. Apollonio, and G. D'Inzeo, "Quantitative assessment of dielectric parameters for membrane lipid bi-layers from RF permittivity measurements," *Bioelectromagnetics*, vol. 30, no. 4, pp. 286-298, May. 2009.

[1.11] D. Popovic, L. McCartney, C. Beasley, M. Lazebnik, M. Okoniewski, S. C. Hagness, and J. H. Booske, "Precision open-ended coaxial probes for in vivo and ex vivo dielectric spectroscopy of biological tissues at microwave frequencies," *IEEE Trans. Microwave Theory and Techn.*, vol. 53, no. 5, pp. 1713-1722, May. 2005.

[1.12] S. Gawad, L. Schild, and P. Renaud, "Micromachined impedance spectroscopy flow cytometer for cell analysis and particle sizing," *Lab Chip*, vol. 1, no. 1, pp. 76-82, Aug. 2001.

[1.13] H. Morgan, T. Sun, D. Holmes, S. Gawad, and N. G. Green, "Single cell dielectric spectroscopy," *J. Phys. D: Appl. Phys.*, vol. 40, no. 1, pp. 61-70, Jan. 2007.

[1.14] D. M. Vykoukal, P. R. C. Gascoyne, and J. Vykoukal, "Dielectric characterization of complete mononuclear and polymorphonuclear blood cell subpopulations for label-free discrimination," *Integr. Biol.*, vol. 1, no. 7, pp. 477-484, Jun. 2009.

[1.15] T. H. Basey-Fisher, S. M. Hanham, H. Andresen, S. A. Maier, M. M. Stevens, N. M. Alford, and N. Klein, "Microwave Debye relaxation analysis of dissolved proteins: Towards free-solution biosensing," *Appl. Phys. Lett.*, vol. 99, no. 23, pp. 233703, Dec. 2011.

[1.16] T. Chretiennot, D. Dubuc, and K. Grenier, "A microwave and microfluidic planar resonator for efficient and accurate complex permittivity characterization of aqueous solutions," *IEEE Trans. Microwave Theory and Techn.*, vol. 61, no. 2, pp. 972-978, Feb. 2013.

[1.17] C. Dalmay, M. Cheray, A. Pothier, F. Lalloué, M. O. Jauberteau, and P. Blondy, "Ultra sensitive biosensor based on impedance spectroscopy at microwave frequencies for cell scale analysis," *Sens. Actuators A-Phys.*, vol. 162, no. 2, pp. 189-197, Aug. 2010.

[1.18] F. Costa, C. Amabile, A. Monorchio, and E. Prati, "Waveguide dielectric permittivity measurement technique based on resonant FSS filters," *IEEE Microw. Wireless Compon. Lett.*, vol. 21, no. 5, pp. 273-275, May. 2011.

[1.19] M. Nagel, P. H. Bolivar, M. Brucherseifer, H. Kurz, A. Bosserhoff, and R. Büttner, "Integrated planar terahertz resonators for femtomolar sensitivity label-free detection of DNA hybridization," *Appl. Opt.*, vol. 41, no. 10, pp. 2074-2078, Apr. 2002.

[1.20] B. Friedman, M. A. Gaspar, S. Kalachikov, K. Lee, R. Levicky, G. Shen, and H. Yoo, "Sensitive, label-free DNA diagnostics based on near-field microwave imaging," *J. Am. Chem. Soc.*, vol. 127, no. 27, pp. 9666-9667, Jun. 2005.

[1.21] E. N. Shaforost, N. Klein, S. A. Vitusevich, A. A. Barannik, and N. T. Cherpak, "High sensitivity microwave characterization of organic molecule solutions of nanoliter volume," *Appl. Phys. Lett.*, vol. 94, no. 11, pp. 112901, Mar. 2009.

[1.22] T.-M. Liu, H.-P. Chen, L.-T. Wang, J.-R. Wang, T.-N. Luo, Y.-J. Chen, S.-I. Liu, and C.-K. Sun, "Microwave resonant absorption of viruses through dipolar coupling with confined acoustic vibrations," *Appl. Phys. Lett.*, vol. 94, no. 4, pp. 043902, Jan. 2009.

[1.23] R. K. Adair, "Vibrational resonances in biological systems at microwave frequencies," *Biophy. J.*, vol. 82, no. 3, pp. 1147-1152, Mar. 2002.

[1.24] C. Merla, M. Liberti, F. Apollonio, C. Nervi, and G. D'Inzeo, "A 3-D microdosimetric study on blood cells: A permittivity model of cell membrane and stochastic electromagnetic analysis," *IEEE Trans. Microwave Theory and Techn.*, vol. 58, no. 3, pp. 691-698, Mar. 2010.

[1.25] J. C. Booth, N. D. Orloff, J. Mateu, M. Janezic, M. Rinehart, and J. A. Beall, "Quantitative permittivity measurements of nanoliter liquid volumes in microfluidic channels to 40 GHz," *IEEE Trans. Instrum. Meas.*, vol. 59, no. 12, pp. 3279-3288, Dec. 2010.

[1.26] A. T. Findikoglu, Q. X. Jia, I. H. Campbell, X. D. Wu, D. Reagor, C. B. Mombourquette, and D. McMurry, "Electrically tunable coplanar transmission line resonators using YBaCuO/SrTiO bilayers," *Appl. phys. lett.*, vol. 66, no. 26, pp. 3674-3676, Jun. 1995.

[1.27] X. Liu, L. P. B. Katehi, W. J. Chappell, and D. Peroulis, "High-Q Tunable Microwave cavity resonators and filters using SOI-based RF MEMS tuners," *J. Microelectromech. Syst.*, vol. 19, no. 4, pp. 774-784, Aug. 2010.

[1.28] G. Annino, D. Bertolini, M. Cassettari, M. Fittipaldi, I. Longo, and M. Martinelli, "Dielectric properties of materials using whispering gallery dielectric resonators: Experiments and perspectives of ultra-wideband characterization," *J. Chem. Phys.*, vol. 112, no. 5, pp. 2308-2314, Feb. 2000.

[1.29] C. Song and P. Wang, "A radio frequency device for measurement of minute dielectric property changes in microfluidic channels," *Appl. Phys. Lett.*, vol. 94, no. 2, pp. 023901, 2009.

[1.30] Y. Yang, H. Zhang, J. Zhu, G. Wang, T. R. Tzeng, X. Xuan, K. Huang, and P. Wang, "Distinguishing the viability of a single yeast cell with an ultra-sensitive radio frequency sensor," *Lab Chip*, vol. 10, no. 5, pp. 553-555, Jan. 2010.

[1.31] M. Hofmann, G. Fischer, R. Weigel, and D. Kissinger, "Microwave-based noninvasive concentration measurements for biomedical applications," *IEEE Trans. Microwave Theory and Techn.*, vol. 61, no. 5, pp. 2195-2204, May. 2013.

[1.32] I. F. Cheng, S. Senapati, X. Cheng, S. Basuray, H.-C. Chang, and H.-C. Chang, "A rapid field-use assay for mismatch number and location of hybridized DNAs," *Lab Chip*, vol. 10, no. 7, pp. 828-831, Feb. 2010.

[1.33] M. Edidin, "The state of lipid rafts: from model membranes to cells," *Annu. Rev. Biophys. Biomol. Struct.*, vol. 32, pp. 257-283, Jan. 2003.

[1.34] C. A. Day and A. K. Kenworthy, "Tracking microdomain dynamics in cell membranes," *Biochim. Biophys. Acta.-Biom.*, vol. 1788, no. 1, pp. 245-253, Nov. 2009.

[1.35] P. M. Vlahovska, T. Podgorski, and C. Misbah, "Vesicles and red blood cells in flow: From individual dynamics to rheology," *C. R. Physique*, vol. 10, no. 8, pp. 775-789, Nov. 2009.

[1.36] P. M. Vlahovska, D. Barthes-Biesel, and C. Misbah, "Flow dynamics of red blood cells and their biomimetic counterparts," *C. R. Physique*, vol. 14, no. 6, pp. 451-458, Jun.-July. 2013.

[1.37] X. Li, P. M. Vlahovska, and G. E. Karniadakis, "Continuum-and particle-based modeling of shapes and dynamics of red blood cells in health and disease," *Soft Matter*, vol. 9, pp. 28-37, Oct. 2013.

[1.38] E. Sezgin, I. Levental, S. Mayor, and C. Eggeling, "The mystery of membrane organization: composition, regulation and roles of lipid rafts," *Nat. Rev. Mol. Cell. Biol.*, pp. 1471-0080, Mar. 2017.

[1.39] K. A. Field, D. Holowka, and B. Baird, "Fc epsilon RI-mediated recruitment of p53/56lyn to detergent-resistant membrane domains accompanies cellular signaling," *Proc. Natl Acad. Sci. USA*, vol. 92, no. 20, pp. 9201-9205, Sep. 1995.

[1.40] P. Varshney, V. Yadav, and N. Saini, "Lipid rafts in immune signaling: current progress and future perspective," *Immunology*, vol. 149, no. 1, pp. 13-24, Sep. 2016.

[1.41] M. Lorizate, T. Sachsenheimer, B. Glass, A. Habermann, M. J. Gerl, H. G. Kräusslich, B. Brügger, "Comparative lipidomics analysis of HIV-1 particles and their producer cell membrane in different cell lines," *Cell. Microbiol.*, vol. 15, no. 2, pp. 292-304, Feb. 2013.

[1.42] R. A. Dick, S. L. Goh, G. W. Feigenson, and V. M. Vogt, "HIV-1 Gag protein can sense the cholesterol and acyl chain environment in model membranes," *Proc. Natl Acad. Sci. USA*, vol. 109, no. 46, pp. 18761-18766, Nov. 2012.

[1.43] H. Raghu, P. K. Sodadasu, R. R. Malla, C. S. Gondi, N. Estes, and J. S Ra, "Localization of uPAR and MMP-9 in lipid rafts is critical for migration, invasion and angiogenesis in human breast cancer cells," *BMC Cancer*, vol. 10, pp. 647, Nov. 2010.

[1.44] J. B. Larsen, M. B. Jensen, V. K Bhatia, S. L Pedersen, T. Bjørnholm, L. Iversen, M. Uline, I. Szleifer, K. J Jensen, N. S Hatzakis, and D. Stamou, "Membrane curvature enables N-Ras lipid anchor sorting to liquid-ordered membrane phases," *Nat. Chem. Biol.*, vol. 11, pp. 192-194, Jan. 2015.

[1.45] A. Maguy, T. E. Hebert, and S. Nattel, "Involvement of lipid rafts and caveolae in cardiac ion channel function," *Cardiovasc. Res.*, vol. 69, no. 4, pp. 798-807, Mar. 2006.

[1.46] F. J. O. Rios, M. Ferracini, M. Pecenin, M. M. Koga, Y. Wang, D. F. J. Ketelhuth, and S. Jancar, "Uptake of oxLDL and IL-10 production by macrophages requires PAFR and CD36 recruitment into the same lipid rafts," *PLoS ONE*, vol. 8, no. 10, pp. e76893, Oct. 2013.

[1.47] S. Tanizaki and M. Feig, "A generalized Born formalism for heterogeneous dielectric environments: application to the implicit modeling of biological membranes," *J. Chem. Phys.*, vol. 122, no. 12, pp. 124706, Mar. 2005.

[1.48] A. P. Lyubartsev and A. L. Rabinovich, "Force field development for lipid membrane simulations," *Biochim. Biophys. Acta*, vol. 1858, no. 10, pp. 2483-2497, Oct. 2016.

[1.49] H. I. Ingólfsson, M. N. Melo, F. J. van Eerden, C. m. Arnarez, C. A. Lopez, T. A. Wassenaar, X. Periole, A. H. de Vries, D. P. Tieleman, and S. J. Marrink, "Lipid organization of the plasma membrane," *J. Am. Chem. Soc.*, vol. 136, no. 41, pp. 14554-14559, Sep. 2014.

[1.50] C. Hofsäß, E. Lindahl, and O. Edholm, "Molecular dynamics simulations of phospholipid bilayers with cholesterol," *Biophys. J.*, vol. 84, no. 4, pp. 2192-2206, Apr. 2003.

[1.51] K. Pluhackova, S. A. Kirsch, J. Han, L. Sun, Z. Jiang, T. Unruh, and R. A. Böckmann, "A critical comparison of biomembrane force fields: structure and dynamics of model DMPC, POPC, and POPE bilayers," *J. Phys. Chem. B*, vol. 120, no. 16, pp. 3888-3903, Apr. 2016.

[1.52] M. Patra, M. Karttunen, M. T. Hyvönen, E. Falck, and I. Vattulainen, "Lipid bilayers driven to a wrong lane in molecular dynamics simulations by subtle changes in long-range electrostatic interactions," *J. Phys. Chem. B*, vol. 108, no. 14, pp. 4485-4494, Mar. 2004.

[1.53] P. R. Gascoyne, S. Shim, J. Noshari, F. F. Becker, and K. Stemke-Hale, "Correlations between the dielectric properties and exterior morphology of cells revealed by dielectrophoretic field-flow fractionation," *Electrophoresis*, vol. 34, no.7, pp. 1042-1050, Apr. 2013.

[1.54] A. Valero, T. Braschler, and P. Renaud, "A unified approach to dielectric single cell analysis: Impedance and dielectrophoretic force spectroscopy," *Lab. Chip.*, vol. 10, pp. 2216-2225, Jul. 2010.

[1.55] T. Y. Tsong, "Electroporation of cell membranes," *Biophys. J.*, vol. 60, no. 2, pp. 297-306, Aug. 1991.

[1.56] G. Gramse, A. Dols-Perez, M.A. Edwards, L. Fumagalli, and G. Gomila, "Nanoscale measurement of the dielectric constant of supported lipid bilayers in aqueous solutions with electrostatic force microscopy," *Biophys. J.*, vol. 104, no. 6, pp. 1257-1262, Mar. 2013.

[1.57] L. Fumagalli, G. Ferrari, M. Sampietro, and G. Gomila, G, "Quantitative nanoscale dielectric microscopy of single-layer supported biomembranes," *Nano. Lett.*, vol. 9, no. 4, 1604-1608, Mar. 2009.

[1.58] G. Gramse, I. Casuso, J. Toset, L. Fumagalli, and G. Gomila, "Quantitative dielectric constant measurement of thin films by DC electrostatic force microscopy," *Nanotechnology*, vol. 20, no. 39, pp. 395702, Sep. 2009.

[1.59] G. Gramse, M. Edwards, L. Fumagalli, and G. Gomila, "Dynamic electrostatic force microscopy in liquid media," *Appl. Phys. Lett.*, vol. 101, no. 21, pp. 213108, Nov. 2012.

[1.60] L. Collins, A. Belianinov, S. Somnath, B. J. Rodriguez, N. Balke, S. V. Kalinin, and S. Jesse, "Multifrequency spectrum analysis using fully digital G Mode-Kelvin probe force microscopy," *Nanotechnology*, vol. 27, no. 10, pp. 105706, Feb. 2016.

[1.61] G. Gramse, M. Kasper, L. Fumagalli, G. Gomila, P. Hinterdorfer, and F. Kienberger, "Calibrated complex impedance and permittivity measurements with scanning microwave microscopy," *Nanotechnology*, vol. 25, no. 14, pp. 145703, Mar. 2014.

[1.62] E. Klotzsch and G. J. Schütz, "A critical survey of methods to detect plasma membrane rafts," *Phil. Trans. R. Soc. B*, vol. 368, no. 1611, pp. 20120033, Feb. 2013.

[1.63] M. C. Biagi, R. Fabregas, G. Gramse, M. Van Der Hofstadt, A. Juárez, F. Kienberger, L. Fumagalli, and G. Gomila, "Nanoscale electric permittivity of single bacterial cells at gigahertz frequencies by scanning microwave microscopy," *ACS nano*, vol. 10, no. 1, pp. 280-288, Jan. 2016.

[1.64] H. G. Coster, T. C. Chilcott, and A. C. Coster, "Impedance spectroscopy of interfaces, membranes and ultrastructures," *Bioelectrochem. Bioenerg.*, vol. 40, no. 1, pp. 79-98, Oct. 1996.

[1.65] A. P. Demchenko, Y. Mély, G. Duportail, and A. S. Klymchenko, "Monitoring biophysical properties of lipid membranes by environment-sensitive fluorescent probes," *Biophys. J.*, vol. 96, no. 9, pp. 3461-3470, May 2009.

[1.66] D. Kurad, G. Jeschke, and D. Marsh, "Lipid membrane polarity profiles by high-field EPR," *Biophys. J.*, vol. 85, no. 2, pp. 1025-1033, Aug. 2003.

[1.67] M. C. Howland, A. W. Szmodis, B. Sanii, and A. N. Parikh, "Characterization of physical properties of supported phospholipid membranes using imaging ellipsometry at optical wavelengths," *Biophys. J.*, vol. 92, no. 4, pp. 1306-1317, Feb. 2007.

[1.68] D. F. Kienle, J. V. de Souza, E. B. Watkins, and T. L. Kuhl, "Thickness and refractive index of DPPC and DPPE monolayers by multiple-beam interferometry," *Anal. Bioanal. Chem.*, vol. 406, no. 19, pp. 4725-4733, Jul. 2014.

[1.69] B. P. Lynch, A. M. Hilton, and G. J. Simpson, "Nanoscale dielectrophoretic spectroscopy of individual immobilized mammalian blood cells," *Biophys. J.*, vol. 91, no. 7, pp. 2678-2686, Oct. 2006.

[1.70] M. Patra, M. Karttunen, M. T. Hyvönen, E. Falck, P. Lindqvist, and I. Vattulainen, "Molecular dynamics simulations of lipid bilayers: major artifacts due to truncating electrostatic interactions," *Biophys. J.*, vol. 84, no. 6, pp. 3636-3645, Jan. 2003.

CHAPTER TWO

ULTRA-SENSITIVE AND TUNABLE RADIO-FREQUENCY INTERFEROMETER

2.1 Dielectric Permittivity Spectroscopy

Permittivity measurement of dielectric materials over a broad frequency range is a powerful technique for scientific and technological investigations in chemistry, biology and micro-total-analysis systems (μ-TAS). When a dielectric material is exposed to an electric field $\vec{E}$, nuclei (positive charges) and electron clouds (negative charges) in individual atoms, as shown in Fig. 2.1 [2.1], and electric dipole moments in molecules separate from one another along the direction of $\vec{E}$. Dielectric permittivity ε is defined as the ratio between the electric field $\vec{E}$ within a material and the corresponding electric displacement $\vec{D}$.

$$\vec{D} = \varepsilon\vec{E} = \varepsilon_0 \varepsilon_r \vec{E} \qquad (2.1)$$

Here, ε_0=8.8541878176$\times$10^{-12} F/m is the permittivity of free-space, and ε_r is defined to the relative permittivity characterizing the dielectric properties of materials.
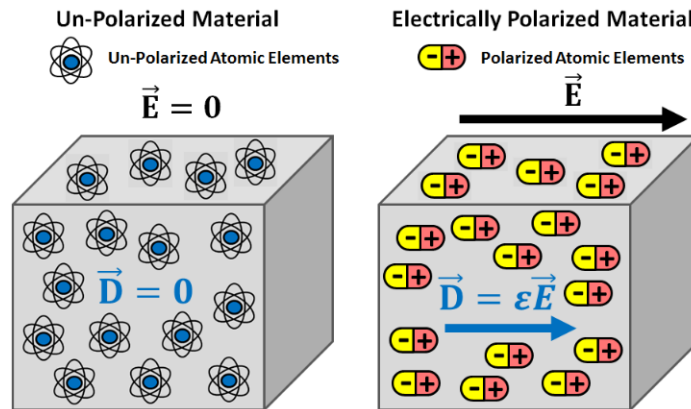
Fig. 2.1 Un-polarized and polarized atomic elements [2.1].

For an applied electric field with high frequency f, the above electric polarization depends on the frequency, and the dielectric permittivity is expressed below as a complex number $\varepsilon^*(\omega)$.

$$\varepsilon^*(\omega) = \varepsilon'(\omega) + j\varepsilon''(\omega) \qquad (2.2)$$

Here, the angular frequency ω is defined by $2\pi f$, the real component $\varepsilon'(\omega)$ of the dielectric permittivity represents energy stored through electrical polarization whereas the imaginary component $\varepsilon''(\omega)$ represents a measure of energy loss. The frequency-dependent dielectric permittivity $\varepsilon^*(\omega)$ is also described by the following model [2.2].

$$\varepsilon^*(\omega) = \varepsilon_\infty + \sum_{j=1}^{n} \frac{\varepsilon_{0j} - \varepsilon_{\infty j}}{[1 + (j\omega\tau_j)^{\beta_j}]^{\alpha_j}} \qquad (2.3)$$

In eq. (2.3), ε_∞ represents a limit as frequency goes to infinity, ε_0 represents the zero-frequency permittivity, τ is the dielectric relaxation time, j represents the jth process, α and β are the shape parameters representing asymmetric and symmetric distribution of relaxation times, respectively. Equation (2.3) includes some following cases: (*i*) the Debye (D1) when $\alpha_j = \beta_j = 1$, $n=1$; (*ii*) the Cole-Cole (CC1) when $\alpha_j = 1$, $0 < \beta_j \leq 1$, $n=1$; (*iii*) the Davidson-Cole (DC1), when $0 < \alpha_j \leq 1$, $\beta_j = 1$, $n=1$; (*iv*) the Havriliak-Negami (HN1) when $0 < \alpha_j \leq 1$, $0 < \beta_j \leq 1$, $n=1$; (*v*) the double-Debye (D2) when $\alpha_j = \beta_j = 1$, $n=2$; (*vi*) the double Cole-Cole (CC2) when $\alpha_j = 1$, $0 < \beta_j \leq 1$, $n=2$; and so on. For example, the dielectric permittivity spectroscopy of methanol-water mixture at 0.01 mole fraction can be described by the CC2. Using the data in [2.2], it can be drawn as:
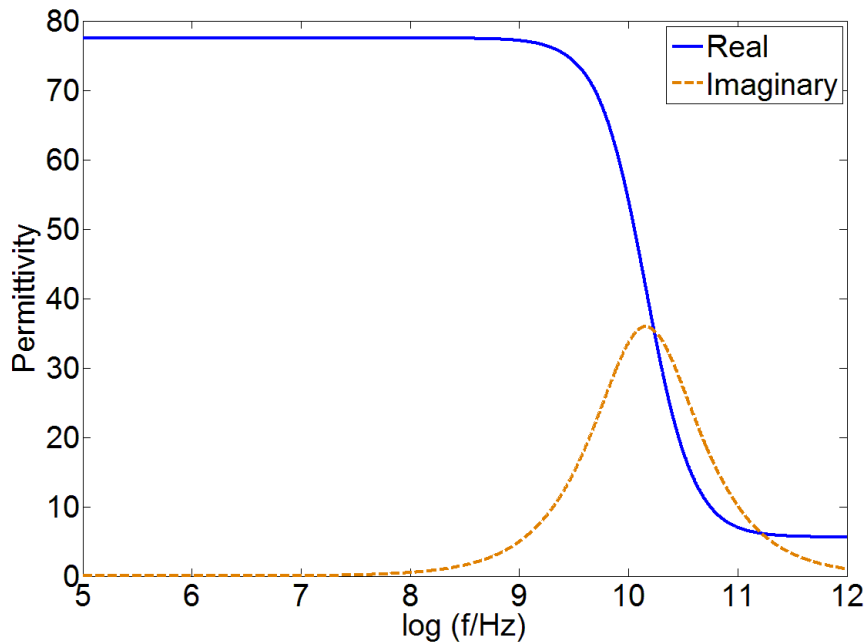
Fig. 2.2 Dielectric permittivity spectroscopy of methanol-water mixture (0.05 mole fraction) from 10^5 Hz (0.1 MHz) to 10^{12} Hz (1 THz). Blue line: real component; green line: imaginary component.

From Fig. 2.2, we can see that (*i*) at low frequency (<10 MHz), the complex permittivity is mainly determined by the real component, and the imaginary one is close to zero; (*ii*) from several hundreds of MHz to 100 GHz (the microwave frequency range), the real and imaginary components have strong frequency-dependency; (*iii*) at high frequency (several hundreds of GHz), the real one is close to 6 and keeps almost consistent, and the imaginary becomes back to zero. These features caused by structural reorientation of polar molecules [2.3] are also applied to other concentration levels and aqueous solutions, e.g., 1-propanol [2.4], 2-propanol [2.5]-[2.6], ethanol [2.7], DNA

[2.8]-[2.9], protein [2.10], glucose [2.11], and so on. As a result, the dielectric permittivity spectroscopy in the microwave regime is of brilliant prospects for the detection and analysis of chemical and biological substances at low-concentration and without fluorescent labels involved.

2.2 Interferometer Design and Operation

Figure 2.3 is the schematic of the proposed radio-frequency (RF) interferometer. Three frequency bands are combined to cover 3-decades of operating frequencies. The detailed arrangement of band *II* is illustrated. Compared with the devices in [2.12]-[2.15], off-chip tuning components are introduced for continuous adjustments of phase (Φ) and attenuation (R). Broadband off-chip power dividers are also used. Band *III* has similar configurations. For band *I*, coaxial cables, instead of phase shifter Φ, are used to provide 180° phase shifts at the fundamental and certain harmonic frequency points. The yellow sensing sections are built with 50 Ω conducted-backed coplanar waveguides (GCPW), which are fabricated with Duroid 5870 laminates using the milling machine shown in Fig. 2.4. They will be replaced by other sensing structures in the following chapters. Polydimethylsiloxane (PDMS) wells are attached to the GCPWs to hold reference (REF) and material-under-test (MUT) solutions. The dimensions of the GCPWs and PDMS wells are shown in Fig. 2.5. As a frequently-used polymeric material in this dissertation, the fabrication process and the limitation of PDMS will be introduced in Section 2.5.
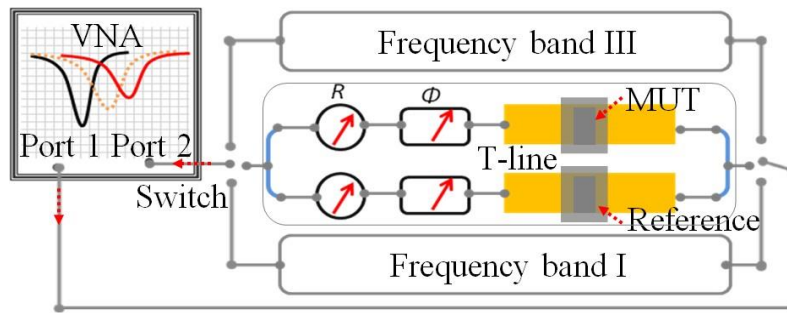
Fig. 2.3 Schematic of the proposed RF sensor setup. Two switches are used to combine

the operations of three frequency-bands. Band *I*: from ~20 MHz to ~1 GHz; band *II*: from

~1 GHz to ~12.5 GHz, band *III*: from ~26.5 GHz to ~38 GHz. Manual tuning

components are used in this work.
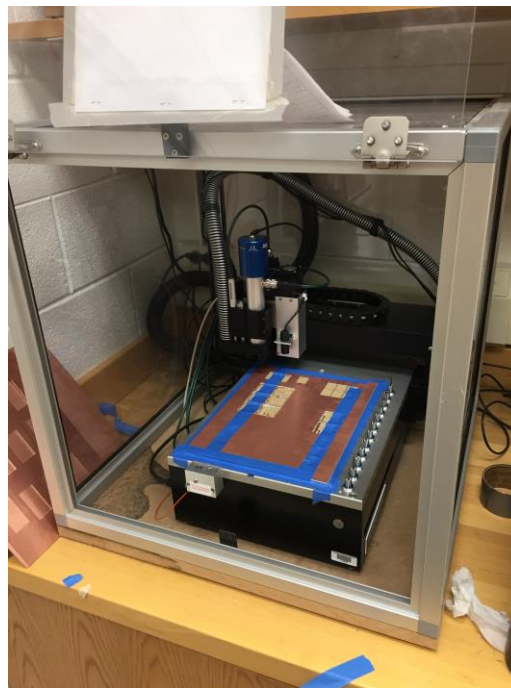
Fig. 2.4 Milling machine for printed circuits board (PCB) circuit fabrication.
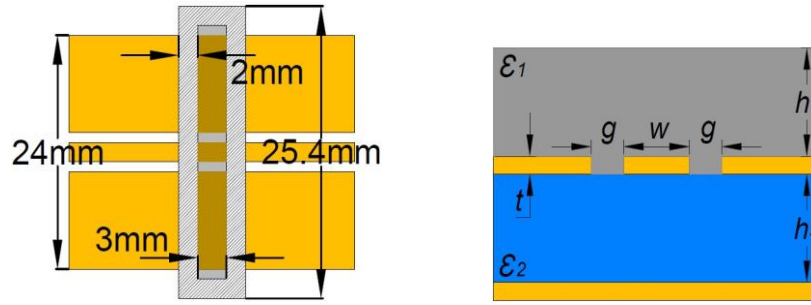
Fig. 2.5 Dimensions of top view and cross section of the sensing zone, where w=2 mm, g=1 mm, t=17 μm, h_1=2.625 mm, h_2=0.787 mm, ε_1: MUT permittivity, ε_2: 2.33.

The sensitivity of the sensor at a given frequency f_0 is characterized by Q_{eff} or equivalently $|S_{21}|_{min}$ if the insertion loss of the circuit components in Fig. 2.3 is negligible. The value of $|S_{21}|_{min}$ is determined by the level of electrical balance between the two branches when REF solutions, which do not have to be identical, are included in the MUT and REF wells. The level of balance, i.e., the sensitivity $|S_{21}|_{min}$, and the operating frequency f_0 can be tuned by the attenuators and phase shifters. The introduction of MUT or change of MUT properties will cause $|S_{21}|_{min}$ and f_0 shifts, which are the sensing indicators that can be further processed to obtain MUT properties. Fig. 2.6 shows the measured $|S_{21}|_{min}$ when DI water is used as REF solutions in both wells. It shows that the RF sensor has high sensitivities over the measured frequency range. Lossy water does not significantly decrease sensor sensitivity due to its relatively small volume. This observation is further verified by doubling the PDMS well length in MUT branch. Nevertheless, the amount of water used in the tests is large in the context of μ-TAS due to large GCPW dimensions. Considering the scalability of GCPW sizes, the achieved $|S_{21}|_{min}$ also indicates high sensitivities when measuring small-volume samples with nanometer

GCPWs. Hence, the sensor sensitivities compare favorably against current RF sensors, such as the planar ones in [2.16]-[2.17]. Furthermore, the lowest $|S_{21}|_{min}$ at ~10.06 GHz yields a Q_{eff} of ~3.8×10^6, which is much higher than the un-loaded Q of dielectric resonators [2.18]. This Q_{eff} is also comparable with that of the optical dielectric resonators, which have been developed for single molecule and single nano-particle measurements [2.19]. Fig. 2.6 also shows different $|S_{21}|_{min}$ values at different frequencies. The differences are mainly caused by the manual tuning operations of the attenuators and phase shifters. With better tuning components and better control, it is expected that $|S_{21}|_{min}$ uniformity will be significantly improved across the operating frequency ranges.
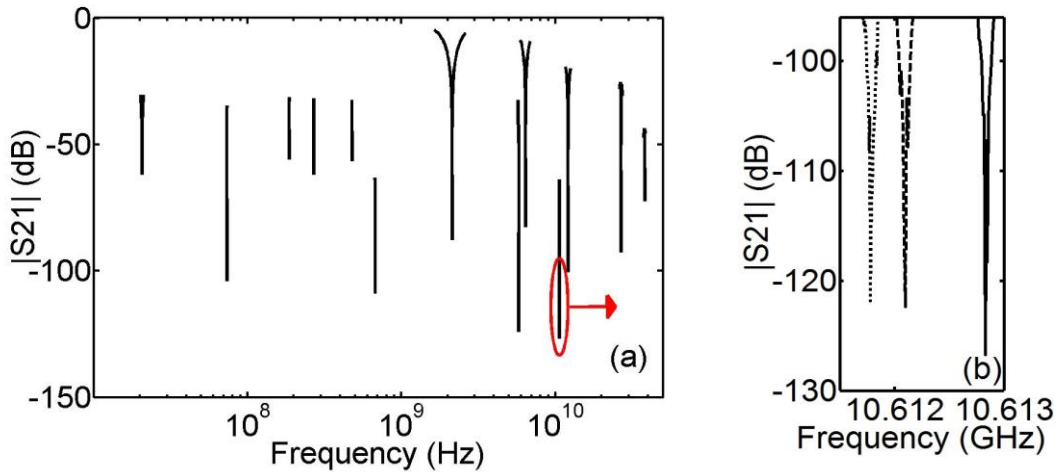
Fig. 2.6 (a) Measured $|S_{21}|$ from ~20.5 MHz to ~38 GHz. (b) Zoom in view at one frequency point.

It should be pointed out that $|S_{21}|_{min}$ values and their corresponding frequencies, f_0, fluctuate and drift with time when the RF sensor is tuned for high sensitivity operations,

as shown in Fig. 2.6 zoom-in. As a result, the high sensitivity tuning in Fig. 2.6 is only

obtained for time duration of about 1~2 minutes. The technique that automatically tunes

the sensitivity of the RF interferometer can improve this issue, presented in Chapter IV.

To demonstrate the operation of the presented interferometer, 0.01 mole fraction

2-proponal/methanol-water solutions are measured. It is placed in the PDMS well in Fig.

2.5. A plastic cylindrical tube is used to hold DI water as REF on the second and identical

CPW. The use of a plastic tube is to illustrate the flexibility of the sensor. The

measurement is focused on frequency band *II*, from ~1 GHz to ~12 GHz, where we have

better tuning components as well as discrete standards for vector network analyzer (VNA)

calibration.

First, use DI water in MUT well to adjust the RF sensor at each f_0 to obtain a

$|S_{21}|_{min}$ of ~-60 dB to ~-70 dB. Then, the water is replaced by methanol-water solution,

which is replaced by the 2-propanol-water solution subsequently. Lastly, 2-propanol-

water mixture is measured. The obtained results are shown in Fig. 2.7.
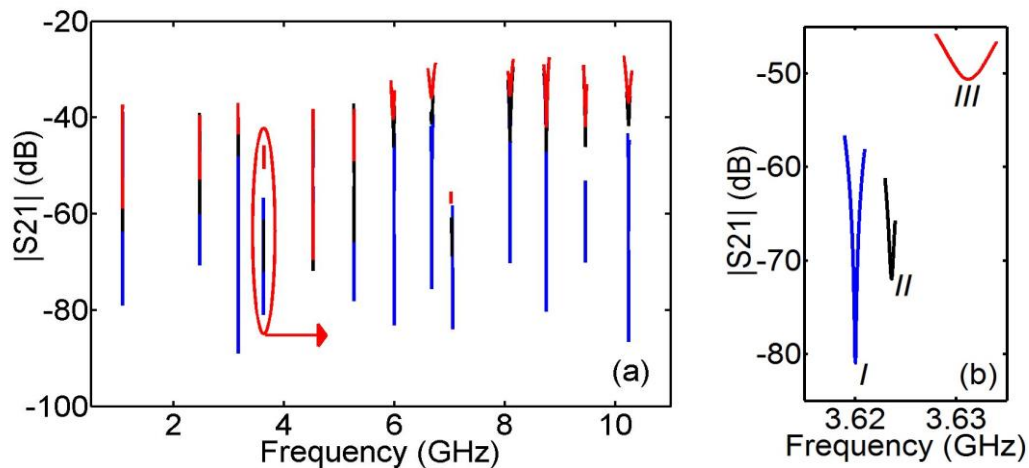
Fig. 2.7 (a) The measured S_{21} magnitude from ~1 GHz to ~10 GHz for water-water, methanol-water and 2-proponal-water solutions. (b) Zoom in view at one frequency point, where *I*: DI water, *II*: methanol-water, *III*: 2-propanol-water.

2.2 Quantitative Analysis of the Interferometer

The introducing of multiple solutions can calibrate the interferometer system for the extraction of the complex permittivity of MUT solution. The reason is that the manually tunable components in Fig. 2.3 do not provide accurate readings. As a result, their exact phase and attenuation values are unknown. These values are also different at different frequency f_0. In order to address this issue, it is assumed that the permittivities of two of three solutions, i.e., DI water, and 2-propanol-/methanol-water mixtures (at 0.01 mole fraction) are known, e.g., the data in [2.2] and [2.6]. Then the third can be solved using the following equations:

$$\frac{S_{21(m)} - S_{21(w)}}{S_{21(p)} - S_{21(w)}} = \frac{\exp(-\gamma_m l_{MUT}) - \exp(-\gamma_w l_{MUT})}{\exp(-\gamma_p l_{MUT}) - \exp(-\gamma_w l_{MUT})} \qquad (2.4)$$

where it is assumed that DI water and methanol-water have known permittivities, and 2-propanol-water is the MUT. Subscript *m* is for methanol-water solution, *p* is for 2-propanol-water solution, *w* is for water-water measurement, and l_{MUT} is for the length of the PDMS well in Fig. 2.5. The parameters $\gamma_{m,p,w}$ are the corresponding propagation constants. Once $\gamma_p = \alpha_p + j\beta_p$ is obtained, the real and imaginary permittivity components of 2-propanol-water solution, $\varepsilon_p = \varepsilon_p' - j\varepsilon_p''$, can be obtained through the following equations for a GCPW.

$$\alpha_p = \pi a_1 \varepsilon_1^{''} / (\lambda_0 \sqrt{(a_0 - a_1 + a_1 \varepsilon_1^{'} + a_2 \varepsilon_2^{'})(a_0 + a_2)}) \qquad (2.5)$$

$$\beta_p = 2\pi f \sqrt{\varepsilon_0 \mu_0} \sqrt{(a_0 - a_1 + a_1 \varepsilon_1^{'} + a_2 \varepsilon_2^{'}) / (a_0 + a_2)} \qquad (2.6)$$

where parameters $a_i=2\varepsilon_0 K(k_i)/K(k_i')$, $i=0$, 2, $a_1=2\varepsilon_0 K(k_i')/K(k_i)$, $K(k)$ is the complete

elliptic integrals of the first kind with modulus k, as shown below, and $k'=(1-k^2)^{0.5}$.

$$k_0 = w / (w + 2g) \qquad (2.7)$$

$$k_1 = \sinh(\pi w / 4h_1) / \sinh(\pi(w + 2g) / 4h_1) \qquad (2.8)$$

$$k_2 = \tanh(\pi w / 4h_2) / \tanh(\pi(w + 2g) / 4h_2) \qquad (2.9)$$

where the geometrical parameters are defined in Fig. 2.5.

The above analysis ignored the effects of mismatches between MUT/REF section

and their adjacent 50 Ω sections. For S_{11}, the reflection is partly absorbed by the power

dividers. For S_{21}, mismatch effects are included in its accurate expression [2.20]

$$S_{21(branch)} = \frac{2ZZ_0}{2ZZ_0 \cosh(\gamma l) + (Z^2 + Z_0^2) \sinh(\gamma l)} \qquad (2.10)$$

where Z is the characteristic impedance of the Reference/MUT section. A constant ratio

$S_{21(branch)}/\exp(-\gamma l)$ of for calibration solutions and MUT indicates that reflection can be

ignored. For calibration liquids and MUT with close permittivity values in this work, e.g.,

DI water, methanol-water and 2-propanol-water both with 0.005 and 0.01 mole fractions,

respectively, the ratio at 6 GHz is (1.56~1.58)∠(-0.04~-0.03), which can be considered to

be a constant. Consequently, the calibration process and the use of the simplified S_{21} in eq.

(2.4) can be used for simplified extraction of extract MUT permittivity. However, for

large permittivity differences, better matched REF/MUT lines should be considered or eq. (2.10) should be used. As a result, data processing is a lot more involved.

2.3 Fabrication of the PDMS Well

Dow Corning's 184 Sylgard Elastomer [2.21] with two separate bottles of liquid base and curing agent are used to synthesize PDMS well. First, prepare two clean glass or plastic dishes, and place mold for the well on one dish. Then, mix base and curing agent together using a weight ratio of 10:1 and stir them for about 15 minutes until they are mixed sufficiently (a lot of bubbles appear). Next, pour the mixture onto the mold on another dish, place the dish into the vacuum oven, and vacuum it until all bubbles disappear. Finally, make the oven keep $60^{o}C$ for 1 hour, then it is ready to use after peeled off from the mold [2.22].

In spite of a lot of advantages of PDMS material, e.g. rapid prototyping, and sealing, transparency for observation, chemical inertness [2.23], which facilitates it be widely used in all sorts of microfluidic devices, PDMS is not a universal material and not suitable for all MUTs. If an inappropriate sample is held in PDMS channel, it would cause measurement uncertainty and even incorrect result. Three main aspects need to be carefully considered, i.e., the solubility of a solvent in PDMS since this solubility influences the swelling of the PDMS, the solubility of solutes in PDMS (or more properly, the partition of solute between a solution and PDMS) since loss of solute from the solvent is a concern; the dissolution of PDMS oligomers in solvent since these oligomers (present as contaminants in cross-linked PDMS) are potential contaminants in PDMS.

Swelling changes the cross sectional area of PDMS well and the rate and profile

of flow in PDMS channel therefore. Also, changes in channel dimensions due to swelling

can affect integration of the channel attaching with other components, such as substrate.

Table 2.1 [2.23] summarizes the swelling of the PDMS in different solvents, where S is

the swelling ratio that was measured experimentally. We can see that there is almost no

swelling for some solvents, e.g., water, glycerol, and nitromethane, but some solvents can

cause significant swelling, e.g., diisopropylamine, triethylamine, and pentane, which

cannot be held directly by a PDMS-based structure.

TABLE 2.1
SOLUBILITY PARAMETERS AND SWELLING RATIOS
OF VARIOUS SOLVENTS USED IN ORGANIC SYNTHESIS [2.23]

Solvent	δ^a	S^b
water	23.4	1.00
glycerol	21.1	1.00
nitromethane	12.6	1.00
diisopropylamine	7.3	2.13
triethylamine	7.5	1.58
pentane	7.1	1.44

$^a\delta$ in units of $\mathrm{cal}^{1/2}\ \mathrm{cm}^{-3/2}$. ^bS denotes the swelling ratio that was measured experimentally; $S=D/D_0$, where D is the length of PDMS in the solvent and D_0 is the length of the dry PDMS.

Table 2.2 [2.23] shows partitioning of solutes between a solvent and PDMS,

where the Flory-Huggins interaction parameter χ is used to evaluate partitioning.

$$\chi = \frac{V_1}{RT}(\delta_{solvent} - \delta_{PDMS})^2 \qquad (2.11)$$

where V_1 is the molar volume of solvent, R is the real gas constant, and T is the

Temperature. When χ is close to zero, the maximum mixing or interaction between

PDMS and solvent exists. Taking rhodamine for example, when dissolved in water,

propylene carbonate, and nitromethane, it has more significant partition ratios than dissolved in ethanol. If one would like to detect rhodamine, ethanol should be a better solvent choice than other three.

TABLE 2.2
PARTITIONING OF ORGANIC COMPOUNDS
IN SOLVENT/PDMS MIXTURES [2.23]

Compound	Partition ratios ($A_{solvent}/(A_{solvent}+A_{PDMS})$)		
	water	nitromethane	ethanol
Rhodamine	0.4 ±0.1	0.83 ±0.08	0.97 ±0.03
Fluorescein	1.00 ±0.04	a	b
Dansyl chloride	a	1.00 ±0.01	b

[a]Compoud did not dissolve in solvent. [b]Fluorescence of compound was quenched in the solvent/PDMS mixture.
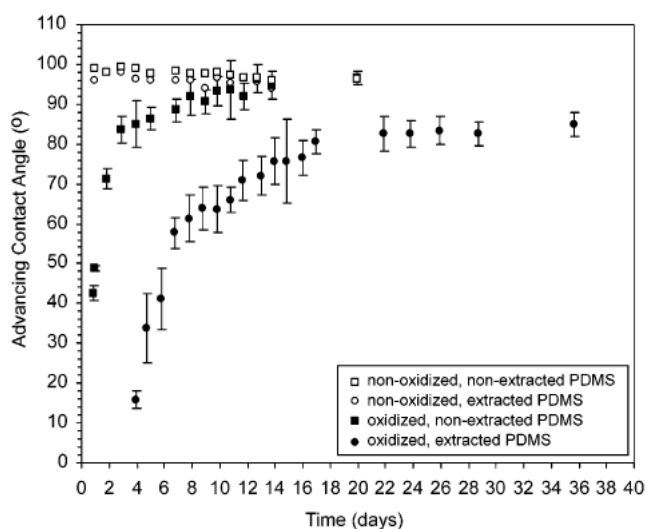
Fig. 2.8 Contact angle versus time for □non-oxidized, non-extracted PDMS; ○non-oxidized, extracted PDMS; ■oxidized, non-extracted PDMS; ●oxidized, extracted PDMS [2.23].

Removal of PDMS oligomers (un-cross-linked hydrophobic groups) from solvent can be achieved using the O_2 plasma treatment for a hydrophilic surface. The detailed steps of plasma treatment will be introduced in Section 3.4. Some organic solvents, e.g., diisopropylamine, are also reported to be effective for decreasing the rate of regeneration of the hydrophobic surface by extracting un-cross-linked oligomers. Figure 2.8 [2.23] is the relationship between contact angle (for measuring hydrophilicity/hydrophobicity) and time, indicating that the use of O_2 plasma treatment and diisopropylamine can create a long-term hydrophilic PDMS surface.

References

[2.1] Geophysics for Practicing Geoscientists. [Online]. Available: http://gpg.geosci.xyz/content/physical_properties/physical_properties_dielectric_permittivity.html

[2.2] T. Sato, A. Chiba, and R. Nozaki, "Hydrophobic hydration and molecular association in methanol-water mixtures studied by microwave dielectric analysis," *J. Chem. Phys.*, vol. 112, no. 6, pp. 2924-2932, Feb. 2000.

[2.3] N. Agmon, "Tetrahedral Displacement: The Molecular Mechanism behind the Debye Relaxation in Water," *J. Phys. Chem.*, vol. 100, no.3, pp. 1072-1080, Jan. 1996.

[2.4] T. Sato, A. Chiba, and R. Nozaki, "Composition-dependent dynamical structures of 1-propanol–water mixtures determined by dynamical dielectric properties," *J. Chem. Phys.*, vol. 113, no. 21, pp. 9748-9758, Dec. 2000.

[2.5] T. Sato and R. Buchner, "Dielectric relaxation spectroscopy of 2-propanol–water mixtures," *J. Chem. Phys.*, vol. 118, no. 10, pp. 4606-4613, Mar. 2003.

[2.6] T. Sato and R. Buchner, "The cooperative dynamics of the H-bond system in 2-propanol/water mixtures: steric hindrance effects of nonpolar head group," *J. Chem. Phys.*, vol. 119, no. 20, pp. 10789-10800, Nov. 2003.

[2.7] T. Sato and R. Buchner, "Dielectric relaxation processes in ethanol/water mixtures," *J. Phys. Chem. A*, vol. 108, no. 23, pp. 5007-5015, May 2004.

[2.8] R. Hölzel, "Dielectric and dielectrophoretic properties of DNA," *IET Nanobiotechnol.*, vol. 3, no. 2, pp. 28-45, Jun. 2009.

[2.9] S. Tomić, S. Dolanski Babić, T. Vuletić, S. Krča, D. Ivanković, L. Griparić, and R. Podgornik, "Dielectric relaxation of DNA aqueous solutions," *Phys. Rev. E*, vol. 75, no. 2, pp. 021905, Feb. 2007.

[2.10] T. H. Basey-Fisher, S. M. Hanham, H. Andresen, S. A. Maier, M. M. Stevens, N. M. Alford, and N. Klein, "Microwave Debye relaxation analysis of dissolved proteins: Towards free-solution biosensing," *Appl. Phys. Lett.*, vol. 99, no. 23, pp. 233703, Dec. 2011.

[2.11] K. Fuchs and U. Kaatze, "Molecular dynamics of carbohydrate aqueous solutions. Dielectric relaxation as a function of glucose and fructose concentration," *J. Phys. Chem. B*, vol. 105, no. 10, pp. 2036-2042, Feb. 2001.

[2.12] C. Song and P. Wang, "A radio frequency device for measurement of minute dielectric property changes in microfluidic channels," *Appl. Phys. Lett.*, vol. 94, no. 2, pp. 023901, Jan. 2009.

[2.13] Y. Yang, H. Zhang, J. Zhu, G. Wang, T. R. Tzeng, X. Xuan, K. Huang, and P. Wang, "Distinguishing the viability of a single yeast cell with an ultra-sensitive radio frequency sensor," *Lab Chip*, vol. 10, no. 5, pp. 553-555, Jan. 2010.

[2.14] J. Wessel, K. Schmalz, G. Gastrock, B. P. Cahill, and C. Meliani, "Contactless investigations of yeast cell cultivation in the 7 GHz and 240 GHz ranges," *J. Phys.: Conf. Ser.*, vol. 434, conf. 1, pp. 012033, 2013.

[2.15] A. Kozhevnikov, "Wideband radio-frequency device for measurements of dielectric properties of small volumes of liquids," *Meas. Sci. Technol.*, vol. 21, no. 4, pp. 043001, Mar. 2010.

[2.16] T. Chretiennot, D. Dubuc, and K. Grenier, "A microwave and microfluidic planar resonator for efficient and accurate complex permittivity characterization of aqueous solutions," *IEEE Trans. Microw. Theory Techn.*, vol. 61, no. 2, pp. 972-978, Feb. 2013.

[2.17] F. Costa, C. Amabile, A. Monorchio, and E. Prati, "Waveguide dielectric permittivity measurement technique based on resonant FSS filters," *IEEE Microw. Wireless Compon. Lett.*, vol. 21, no. 5, pp. 273-275, May 2011.

[2.18] Y. M. Poplavko, Y. V. Prokopenko, V. I. Molchanov, and A. Dogan, "Frequency-tunable microwave dielectric resonator," *IEEE Trans. Microw. Theory Techn.*, vol. 49, no. 6, pp. 1020-1026, Jun. 2001.

[2.19] X. Liu, L. P. B. Katehi, W. J. Chappell, and D. Peroulis, "High-Q tunable microwave cavity resonators and filters using SOI-based RF MEMS tuners," *J. Microelectromech. Syst.*, vol. 19, no. 4, pp. 774-784, Aug. 2010.

[2.20] K. C. Gupta, R. Grag, and R. Chada, *Computer Aided Design of Microwave Circuits*. Dedham, MA, USA: Artech House, 1981, pp. 25-43.

[2.21] SYLGARD® 184 SILICONE ELASTOMER KIT, http://www.dowcorning.com/applications/search/products/Details.aspx?prod=01064291

[2.22] J. C. McDonald, D. C. Duffy, J. R. Anderson, D. T. Chiu, H. Wu, O. J. A. Schueller, and G. M. Whitesides, "Fabrication of microfluidic systems in poly(dimethylsiloxane)," *Electrophoresis*, vol. 21, no. 1, pp. 21-27, Jan. 2000.

[2.23] J. N. Lee, C. Park, G. M. Whitesides, "Solvent compatibility of poly (dimethylsiloxane)-based microfluidic devices," *Anal. Chem.*, vol. 75, no. 23, pp. 6544-6554, Dec. 2003.

CHAPTER THREE

DETECTION AND ANALYSIS OF AQUEOUS SOLUTIONS

USING COPLANAR WAVEDUIDE SENSING STRUCTURES

3.1 Mathematical Models of the Sensing Structures

A GCPW component is used as the sensing structure in Fig. 2.2, which is also

replaced by a regular CPW (without backed conductor) or microstrip line (ML). Fig. 3.1

shows the top and cross-section views of CPW-based MUT transmission line (TL)

section together with a microfluidic channel. The capacitance of a uniform CPW with the

cross section in Fig. 3.1 can be written as the superposition of four partial capacitances

[3.1]:

$$C_{tot} = C_0 + C_1 + C_2 + C_3 \qquad (3.1)$$

The configurations for the calculation of these partial capacitances are similar to

those in [3.1]. The expressions of $C_0 \sim C_3$ are [3.1]:

$$C_0 = 4\varepsilon_0 \frac{K(k_0')}{K(k_0)} = 2a_0 \qquad (3.2)$$

$$C_1 = 2\varepsilon_0(\varepsilon_1' - \varepsilon_3') \frac{K(k_1')}{K(k_1)} = a_1(\varepsilon_1' - \varepsilon_3') \qquad (3.3)$$

$$C_2 = 2\varepsilon_0(\varepsilon_2' - 1) \frac{K(k_2')}{K(k_2)} = a_2(\varepsilon_2' - 1) \qquad (3.4)$$

$$C_3 = 2\varepsilon_0(\varepsilon_3' - 1) \frac{K(k_3')}{K(k_3)} = a_3(\varepsilon_3' - 1) \qquad (3.5)$$

where $a_i = 2\varepsilon_0 K(k_i')/K(k_i)$ ($i=0, 1, 2, 3$), $k' = (1-k^2)^{0.5}$, $K(k)$ is the complete elliptic integrals

of the first kind with modulus $k_0 = w/(w+2g)$, $k_i(i=1, 2, 3)$, and

$$k_i = \frac{\sinh\left(\dfrac{\pi w}{4h_i}\right)}{\sinh\left(\dfrac{\pi(w+2g)}{4h_i}\right)} \qquad (3.6)$$

The effective permittivity of the CPW is

$$\varepsilon_{eff} = \varepsilon_{r,eff} - j\varepsilon_{i,eff} \qquad (3.7)$$

where the real and imaginary components of the permittivity are [3.2]

$$\varepsilon_{r,eff} = \frac{C_{tot}}{C_0} = q_0 + q_1\varepsilon_1' + q_2\varepsilon_2' + q_3\varepsilon_3' \qquad (3.8)$$

$$\varepsilon_{i,eff} = q_1\varepsilon_1'' + q_2\varepsilon_2'' + q_3\varepsilon_3'' \qquad (3.9)$$

where filling factors $q_0=(2a_0-a_2-a_3)/(2a_0)$, $q_1=a_1/(2a_0)$, $q_2=a_2/(2a_0)$, $q_3=(a_3-a_1)/(2a_0)$.

(a)   (b)
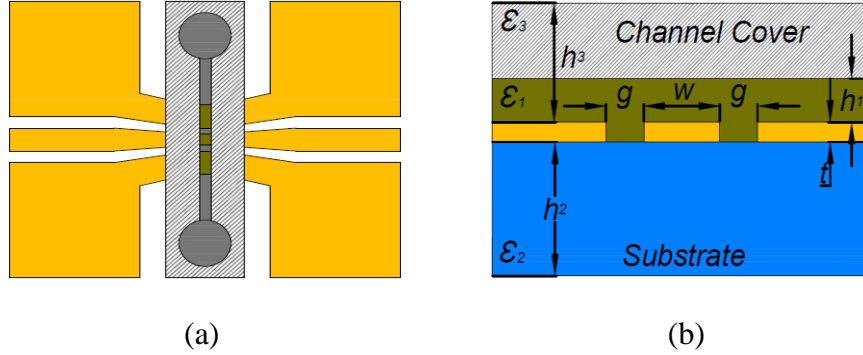
Fig. 3.1 (a) Top view and (b) cross section of a CPW MUT section.

The dielectric loss α_d is determined by the substrate, MUT liquids and the channel cover material,

$$\alpha_d = \frac{\omega}{2c\sqrt{\varepsilon_{r,eff}}}(q_1\varepsilon_1'' + q_2\varepsilon_2'' + q_3\varepsilon_3'') \qquad (3.10)$$

The conductor loss α_c of the center signal line and the ground planes can also be calculated. But its effects will be cancelled out in eq. (2.1).

For phase constant β, it depends on the relative effective dielectric constant $\varepsilon_{r,eff}$,

$$\beta = \frac{\omega}{v_{ph}} = 2\pi f \sqrt{\varepsilon_0 \varepsilon_{r,eff} \mu_0} \tag{3.11}$$

Thus, MUT permittivity $\varepsilon = \varepsilon' - j\varepsilon''$ can be obtained from $\gamma_{MUT} = (\alpha_c + \alpha_d) + j\beta$ with eq. (3.10) and (3.11). The algorithm for extracting material property $\varepsilon = \varepsilon' - j\varepsilon'' = \varepsilon'(1 - \tan\delta)$ from scattering parameters is also summarized in Fig. 3.2, where the subscript $cal1$ and $cal2$ represent two different calibration liquids with known dielectric constants. As mentioned in the end of Chapter II, the purpose of two different calibration liquids is to increase the number of independent measurements to remove the unknown effects brought by the cables, manual attenuators and phase shifters in Fig. 2.3.
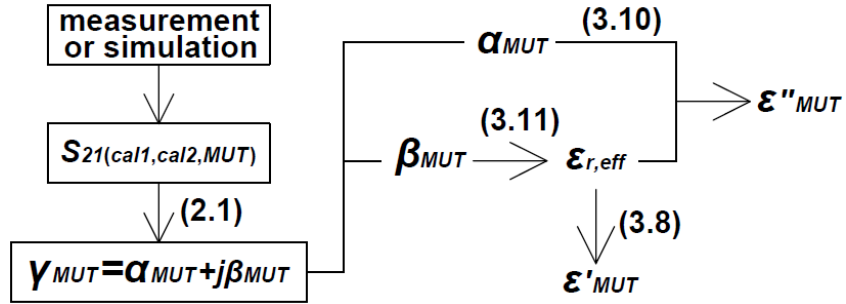
Fig. 3.2 Algorithm to obtain MUT permittivity values from S-parameters.

For GCPW-/ML-based MUT TL section, shown in Fig. 3.3 and 3.4 respectively, the similar mathematical models can be also presented to quantify material properties from scattering parameters.
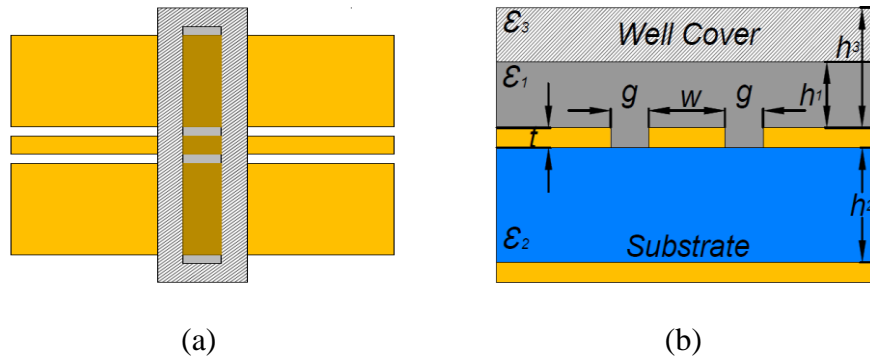
Fig. 3.3 (a) Top view and (b) cross section view of the GCPW MUT section.
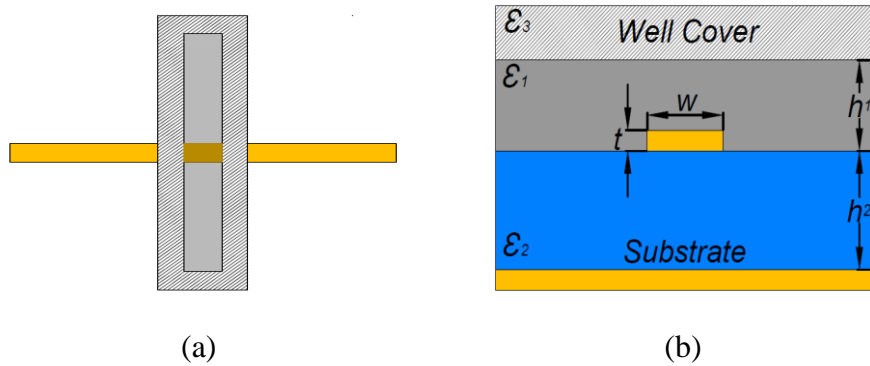
Fig. 3.4 (a) Top view and (b) cross section of the ML MUT section.

3.2 Quadrature Hybrid Based RF Interferometers

Power dividers in Fig. 2.3 can be replaced with broadband quadrature hybrids, as shown in Fig. 3.5. Compared with power divider implementation, the quadrature hybrid implementation enables the use of reflected RF probing signals, e.g., S_{11} in Fig. 3.6, in addition to transmission signal S_{21}. The use of S_{11} also helps to address the uncertainties that appear in obtaining phase constant β_{MUT} from propagation constant. The use of S_{21} will not be repeated below.
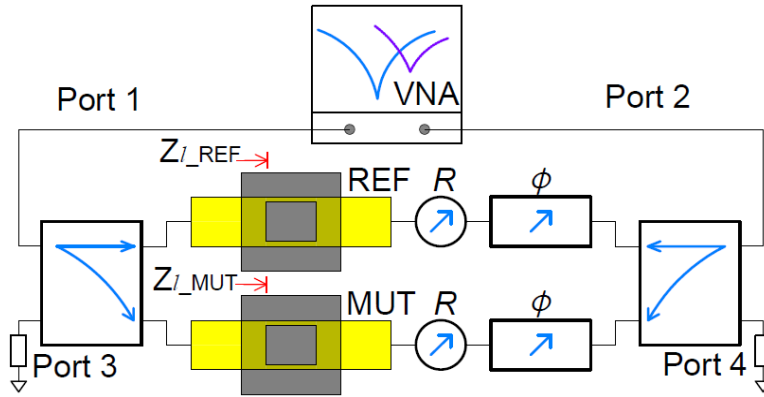
Fig. 3.5 The schematic of an interferometer that is based on quadrature hybrids.

To use S_{11} to obtain MUT properties, it is easy to show

$$\frac{S_{11(MUT)} - S_{11(cal1)}}{S_{11(cal2)} - S_{11(cal1)}} = \frac{\dfrac{Z_{L(MUT)} - Z_0}{Z_{L(MUT)} + Z_0} - \dfrac{Z_{L(cal1)} - Z_0}{Z_{L(cal1)} + Z_0}}{\dfrac{Z_{L(cal2)} - Z_0}{Z_{L(cal2)} + Z_0} - \dfrac{Z_{L(cal1)} - Z_0}{Z_{L(cal1)} + Z_0}} \qquad (3.12)$$

where $Z_{L(MUT)}$ is the impedance looking towards attenuators and phase shifters at the MUT branch. Matching consideration is assumed between adjacent circuit components except the MUT TL section, which has a characteristic impedance of Z_{MUT}. For CPW and GCPW, it can be written as [3.1]

$$Z_{MUT} = 1/(C_{tot} v_{ph}) = \sqrt{\varepsilon_{r,eff}} / (C_{tot} c) \qquad (3.13)$$

For ML, the following expression can be used [3.3]

$$Z_{MUT} = \frac{60}{\sqrt{\varepsilon_{r,eff}}} \ln \frac{8h_2}{w} \qquad (3.14)$$

which is valid for $w/h_2 \geq 1$, and the expression for $w/h_2 \leq 1$ is also given in [3.3].
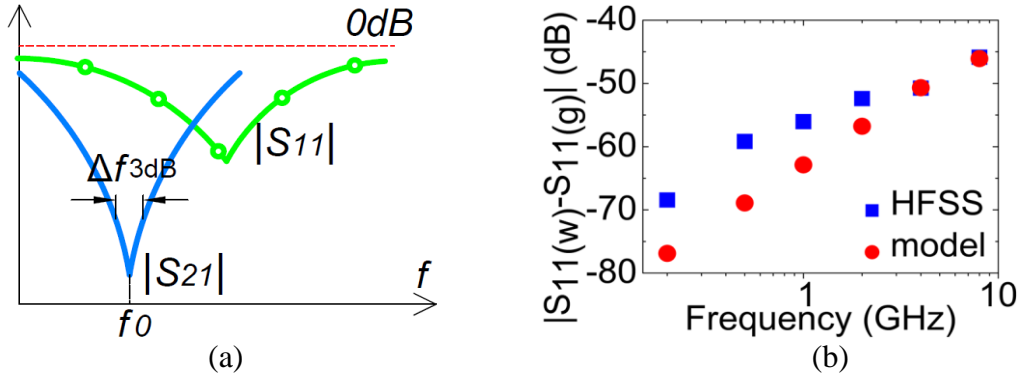
Fig. 3.6 (a) Illustrations of $|S_{21}|$ and $|S_{11}|$. (b) $|S_{11}|$ differences of a CPW based MUT TL.

The obtained scattering parameters S_{11} and S_{21} can be combined to obtain MUT permittivity. The use of S_{11} for MUT detection is also highly sensitive even though the measured S_{11} does not yield an effective Q that is nearly as high as that from $|S_{21}|_{min}$. The high-sensitivity is enabled by the differential nature of the reflections from MUT and REF branch in Fig. 3.5. The differential operation of S_{11} in eq. (3.12) also removes reflections from mismatches occurred mainly at quadrature-hybrid connections. These reflections are part of the measured S_{11} data for each individual measurement and cause much higher $|S_{11}|$ values (e.g., -20 dB) than $|S_{21}|_{min}$ values (e.g., -100 dB). Thus, the smallest $|S_{11}|$ change measured by VNA determines S_{11}-related sensitivity. Typical long-term measurement uncertainty of $|S_{11}|$ is better than 0.005 for commercial VNAs. For the measurements at each frequency point, it is observed that S_{11} is stable at the 5th digit, which corresponds to a level of ~-100 dB. It implies that the proposed differential S_{11} measurement has the potential to achieve a sensitivity that is comparable to that of $|S_{21}|_{min}$.

3.3 High Sensitivity Measurements

The operating principles of the two types of interferometers in Figs. 2.3 and 3.5 have been demonstrated in the above section. In this chapter, the quadrature-hybrid-based interferometer is further improved for stable operations at much higher sensitivity levels than those in Fig. 2.7. The improved performance is demonstrated by measuring glucose solutions at a concentration level 10-times lower than that in [3.4] and pET21a (pE) DNA solution at 10 ng/mL, which is close to the lowest detectable concentration level [3.5]. At the same time, the effective MUT volume is only ~1 nL. The analysis of molecular compositions of ternary solutions with a power-divider based interferometer is further demonstrated. Such capabilities may lead to some interesting applications, including non-invasive, label-free detection and identification of molecules [3.6].

The CPW TL MUT section is fabricated with standard microfabrication techniques on 1 mm thick fused silica substrate. The detailed process will be introduced in Section 3.5. A 500 nm thick gold film on top of a 10 nm thick Ti adhesion layer is deposited as CPW sensing electrode. Microfluidic channels, 500 μm wide and 50 μm high, are incorporated with the CPW for MUT handling. High Frequency Structure Simulator (HFSS) [3.7] simulation indicates that the channel has an insertion loss of 0.54 dB at 6 GHz with water as MUT. The small loss does affect measurement sensitivity, but negligible in the proposed measurements. Fig. 3.7 shows the measurement setup, where VNA, phase shifters and attenuators are marked, for glucose-/DNA-water solution measurements. The CPW lines for MUT and REF are covered with thick PDMS slabs to eliminate deposition of micro-particles from the measurement environment onto CPW

surfaces. The post-processing of the PDMS channel for good adhesion and hydrophilicity will be introduced in Section 3.4. These particles and the mechanical stability of the cables and connections in Fig. 3.7 affect achievable $|S_{21}|_{min}$, which is improved by about 15~20 dB in this Chapter when compared with that in Fig. 2.7. The Q_{eff} magnitude is improved from ~10^4 to ~10^5. The micro-particles are mainly from air in the measuring environment. Figure 3.8 shows measured S_{21} and S_{11} of glucose-water solution at 5 mg/dL (~0.0002 mol/L) from ~2 GHz to ~10 GHz. The concentration level is 10 times lower than that in [3.4], which aims at non-invasive measurements of glucose in blood vessels. DI water and methanol-water solution (at 0.005 mole fraction) are used as calibration liquids for this measurement.
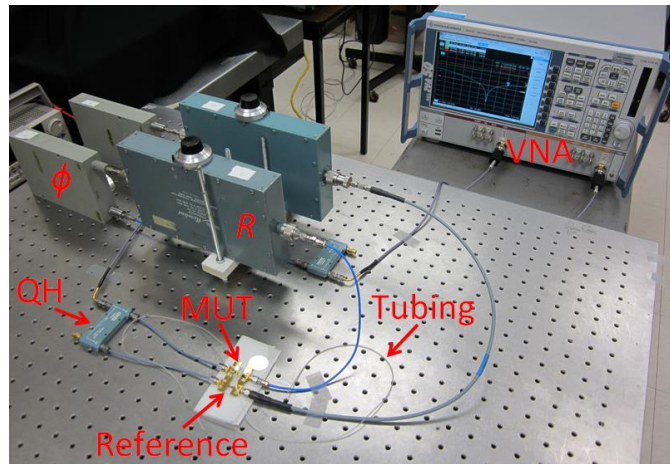
Fig. 3.7 A high sensitivity interferometer measurement setup.
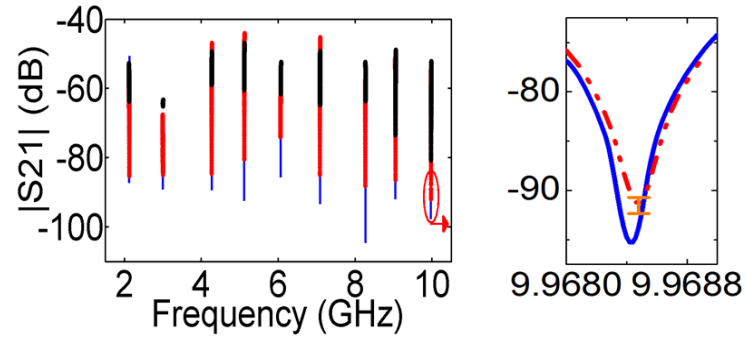
(a)
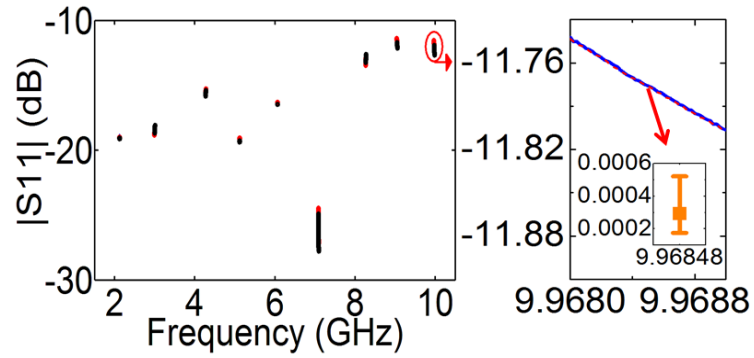
(b)

Fig. 3.8 Measured (a) S_{21} and (b) S_{11} from ~2 to ~10 GHz and a zoom-in view at ~10 GHz (blue solid line, *I*: DI water; red dashed line, *II*: glucose-water; black circles: methanol-water). The error bar in (b) shows the range of $|S_{11}|$ difference for water (*w*) and glucose-water (*g*) at the frequency f_0, i.e., $|S_{11}|_w$-$|S_{11}|_g$ (dB).

Figure 3.9 shows the calculated permittivity of glucose-water solution by following the algorithm in Fig. 3.2. Based on the calculated results, the Cole-Cole (CC) equation in [3.8] can be fitted through a least-square fitting approach, also drawn in the same figure. Table 3.1 lists all fitting parameters in the CC equation. The uncertainty of the REF material property also propagates to the extracted MUT properties. For instance,

the calculated 5 mg/dL glucose-water permittivity value is 77.57-j7.96 at ~2 GHz if the permittivity of the calibration liquid methanol-water (at 0.005 mole fraction) is 77.02-j8.10 [3.9]. A +1% uncertainty, i.e., a deviation of 0.77-j0.08 of methanol-water permittivity, induces a +1% shift of glucose-water solution permittivity to 78.30-j8.04. If the same process is repeated again at ~10 GHz, the permittivity changes from 63.10-j29.66 to 63.18-j29.75, which is smaller than 1% shift. The larger uncertainty at relatively lower frequency point is caused by closer permittivity values among calibration liquids 1&2 and MUT.
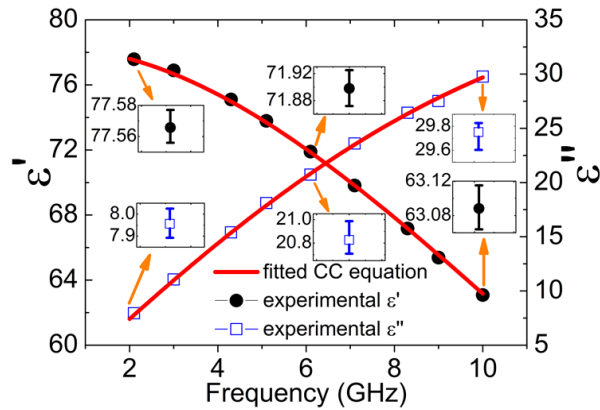
Fig. 3.9 The permittivity, $\varepsilon=\varepsilon'-j\varepsilon''$, of glucose-water solution at 5 mg/dL.

TABLE 3.1
FITTING PARAMETERS FOR GLUCOSE-WATER SOLUTION
AT DIFFERENT CONCENTRATIONS

Parameter	Fitting values			
	0.0002 mol/L	0.001 mol/L	0.01 mol/L	0.1 mol/L
ε_0	78.36	78.52	77.9	77.6
τ_1	8.15 ps	8.21 ps	8.18 ps	7.57 ps
τ_2	8.17 ps	9.79 ps	9.50 ps	11.8 ps
a_1	72.1	71.7	70.4	64.5
a_2	1.1	2.02	2.6	10.1

Glucose-water solutions of different concentration levels are also measured with their permittivity values at each frequency point obtained. A part of the results are summarized in Table 3.1 with their fitting parameter values. It shows that the techniques can be applied to measure solutions with wide range concentration variations. The parameters also show that two types of Debye processes (high-frequency process: subscript 1; low frequency process: subscript 2) contribute to the dielectric spectrum of glucose-water solution [3.8]. With the concentration level increased, the fitting parameters a_1 and a_2 change in opposite directions, which suggest that the low frequency process is more significant. Parameters τ_1 and τ_2 also demonstrate such a trend. The change trend of ε_0 suggests that the static permittivity decreases with the increase of glucose molecules due to the glucose related low frequency processes. The non-monotonic variations of ε_0, τ_1 and τ_2 versus concentration level are probably due to measurement errors.

Fig. 3.10 shows the measured S_{21} magnitude for pET21a (pE) DNA at different concentration levels. Multiple measurements are conducted for each MUT sample. Corresponding $|S_{21}|_{min}$ points are also shown. It shows that the achievable sensitivity limit is below 10 ng/mL, i.e., 2.97×10^{-15} mol/mL, which is close to the highest sensitivity in [3.5]. In the measurements, however, the effective MUT volume is ~1 nL and DNA molecules are not pre-processed or concentrated. The distance between two adjacent DNA molecules in the solution is estimated to be ~8.2 μm. Such distance is much larger than the Debye length of pure DI water [3.10]. Therefore, the interactions among the

DNA molecules in the test solution are negligible. The demonstrated dielectric properties are a simple summation of the individual DNA molecules.
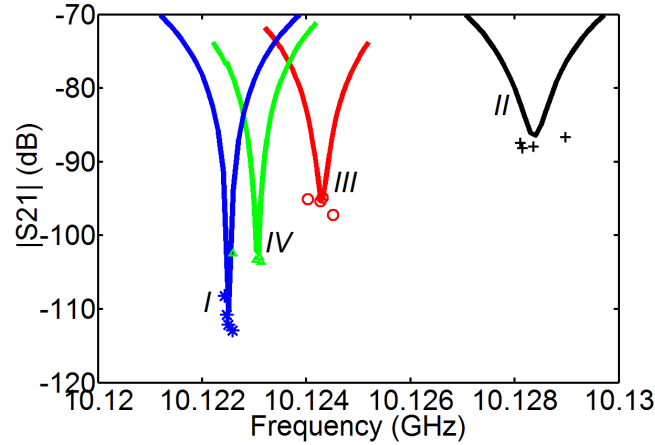
Fig. 3.10 $|S_{21}|$ measurement results for pE DNA aqueous solution with different concentration levels at ~10 GHz (blue line and snowflakes, *I*: DI water; black line and crosses, *II*: 1 μg/mL; red line and circles, *III*: 100 ng/mL; green line and triangles, *IV*: 10 ng/mL).

The GCPW TLs for Fig. 3.3 and the power divider-based measurement setup in Fig. 2.3 are used here to demonstrate the composition analysis of aqueous samples. PDMS wells with a 3 mm-long l_{MUT} are attached to the GCPWs to hold REF and MUT solutions, which has a volume of 200 μL. The HFSS simulation indicates that the GCPW section has an insertion loss of 1.75 dB at 6 GHz with water as MUT.

Three solution samples, methanol, 2-propanol, and water, are used for measurements. The mole fractions of the mixtures are listed in column 1 of Table 3.2.

Figure 3.11 shows measurement results for methanol-2-propanol-water solution (m: 0.01; p: 0.01) at ~1 GHz and ~8 GHz. DI water and 2-propanol-water mixture solution with a mole fraction of 0.01 are used as calibration liquids. The measurement setup is similar to that in Fig. 3.7.

The permittivity of the solutions can be obtained with the algorithm described in Fig. 3.2 and are shown in column 2 of Table 3.2.

One way to identify the concentration levels of the solution components is to exploit the relative dielectric constant expression [3.11], [3.12]

$$\varepsilon_{tot}' = (1 - x - y)\varepsilon_w' + x\varepsilon_m' + y\varepsilon_p' \qquad (3.15)$$

where ε_m' and ε_p' are relative dielectric constants of pure methanol and 2-propanol. Factors x and y are the mole fraction of methanol and 2-propanol, respectively. The excess function ε^E has been eliminated since the interactions between different molecules are expected to be weak under low mole fractions, as described in [3.11], [3.12].

TABLE 3.2
COMPOSITION ANALYSIS OF METHANOL-2-PROPANOL-WATER SOLUTIONS
WITH DIFFERENT MOLE FRACTIONS

Sample	Measurement result	
(*m* & *p*)	Permittivity (1 GHz & 8 GHz)	Mole fraction
0.01 & 0.01	76.71&66.02	0.0130 & 0.0130
0.005 & 0.01	77.17&66.31	0.0032 & 0.0139
0.01 & 0.005	77.07&65.93	0.0156 & 0.0069

Substituting these data and the corresponding permittivities of pure water, methanol and 2-propanol [3.8], [3.13] into (3.15), x and y can be found as 0.0130 and

0.0130, respectively. Table 3.2 also summaries the results for the other two samples. These results indicate that the obtained solution composition levels are reasonable even though further work is needed to improve the accuracies.

3.4 Surface Modifications of PDMS

The surface of the used PDMS channel required to be chemically modified using an O_2 plasma to be hydrophilic before it is attached onto a glass substrate for a good adhesion. Also, the hydrophilicity can facilitate the easiness of the solution flow.

First, the surface of PDMS and glass substrate needs to be well cleaned using isopropyl alcohol (IPA) and DI water. If there is diisopropylamine in lab, to rinse PDMS using it is recommended. Then, dry them using nitrogen if it is available in lab, otherwise, fiber-free paper is alternative. In this process and the followings, one should wear latex gloves to prevent possible contaminations.

Second, put the cleaned PDMS (face up) and glass substrate into the chamber of the plasma cleaner, and run it under the maximum RF power for 20 to 30 seconds.

Third, face down the PDMS and press it onto the glass under a microscope for good alignment. In this step, any air bubbles between the PDMS and the glass substrate should be removed.

Forth, place the glass with PDMS onto a hotplate for $85^{o}C$ and 30 minutes for annealing. Then it is ready to use. An excellent bonding means an irreversible process, i.e., once one tries to peel it off from the glass substrate, the PDMS structure will be destroyed permanently.

3.5 Microfarication Process

The metal layers of micro-machined sensing structures in this and next chapters are patterned by lift-off process in clean room. Compared to the wet-etching process, the micron-level CPW gap is closer to what is designed on the mask since no lateral etching occurs, which is positive to enhance the electric field in the gap and the sensitivity.

The main process and recipes are following:

(1) Cleaning Wafers

First, well clean 4-inch fused quartz wafers using 65°C Nanostrip or the mixture solvents of 96% H_2SO_4 and H_2O_2 (piranha solvent) at a volumetric percentage of 3:1 for removal of most organic matter and adding hydroxyl groups with highly hydrophilic. Then put them one by one into a Cl_2 plasma chamber for 3 minutes descuuming.

(2) Coating

Use a spinner and the following recipe in Table 3.3 to coat a ~500 nm thick photoresist LOR_3A layer [3.14] as the undercut layer in bi-layer to speed up the lift-off process. After that, place the wafer onto a hotplate at 150°C for 150 seconds for soft-baking. If there is no Cl_2 plasma in Step (1), the O_2 plasma can be alternative but higher temperature and longer time, e.g., 180°C and 5 minutes, are required for soft-baking, and an additional 200°C and 5 minutes dehydration process is highly recommended. Otherwise, there will be terrible mouse-bites after development, as shown in Fig. 3.11(a).

TABLE 3.3
SPINNING RECIPE FOR LOR_3A

Step #	RPM	RPM/s	Time (s)
1	500	500	10
2	1000	10000	45

<div align="center">(a)   (b)</div>
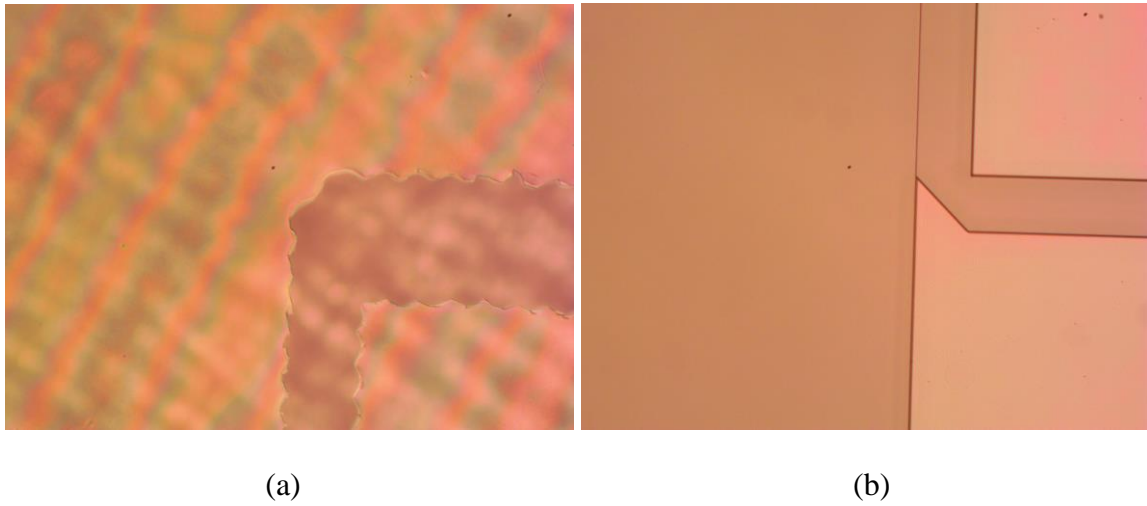
Fig. 3.11 (a) Mouse-bites and (b) improved patterns and after development.

Next, coat a layer of AZ2020 [3.15] with a thickness of about 3 μm on the LOR_3A layer using the recipe in Table 3.4. For its soft-baking, 110°C and 90 seconds are used.

<div align="center">TABLE 3.4</div>
<div align="center">SPINNING RECIPE FOR AZ2020</div>

Step #	RPM	RPM/s	Time (s)
1	1000	1000	5
2	2890	5000	40

(3) Optical Lithography

Use a chrome-down mask for contact exposure under pressure mode for minimum 5 μm feature size. The exposure time is measured to be 25 seconds (125 mJ/cm^2) under a ultra-violet (UV) intensity of 5 mw/cm^2 for quartz-based mask material. For other mask

materials, e.g., soda lime, the exposure time should be compensated accordingly. A

recipe of 100°C and 90 seconds are used for post-baking.

(4) Development

After the post-baking, use a spinner with the recipe in Table 3.5 for development.

For a good metal adhesion during the deposition, the developed wafers need to be plasma

cleaned again for 30 seconds. The cross-sectional shape [3.15] after AZ2020

development is shown in Fig. 3.12.

TABLE 3.5
SPINNING RECIPE FOR DEVELOPMENT

Step #	RPM	RPM/s	Time (s)	Commentary
1	500	1000	3	Pre-treatment
2	500	250	3	Pre-treatment
3	500	250	90	Developer
4	500	500	45	Water (top side)
5	2500	1000	60	Water (back side)
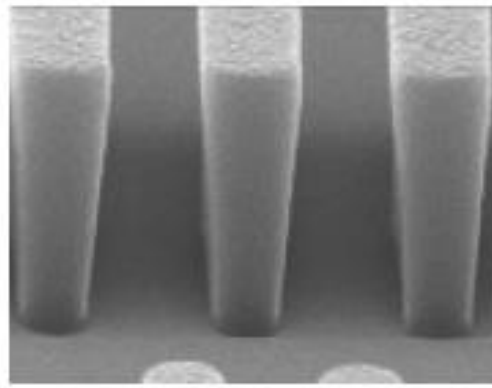
Fig. 3.12 Cross-sectional shape after AZ2020 development [3.15].

(5) Evaporation

Use Telemark's E-beam evaporator [3.16] for metal deposition. First, check the crystal sensor and renew it if necessary. Second, check the metal pellets if they are sufficient during the deposition. Third, load all wafers and face down the surface needs to be deposited. Forth, close the chamber, turn on the control and high-voltage button, and start the vacuuming step until the pressure is down to about 2×10^{-6} torr. In the followings, deposit all desired layers one by one, cool down the chamber below 70°C, and open the valve for a room atmospheric pressure. Finally, get all wafers out. A concise process flow from optical lithography to evaporation is shown in Fig. 3.13.
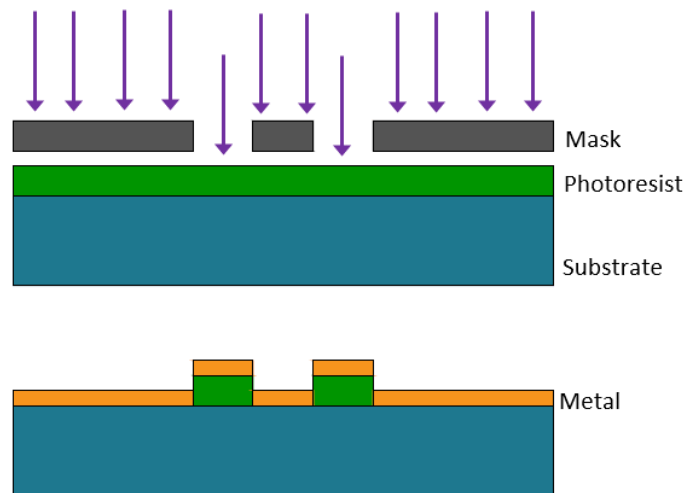
Fig. 3.13 Process flow from optical lithography to evaporation.

(6) Lift-off

Put all deposited wafers into an ultra-sonic bath with NMP solvent [3.17] for about 1 to 1.5 hours until all photoresists shaken off. Then dice chips out for measurement.

References

[3.1] E. Chen and S. Y. Chou, "Characteristics of coplanar transmission lines on multilayer substrates: Modeling and experiments," *IEEE Trans. Microwave Theory and Techn.*, vol. 45, no. 6, pp. 939-945, Jun. 1997.

[3.2] B. Kang, C. Jeiwon, C. Changyul, and K. Youngwoo, "Nondestructive measurement of complex permittivity and permeability using multilayered coplanar waveguide structures," *IEEE Microw. Wireless Compon. Lett.*, vol. 15, no. 5, pp. 381-383, May 2005.

[3.3] J. Svačina, "Analysis of multilayer microstrip lines by a conformal mapping method," *IEEE Trans. Microwave Theory and Techn.*, vol. 40, no. 4, pp. 769-772, Apr. 1992.

[3.4] M. Hofmann, G. Fischer, R. Weigel, and D. Kissinger, "Microwave-based noninvasive concentration measurements for biomedical applications," *IEEE Trans. Microwave Theory and Techn.*, vol. 61, no. 5, pp. 2195-2204, May 2013.

[3.5] I. F. Cheng, S. Senapati, X. Cheng, S. Basuray, H.-C. Chang, and H.-C. Chang, "A rapid field-use assay for mismatch number and location of hybridized DNAs," *Lab Chip*, vol. 10, no. 7, pp. 828-831, Feb. 2010.

[3.6] T. Chretiennot, D. Dubuc, and K. Grenier, "A microwave and microfluidic planar resonator for efficient and accurate complex permittivity characterization of aqueous solutions," *IEEE Trans. Microwave Theory and Techn.*, vol. 61, no. 2, pp. 972-978, Feb. 2013.

[3.7] High Frequency Structure Simulator. ANSYS, Inc., Canonsburg, PA, USA. [Online]. Available: http://www.ansys.com/Products/Simulation+Technology/Electromagnetics/Signal+Integrity/ANSYS+HFSS

[3.8] H. Weingärtner, A. Knocks, S. Boresch, P. Hochtl, and O. Steinhauser, "Dielectric spectroscopy in aqueous solutions of oligosaccharides: Experiment meets simulation," *J. Chem. Phys.*, vol. 115, no. 3, pp. 1463-1472, Jul. 2001.

[3.9] T. Sato, A. Chiba, and R. Nozaki, "Hydrophobic hydration and molecular association in methanol-water mixtures studied by microwave dielectric analysis," *J. Chem. Phys.*, vol. 112, no. 6, pp. 2924-2932, Feb. 2000.

[3.10] S. Tomić, S. D. Babić, T. Vuletić, S. Krča, D. Ivanković, L. Griparić, and R. Podgornik, "Dielectric relaxation of DNA aqueous solutions," *Phys. Rev. E*, vol. 75, no. 2, pp. 021905, Feb. 2007.

[3.11] R. Payne and I. E. Theodorou, "Dielectric properties and relaxation in ethylene carbonate and propylene carbonate," *J. Phys. Chem.*, vol. 76, no. 20, pp. 2892-2900, Sep. 1972.

[3.12] G. C. Franchini, A. Marchetti, M. Tagliazucchi, L. Tassi, and G. Tosi, "Ethane-1, 2-diol-2-methoxyethanol solvent system. Dependence of the relative permittivity and refractive index on the temperature and composition of the binary mixture," *J. Chem. Soc., Faraday Trans.*, vol. 87, no. 16, pp. 2583-2588, Aug. 1991.

[3.13] T. Sato and R. Buchner, "The cooperative dynamics of the H-bond system in 2-propanol/water mixtures: Steric hindrance effects of nonpolar head group," *J. Chem. Phys.*, vol. 119, no. 20, pp. 10789-10800, Nov. 2003.

[3.14] LOR_3A. MicroChem, Corp., Westborough, MA, USA. [Online]. Available: http://microchem.com/pdf/PMGI-Resists-data-sheetV-rhcedit-102206.pdf

[3.15] AZ2020. MicroChemicals, GmbH, Ulm, Germany. [Online]. Available: http://www.microchemicals.com/products/photoresists/az_nlof_2020.html

[3.16] Telemark's E-beam evaporator. Battle Ground, WA, USA. [Online]. Available: https://telemark.com/electron-beam-sources/

[3.17] NMP (1-methyl-2-pyrrolidone). MicroChemicals, Ulm, Germany. [Online]. Available: http://www.microchemicals.com/products/solvents/nmp.html

CHAPTER FOUR

AUTO-TUNING AND SELF-CALIBRATION OF

RADIO-FREQUENCY INTERFEROMETERS

4.1 Principle and Operation

For a matched design, the measured transmission coefficient S_{21} of the

interferometer in Fig. 2.3, 3.5, or re-drawn Fig. 4.1(a) is

$$S_{21} = K_1 \exp(-\gamma_{MUT} l_1) + K_2 \exp(-\gamma_{REF} l_1) \qquad (4.1)$$

where K_1 and K_2 include the effects of all the components in MUT and REF paths except

MUT and REF liquid sections; γ_{MUT} and γ_{REF} are the propagation constants of the

sections, and their length is l_1 (Fig. 4.1(b)). For high sensitivity MUT measurement at

frequency f_0, it is necessary to fine tune the interference process and to obtain very low

$|S_{21}|_{min}$ values (Fig. 4.1(a)). The tuning is achieved with high resolution tunable

attenuators. Currently, significant experience is needed with available commercial

devices. It is often challenging to keep the interferometer stable over a long period of

time. Thus, rapid measurements are important. Furthermore, calibration liquids are

needed to remove the unknown coefficients, i.e., K_i and γ_{REF} in eq. (4.1), in order to

quantify MUT permittivity. The accuracy of the calibration liquid properties and the

measurement repeatability are significant concerns, especially when the analyte

concentration level is very low. De-embedding approaches could avoid the use of

calibration liquids by measuring different calibration structures [4.1]. But measurement

repeatability of different structures is a challenge. In this chapter, it is demonstrated that

liquid-based attenuators can be exploited to automatically tune RF interferometer

sensitivity at high resolutions. Also, MUT solutions can be used to calibrate the measurement system, and enable rapid and quantitative measurements of MUT dielectric properties. No additional calibration standards or de-embedding structures are needed. Thus, the above mentioned problems are addressed.
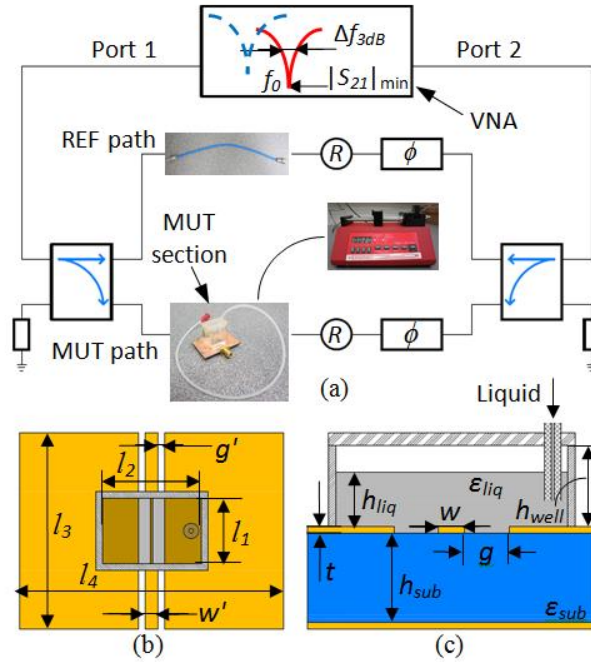
Fig. 4.1 (a) A schematic of the proposed RF interferometer with liquid attenuators. Another attenuator in the REF path can be replaced by a cable. The additional manually-tunable attenuators (R) and phase shifters (ϕ) are introduced for additional tuning flexibility. (b) Top view and (c) cross section of the liquid attenuator in (a), where w=0.13 mm, g=1.935 mm, t=17 μm, h_{well}=20 mm, h_{liq}: tunable, h_{sub}=0.787 mm, w'=2.2 mm, g'=0.9 mm, l_1=10 mm, l_2=15 mm, l_3=32 mm, l_4=40 mm, ε_{sub}=2.33, ε_{liq}: to be measured.

Figures 4.1(b) and (c) show the layout of a well-based tunable liquid attenuator

built on a CPW, which is fabricated with Duroid 5870 laminate by the milling machine in

Fig. 2.3. When MUT liquid, i.e., methanol-water solution, is used for tuning, the well is

simultaneously a sample holder. A syringe pump shown in Fig. 4.1(a) is used to infuse or

withdraw MUT liquid to or from the well with a pre-determined volume ΔV, which

effectively tunes the attenuation value. The attenuation resolution, which depends on

initial h_{liq} (Fig. 4.1(c)), ΔV, and MUT properties, can be very high since ΔV can be very

small, as indicated in Fig. 4.2. The curves are calculated with eqs. (2.2)-(2.6) in Chapter

II at ~3 GHz. Compared with digitally tunable attenuators, Fig. 4.2 indicates that the

liquid attenuator has better resolution. It also has larger dynamic range as well as

potentially smaller insertion loss and lower cost.
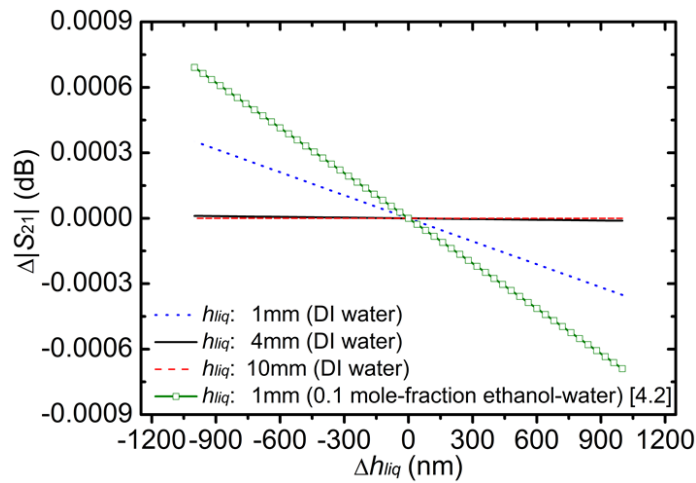
Fig. 4.2 Calculated $\Delta|S_{21}|$ of the attenuator in Fig. 1(b) when infuse (positive change) or

withdraw (negative change) lossy liquids. Δh_{liq} is referenced to the initial h_{liq}, at which

the characteristic impedance values are 48.677 Ω, 44.033 Ω, 43.717 Ω and 54.116 Ω. A

change of 54 nL liquid volume induces 360 nm Δh_{liq}. When Δh_{liq} is tuned from -1000 nm to +1000 nm, the impedance value changes are below 0.017 Ω. Thus, the attenuator is reasonably matched.

To evaluate the performance of the attenuator and the interferometer in Fig. 4.1, the well is initially filled with ~600 μL deionized (DI) water, which corresponds to an h_{liq} of ~4 mm. The $|S_{21}|_{min}$ in Fig. 4.1(a) is manually tuned to ~-70 dB, the corresponding f_0 and $|S_{21}|_{min}$ are the "starting point" in Fig. 4.3. Then the attenuator in Fig. 4.1(c) takes over the job for tuning $|S_{21}|_{min}$. DI water is withdrawn from the well at ~54 nL per step with ~1 second time interval between two steps. As a result, both $|S_{21}|_{min}$ and f_0 will change and reach a new (f_0, $|S_{21}|_{min}$) point in Fig. 4.3 until ($f_{0,min}$, $|S_{21}|_{min,min}$) is obtained. Further water withdrawal increase $|S_{21}|_{min}$ until it goes back to ~-70 dB. The pump is then switched to infuse water to the well. Thus, curve 2 in Fig. 4.3 is obtained. The procedure is repeated and stopped at the "ending point". The whole process took about 33 minutes.

53
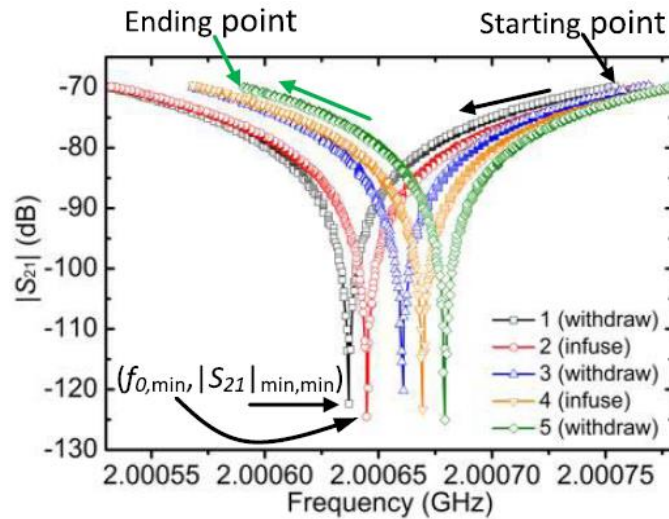
Fig. 4.3 Measured trajectory of (f_0, $|S_{21}|_{min}$) in Fig. 4.1(a) for repeated water infusion and withdrawal operations.

In Fig. 4.3, the interferometer has very high frequency resolution, consequently high sensitivity, at ($f_{0,min}$, $|S_{21}|_{min,min}$). Figure 4.4 shows three curves measured on the VNA in Fig. 4.1(a) around 5 GHz. To make the figure clearer, only the $|S_{21}|$ curve with ($f_{0,min}$, $|S_{21}|_{min,min}$), i.e., curve 1, and two adjacent curves, i.e., 2 and 3, are included. At point (5.0695322 GHz, ~-138.88 dB), the measured Q_{eff} is more than 1×10^8, which is exceptionally high and indicates outstanding frequency resolution. The Q_{eff} is comparable to or higher than those reported for optical resonators [4.2]. It is worth pointing out that lossy water, which significantly deteriorates the Q of resonators, is used in the measurement.

4.2 Quantitative Model for Complex Permittivity Extraction

To obtain quantitative $\varepsilon=\varepsilon'-j\varepsilon''$ of MUT, the coefficients $K_{1,2}$ and propagation constants $\gamma_{MUT,REF}$ in eq. (4.1) as well as h_{liq} for $|S_{21}|_{min,min}$ in Fig. 4.4 need to be obtained. As a result, 4 different measurements need to be used for data extraction. High sensitivity/accuracy consideration suggests using the measurements close to the one with $|S_{21}|_{min,min}$, i.e., curve 1 in Fig. 4.4, where MUT V_{min} is also uncertain. Using eq. (4.1), we have

$$S_{21,min,min} = K_1 \exp(-\gamma_{V_{min}} l_1) + K_2 \exp(-\gamma_{REF} l_1) \qquad (4.2)$$

Similarly, for $|S_{21}|$ at the same f_0, but measured immediately after drawing $\varDelta V$ (curve 2 in Fig. 4.4) or before drawing $\varDelta V$ (curve 3), the S-parameters are expressed as

$$S_{21,next} = K_1 \exp(-\gamma_{V_{min}-\varDelta V}l_1) + K_2 \exp(-\gamma_{REF}l_1) \tag{4.3}$$

$$S_{21,last} = K_1 \exp(-\gamma_{V_{min}+\varDelta V}l_1) + K_2 \exp(-\gamma_{REF}l_1) \tag{4.4}$$

Thus, we have

$$\frac{S_{21,last} - S_{21,min,min}}{S_{21,next} - S_{21,min,min}} = \frac{\exp(-\gamma_{V_{min}+\varDelta V}l_1) - \exp(-\gamma_{V_{min}}l_1)}{\exp(-\gamma_{V_{min}-\varDelta V}l_1) - \exp(-\gamma_{V_{min}}l_1)} \tag{4.5}$$

Additionally, another S_{21} curve next to curves 2 or 3 is needed.

The formula for calculating propagation constant $\gamma = \alpha + j\beta$ can be found in Chapter II and III. The parameters V_{min}, ε'_{liq}, and ε''_{liq} can be solved using eqs. (4.2)-(4.5) when mismatches in Fig. 4.1(a) are ignored, as discussed at the end of Section 2.2.
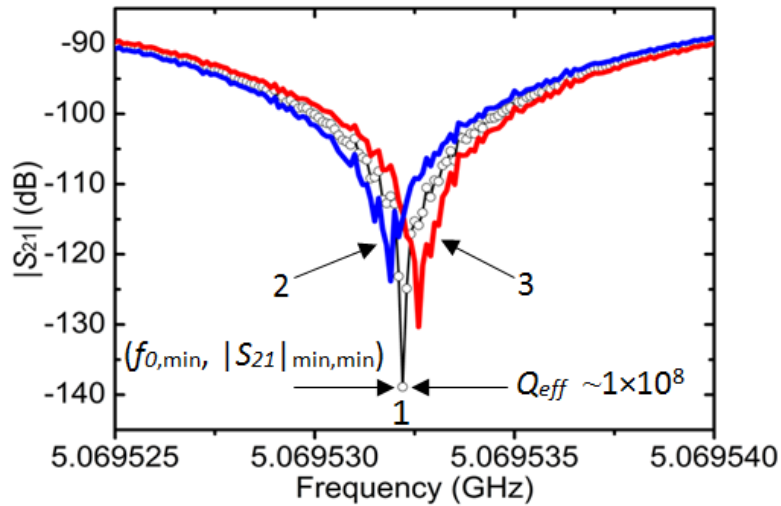
Fig. 4.4 Measured interferometer outputs when MUT is removed from the well at 54 nL/step. Curve 2 is one step after curve 1, which is one step after 3.

4.3 Model Validation and High-Sensitivity Measurement

First, the self-calibration method needs to be verified by measuring 0.005 mole fraction methanol-in-DI water (MUT) and comparing with the results reported in [4.3]. The liquid attenuator in Fig. 4.1(c) is also used as a sample holder. Approximately 600 μL MUT is infused to establish an initial h_{liq} in Fig. 4.1(c). Then the manual phase shifters and attenuators are used to tune $|S_{21}|_{min}$ to ~-80 dB at the desired frequency point. After that, the computer controlled syringe pump automatically infuses or withdraws MUT solutions to or from the well, ~54 nL per step. The measured scattering parameters are recorded until $|S_{21}|_{min,min}$ is identified. Repeat the process 4 times for the same frequency point before move to the next frequency point.

Using eqs. (4.2)-(4.5), the extracted complex permittivity at different frequencies of the methanol-water solution is shown in Table 4.1. They agree with the results in [4.3] reasonably well. Thus, our auto-tuning and self-calibration measurement procedures are validated.

TABLE 4.1
EXTRACTED COMPLEX PERMITTIVITY OF METHANOL-WATER
SOLUTION AT 0.005 MOLE FRACTION AND COMPARISON WITH THE DATA IN [4.3]

Freq. (GHz)	This work		[4.3]	
	Real	Imag	Real	Imag
2	77.1327 ±0.0063	7.6241 ±0.0034	77.1304	7.6212
3	76.1358 ±0.0005	11.2783 ±0.0004	76.1417	11.2692
4	74.8036 ±0.0056	14.7401 ±0.00005	74.8056	14.7372
6	71.2439 ±0.0021	20.9998 ±0.0097	71.2586	20.9673
7.5	68.0076 ±0.0016	24.9204 ±0.0004	68.0224	24.9164

Then, methanol-water solutions at 5×10^{-4} and 5×10^{-5} mole fractions are measured similarly at 3 GHz to further demonstrate the high sensitivity capabilities. The methanol concentrations are 10 and 100 times lower than that in [4.3], respectively. The obtained permittivity data, averaged from five independent measurements, are shown in Table 4.2. As expected, lower methanol concentration MUT has ε closer to that of water. The values are reasonable even though there are no published data for comparison. Thus, accurate permittivity values or small permittivity changes can be automatically measured without the need for additional calibration liquids or de-embedding procedures.

TABLE 4.2
MEASURED COMPLEX PERMITTIVITY OF METHANOL-WATER SOLUTIONS AT
0.005 (#0), 0.0005 (#1), 0.00005 (#2) MOLE FRACTIONS AND PURE DI WATER (#3)

#	Real	Imag
0	76.1358±0.0005	11.2783±0.0004
1	76.5192±0.0017	11.1125±0.0023
2	76.5479±0.0023	11.1048±0.0047
3	76.5462±0.0004	11.1097±0.00006

References

[4.1] J. C. Booth, N. D. Orloff, J. Mateu, M. Janezic, M. Rinehart, and J. A. Beall, "Quantitative permittivity measurements of nanoliter liquid volumes in microfluidic channels to 40 GHz," *IEEE Trans. Instrum. Meas*, vol. 59, no. 12, pp. 3279-3288, Dec. 2010.

[4.2] D. K. Armani, T. J. Kippenberg, S. M. Spillane, and K. J. Vahala, "Ultra-high-Q toroid microcavity on a chip," *Nature*, vol. 421, pp. 925-928, Feb. 2003.

[4.3] T. Sato, A. Chiba, and R. Nozaki, "Hydrophobic hydration and molecular association in methanol–water mixtures studied by microwave dielectric analysis," *J. Chem. Phys.*, vol. 112, no. 6, pp. 2924-2932, Feb. 2000.

CHAPTER FIVE

ANALYZING SINGLE GIANT UNILAMELLAR VESICLES

USING SLOTLINE SENSING STRUCTURE

5.1 Slotline-Based RF Sensor Design

Figure 5.1(a) shows the schematic of the RF sensor. Similar to the highly

sensitive and tunable RF interferometers in Chapter II-IV, two broadband quadrature

hybrids (QH) are used for RF probing signal division and combination. Off-chip tuning

components, phase shifters (Φ) and attenuators (R), are introduced to tune the sensor

sensitivity as well as the operating frequency. A slotline-based sensing structure, shown

in Figs. 5.1(b) and 1(c), is used to probe single GUVs. Unlike coplanar waveguide

transmission lines (CPWs) used in Chapter II-IV, slotlines are designed to yield higher

RF fields for the same gap dimension w (Fig. 5.1(c)), which is often limited by

fabrication techniques. Thus, stronger interactions between RF fields and GUVs [5.1] can

be obtained for higher sensor sensitivities. Furthermore, better one-dimensional (1-D)

spatial resolution can be achieved since a slotine has only one gap, unlike a CPW with

two gaps and a signal line.

Baluns for nanometer slotline to CPW transitions [5.2] are shown in Fig. 5.1(a).

CPWs are convenient for measurements. The RF structures, including the slotline and the

baluns, are integrated on a fused-silica substrate through conventional micro-fabrication

procedures. Lift-off processes are used, same as that in Section 3.5, for the deposition of

Ti/Au (20 nm / 200 nm) films. A focused ion beam (FIB) is used to form the 100 nm

slotline. Figure 5.2 shows the simulated and measured performance of the RF structure

around the designed center frequency, 3 GHz, around which the measurement will be performed. The simulation is conducted with HFSS. Low return loss and insertion loss are achieved for sensor operations. Factors that cause discrepancies between measurements and simulations include metal line dimension and cross-section deviations from layout, which is used for simulations. SMA female connectors and conductive epoxy used for measurement connection are also not taken into consideration in simulation.
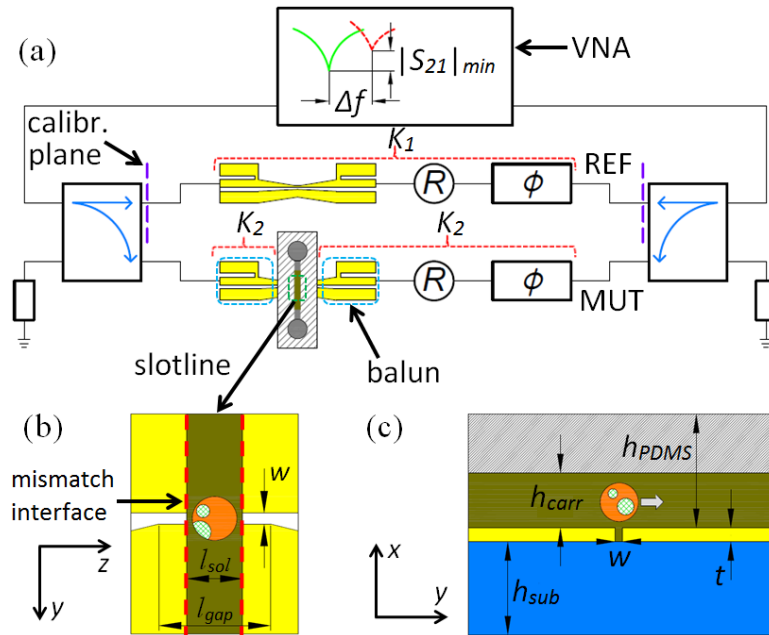
Fig. 5.1 (a) Schematic of the RF sensor. (b) The top and (c) cross section views of the sensing zone in (a) with single GUV (circle), where dimensions w=100 nm (gap), t=220 nm (Ti/Au), h_{carr}=50 μm (channel height), h_{sub}=1 mm (substrate), h_{PDMS}=~2 mm (PDMS cover), l_{sol}= 50 μm (channel width), and l_{gap}=100 μm. The dimension for the CPW is 0.1 mm / 1.5 mm / 0.1 mm (gap/signal line/gap). Abbreviations MUT and REF represent

material-under-test and reference branches, respectively. Coefficients K_1, K_2 will be used to describe effects of indicated components. Φ and R represent phase shifters and attenuators, respectively. The Cartesian coordinate systems are marked for (b) and (c). The mismatch interfaces for impedance are marked by red dash lines in (b).
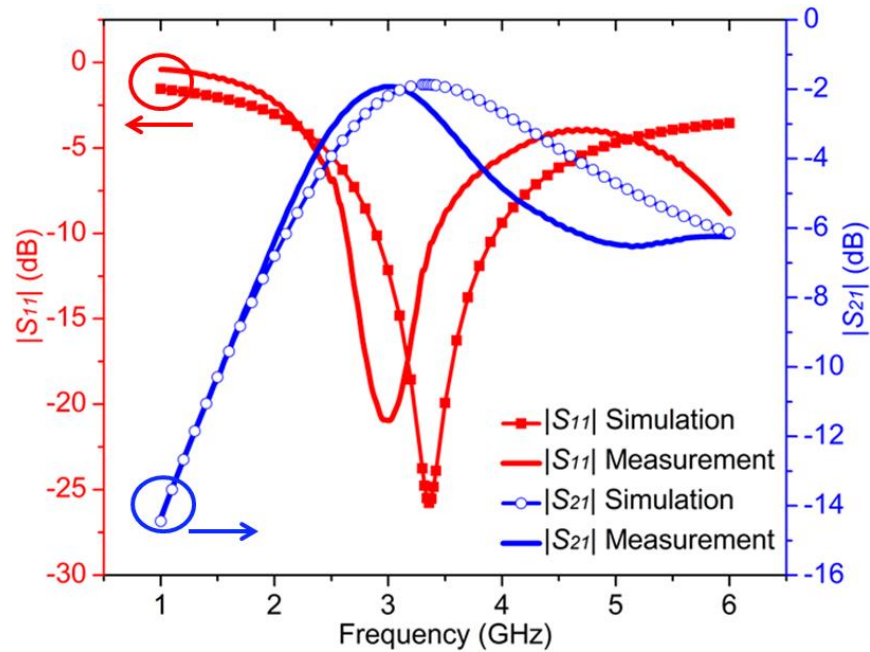
Fig. 5.2 *S*-parameters of the nanometer RF sensing structure.

Compared with the previous sensors that have millimeter (mm) in Chapter II, III and IV, and micrometer (μm) gaps in Chapter III, the RF electric fields of the 100 nm slotline are concentrated to achieve much stronger GUV-RF field interactions. Figure 5.3 depicts the electric field distribution at 3 GHz around the gap obtained with HFSS simulation. Minor asymmetry may be caused by simulation meshes, for which 0.5 μm is used as the maximum length of mesh elements due to a compromise between simulation

accuracy and simulation time. For 5 dBm input power (used in the measurements), the electric field intensity is up to $\sim 1.76 \times 10^7$ V/m around the sensing zone. In comparison, for the sensors with mm and μm gaps, the maximum electric field intensities are $\sim 1.33 \times 10^3$ and $\sim 1.73 \times 10^5$ V/m, respectively. Thus, the absolute sensitivity of the sensor is significantly improved, as illustrated by eq. (5.22) and (5.24) below.
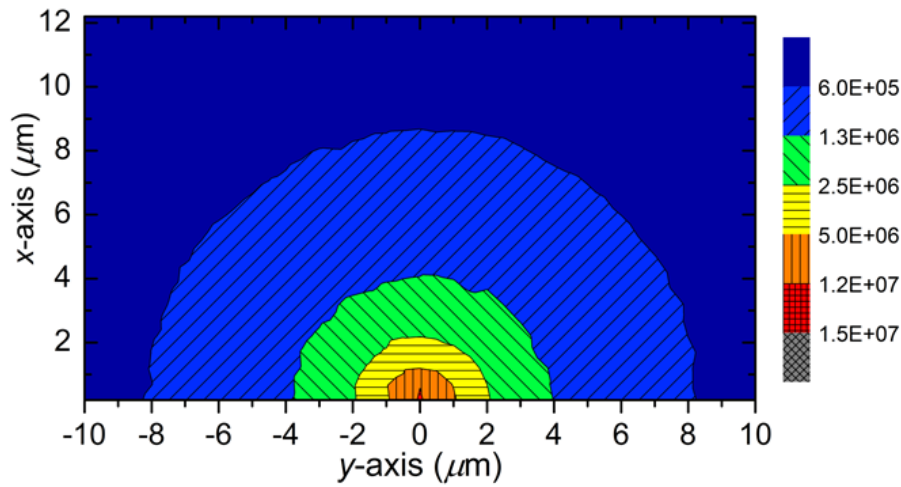
Fig. 5.3 Simulated distribution of electric field intensity (unit: V/m) around the sensing zone (axis origin corresponds to the gap in Fig. 1(c)).

A polydimethylsiloxane (PDMS) microfluidic channel with a cross-section of 50 μm $\times 50$ μm is built and incorporated with the slotline in the MUT branch. The GUV solution is injected into and extracted from the channel through two soft plastic tubes (not shown in Fig. 5.1) that are attached to the circular openings of the channel.

5.2 Extraction of GUV Dielectric Property

The introduction of a GUV particle, Fig. 1(c), will change the effective permittivity of the overall slotline structure and its *S*-parameters measured by the vector network analyzer (VNA). As a result, the particle properties can be obtained with the models based on the conformal mapping method and perturbation method presented below in this work.

(1) Conformal mapping method

The transmission *S*-parameter recorded by the VNA in Fig. 1(a) can be expressed as

$$S_{21,sol} = \frac{\sqrt{2}}{2} e^{j0} K_1 \frac{\sqrt{2}}{2} e^{j0} + \frac{\sqrt{2}}{2} e^{j\frac{\pi}{2}} K_2 e^{-\gamma_{sol} l_{sol}} \frac{\sqrt{2}}{2} e^{j\frac{\pi}{2}} \qquad (5.1).$$

Subscript *sol* indicates solution. The propagation constant of the slotline section is γ_{sol} with a physical length of l_{sol}. The coefficients K_1 and K_2 describe the effects of all the other sensor components, including cables, attenuators and phase shifters. K_1 also includes the slotline, and can be measured independently using a calibrated VNA, as illustrated in Fig. 5.1(a). When a GUV flows above the slotline gap, the strong interaction between the electric field and GUV causes $|S_{21}|$ to be

$$S_{21,solp} = \frac{\sqrt{2}}{2} e^{j0} K_1 \frac{\sqrt{2}}{2} e^{j0} + \frac{\sqrt{2}}{2} e^{j\frac{\pi}{2}} K_2 e^{-\gamma_{sol}(l_{sol}-l_{solp})-\gamma_{solp} l_{solp}} \frac{\sqrt{2}}{2} e^{j\frac{\pi}{2}} \qquad (5.2)$$

where the subscript *solp* is for solution with single GUV particle, as shown in Fig. 5.1(c). It is proved that for solutions with and without single GUV, which have close permittivity values, γ_{solp} can be solved using eqs. (5.1) and (5.2) when mismatches at the interfaces, as shown in Fig. 5.1(b), between microfluidic channel section of MUT/REF

branch and transmission lines, are ignored. For a solution with known permittivity, the

propagation constant $\gamma_{sol} = \alpha_{sol} + j\beta_{sol}$ can be obtained from

$$\alpha_{sol} = \frac{\pi}{\lambda_0} \frac{\varepsilon''_{eff,sol}}{\sqrt{\varepsilon'_{eff,sol}}} \tag{5.3}$$

$$\beta_{sol} = \frac{2\pi f}{v_{ph}} = \frac{2\pi f}{\sqrt{\varepsilon_0 \varepsilon'_{eff,sol} \mu_0}} \qquad . \tag{5.4}$$
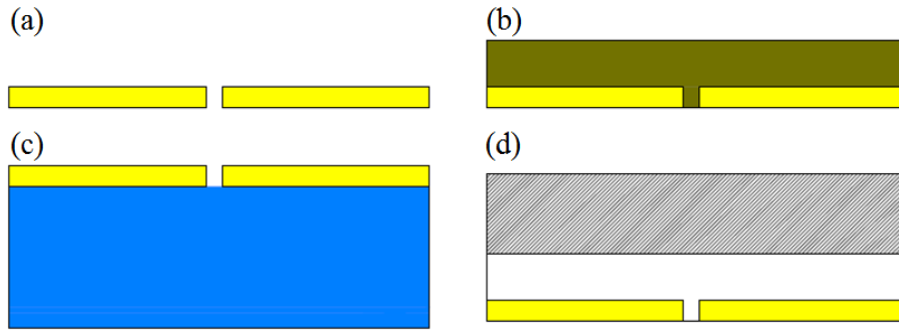
Fig. 5.4 Configurations of partial capacitances: (a) C_{air}, (b) C_{carr}, (c) C_{sub}, and (d) C_{PDMS}.

The capacitance of a uniform slotline with the cross section shown in Fig. 5.1(c)

can be approximated as the superposition of four partial capacitances C_{air}, C_{carr}, C_{sub} and

C_{PDMS}, as shown in Fig. 5.4 [5.3]. Then, ε'_{eff} and ε''_{eff} can be obtained through,

$$\varepsilon'_{eff,sol} = \frac{C_{air} + C_{sub}(\varepsilon'_{sub}) + C_{carr}(\varepsilon'_{carr}) + C_{PDMS}(\varepsilon'_{PDMS})}{C_{air}} \tag{5.5}$$

$$\varepsilon''_{eff,sol} = \frac{C_{carr}(\varepsilon''_{carr})}{C_{air}} \tag{5.6}$$

where the subscript sub refers to the substrate, e.g., $\varepsilon'_{sub} = 3.75$ for fused silica, while the

subscript $carr$ stands for the carrier solution of the particle. Only the dielectric loss

coming from the solution is considered in eq. (5.6). The expressions for the capacitances

in eqs. (5.5) and (5.6) are

$$C_{air} = 2\varepsilon_0 \frac{K(k'_0)}{K(k_0)} \tag{5.7}$$

$$C_{sub}(\varepsilon_{sub}) = \varepsilon_0(\varepsilon_{sub} - 1)\frac{K(k'_{sub})}{K(k_{sub})} \tag{5.8}$$

$$C_{carr}(\varepsilon_{carr}) = \varepsilon_0\varepsilon_{carr}\frac{K(k'_{carr})}{K(k_{carr})} \tag{5.9}$$

$$C_{PDMS}(\varepsilon_{PDMS}) = \varepsilon_0(\varepsilon_{PDMS} - 1)\frac{K(k'_{PDMS})}{K(k_{PDMS})} - \varepsilon_0\varepsilon_{PDMS}\frac{K(k'_{carr})}{K(k_{carr})} \; . \tag{5.10}$$

The functions K in eqs. (5.7)-(5.10) are incomplete elliptic integral of the first

kind with variable $k_{0,sub,carr,PDMS}$ as

$$k_{0,sub,carr,PDMS} = \sqrt{\frac{2\tanh(0.5\pi w / h_{0,sub,carr,PDMS})}{1 + \tanh(0.5\pi w / h_{0,sub,carr,PDMS})}} \tag{5.11}$$

where metal film thickness t is assumed to be negligible, w is the gap width of the

slotline, $h_{sub,carr,PDMS}$ are thicknesses of substrate, solution and PDMS layers, and a

semiempirical expression for the quasi-static non-frequency dependent approximation of

distance h_0 is [5.3]

$$h_0 = h_{PDMS}\left(1 + \frac{133}{2 + \varepsilon'_{PDMS}}\right) \tag{5.12}$$

and $k' = (1 - k^2)^{0.5}$.

The obtained $\gamma_{solp} = \alpha_{solp} + j\beta_{solp}$ from eqs. (5.1) and (5.2) is used to extract the

complex permittivity of the particle, where the expression for α_{solp} and β_{solp} are the same

as eqs. (5.3) and (5.4) with different subscripts. The partial capacitances in eqs. (5.5) and

(5.6) have to be modified to include the dielectric and physical properties of single particles. As shown in Fig. 5.6, the carrier solution layer is split into upper and bottom layers (subscripts: *upp* and *bott*), and a particle-solution layer (subscript: *ps*), where it is assumed that the particle can be treated as a cylinder to acquire the unit length capacitance using the conformal mapping method. The validity of this assumption will be discussed later. So $\varepsilon'_{eff,solp}$ and $\varepsilon''_{eff,solp}$ should be rewritten as

$$\varepsilon'_{eff,solp} = \frac{C_{air} + C_{sub}(\varepsilon'_{sub}) + C_{upp}(\varepsilon'_{carr}) + C_{ps}(\varepsilon'_{p}, \varepsilon'_{carr}) + C_{bott}(\varepsilon'_{carr}) + C_{PDMS}(\varepsilon'_{PDMS})}{C_{air}} \quad (5.13)$$

$$\varepsilon''_{eff,solp} = \frac{C_{upp}(\varepsilon''_{carr}) + C_{ps}(\varepsilon''_{p}, \varepsilon''_{carr}) + C_{bott}(\varepsilon''_{carr})}{C_{air}} \quad (5.14)$$

where $\varepsilon'_p - j\varepsilon''_p$ is the complex permittivity of the particle, and the expressions for the capacitances, C_{upp} and C_{bott}, are

$$C_{upp}(\varepsilon_{carr}) = \varepsilon_0 \varepsilon_{carr} \left(\frac{K(k'_{carr})}{K(k_{carr})} - \frac{K(k'_{upp})}{K(k_{upp})} \right) \quad (5.15)$$

$$C_{bott}(\varepsilon_{carr}) = \varepsilon_0 \varepsilon_{carr} \frac{K(k'_{bott})}{K(k_{bott})} \quad . \quad (5.16)$$

The variables k_{upp} and k_{bott} in eqs. (5.15) and (5.16) are

$$k_{upp} = \sqrt{\frac{2\tanh(0.5\pi w / (SC + R))}{1 + \tanh(0.5\pi w / (SC + R))}} \quad (5.17)$$

$$k_{bott} = \sqrt{\frac{2\tanh(0.5\pi w / (SC - R))}{1 + \tanh(0.5\pi w / (SC - R))}} \quad (5.18)$$

where *SC* and *R* are the spherical-center coordinate and radius of the particle, respectively. It can be found from Fig. 5.5 that $h_{upp}=SC+R$ ($\theta=\pi/2$) and $h_{bott}=SC-R$ ($\theta=-\pi/2$) with θ shown in Fig. 5.5.
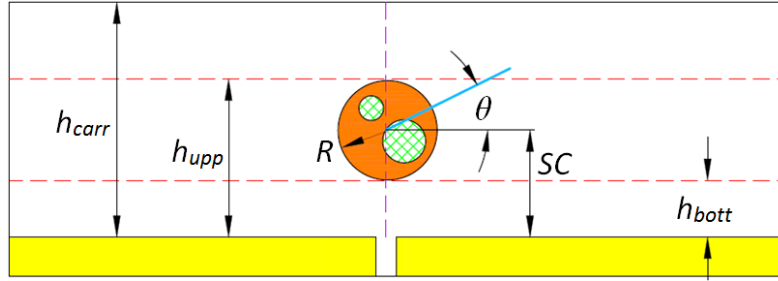
Fig. 5.5 Partition of the carrier layer (horizontal dash line), and magnetic wall (vertical dash line) with single GUV (solid circle with two meshed circles marked as microdomains on it).
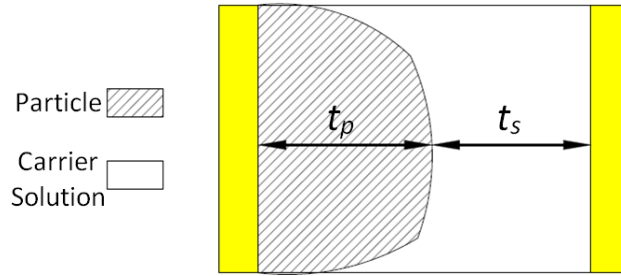
Fig. 5.6 Two-dimensional conformal mapping of particle-solution layer (*w* plane).

For the particle-solution layer, dielectrics in the mapped capacitance consist of two parts: particle and carrier solution, as shown in Fig. 5.6. Transforms eqs. (1) and (2) in [5.3] are used to map the particle-solution layer from *z* plane to *w* plane. Capacitance C_{ps} is in the form of

$$C_{ps}(\varepsilon_p, \varepsilon_{carr}) = \int_{-\pi/2}^{\pi/2} \frac{\dfrac{K'(\sqrt{\dfrac{1-\tanh(0.5\pi(SC+R\sin\theta)/h_0)}{1+\tanh(0.5\pi(SC+R\sin\theta)/h_0)}})}{K(k'_0)}}{\dfrac{1}{\varepsilon_p \dfrac{K(k'_x)}{K(k_x)}} + \dfrac{1}{\varepsilon_{carr}(\dfrac{K(k'_0)}{K(k_0)} - \dfrac{K(k'_x)}{K(k_x)})}} d\theta \qquad (5.19)$$

66

where $K'(f(\theta)) = \mathrm{d}(K(f(\theta)))/\mathrm{d}\theta$, and the coefficient k_x is also a function of the angle θ

$$k_x = \sqrt{\frac{2\tanh(0.5\pi w \tanh(0.5\pi R \cos\theta / (SC + R\sin\theta)) / h_0)}{1 + \tanh(0.5\pi w \tanh(0.5\pi R \cos\theta / (SC + R\sin\theta)) / h_0)}} \quad . \tag{5.20}$$

In eq. (5.19), the terms '$(K(k'_x)/K(k_x))^{-1}$' and '$(K(k'_0)/K(k_0)-K(k'_x)/K(k_x))^{-1}$' represent the dielectric thicknesses for particle and solution, i.e., t_p and t_s in Fig. 5.6, respectively, corresponding to a given θ. Figure 5.7 shows normalized t_p and t_s versus θ (from $-\pi/2$ to $\pi/2$) for different SCs and Rs. The parameters for Case #0 in Fig. 5.7 will be used to extract complex permittivity in Section 5.4. Based on this, for Case #1 and #2, R and w are changed, respectively, to demonstrate their independent effect on t_p and t_s. Figure 5.7 shows that (*i*) the vertical position has a more significant effect than the radius through Case #0 and #1; (*ii*) the dielectric thickness in Fig. 5.6 increases with increased radius for the same vertical position through Case #1 and Case #2.

The GUV sphere is treated as a cylinder, which may cause significant errors, partly due to increased volume. A coefficient fitting factor $\kappa=0.67$, which is also the volume ratio of the sphere and the approximated cylinder, is introduced to revise l_{solp} as $2\kappa R$.

Thus, the dielectric property of the measured particle can be obtained. Figure 5.8 summarizes the algorithm to obtain GUV permittivity values from *S*-parameters.

The conformal mapping method gives an intuitive and closed-form model for analyzing GUV permittivity from measured *S*-parameters. Yet, conformal mapping is rigorous for the analysis of two-dimensional direct-current (DC) systems or RF transverse-electromagnetic (TEM) systems. Although the slotline in Fig. 5.1 may be

approximated as a quasi-TEM system for the targeted frequency band, which is relatively narrow, GUVs are, in fact, three-dimensional objects. Therefore, the validity of the above model needs to be examined. This is accomplished by the experimental results presented in Section IV and by using a second modeling approach, discussed below.
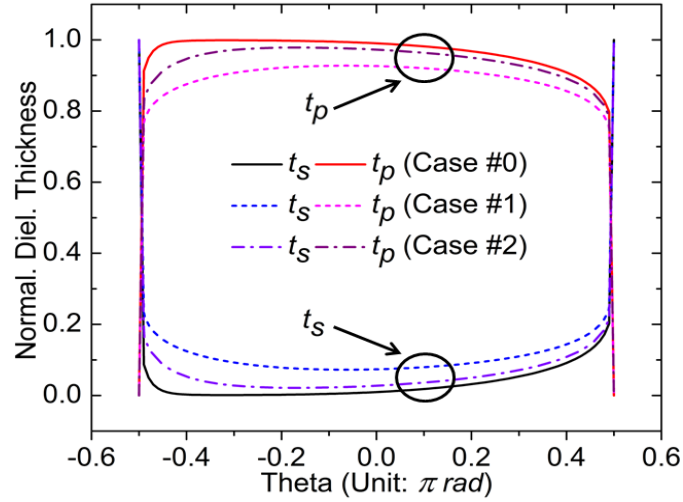
Fig. 5.7 t_p and t_s versus θ for: case #0, w=100 nm, SC=6 μm, R=5 μm; case #1, w=100 nm, SC=15 μm, R=5 μm; case #2, w=100 nm, SC=20 μm, R=10 μm.
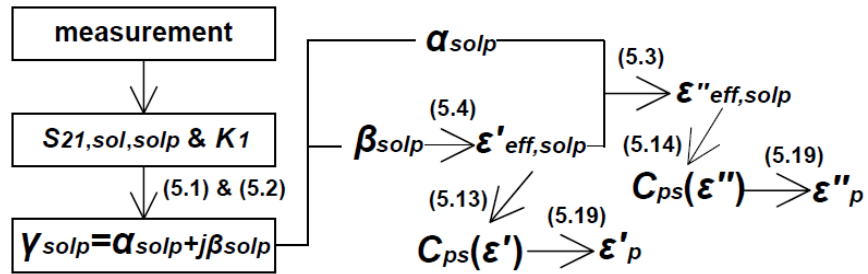
Fig. 5.8 Algorithm to obtain GUV permittivity values from S-parameters.

(2) Perturbation method

It is assumed that the GUV particle in Fig. 5.1(c) only slightly perturbs the RF electric and magnetic fields of the slotline. Therefore, the un-perturbed RF fields can be used to calculate the interactions between the GUV and the RF fields. As a result, the new propagation constants of the slotline section, $\gamma_{sol,solp}$ in eqs. (5.1) and (5.2), can be obtained. So can the GUV properties. This assumption is reasonable since the RF properties of GUVs are expected to be close to those of the carrier liquids.

It is possible to obtain an approximate, closed-form analytical solution of slotline RF fields (without GUVs). The fields can also be obtained using simulation tools, such as COMSOL Multiphysics tools [5.4]. The time cost of a single simulation is acceptable. Figure 5.9 shows the distributions of RF fields at the cross section in Fig. 5.1(c) with the dimensions given in Table 5.1 (only a part of the channel is shown), where ε_{carr}=76.05-j10.34 (glucose-water solution at 2.8 GHz [5.5]). The green circle indicates the location of a GUV, which is not included in the simulation for Fig. 5.9.

TABLE 5.1
PARAMETERS USED FOR ESTIMATING $/S_{21}/_{\min}$

Parameter	Symbol	Value
Thickness of PDMS	h_{PDMS}-h_{carr}	2 mm
Relative dielectric constant of PDMS	ε_{PDMS}	2.5
Thickness of substrate	h_{sub}	1 mm
Relative dielectric constant of substrate	ε_{sub}	3.75
Width of microfluidic channel	l_{sol}	50 μm
Height of microfluidic channel	h_{carr}	50 μm
Radius of GUV	R	5 μm
Spherical-center coordinate of GUV	SC	6 μm
Width of slotline gap	w	100 nm
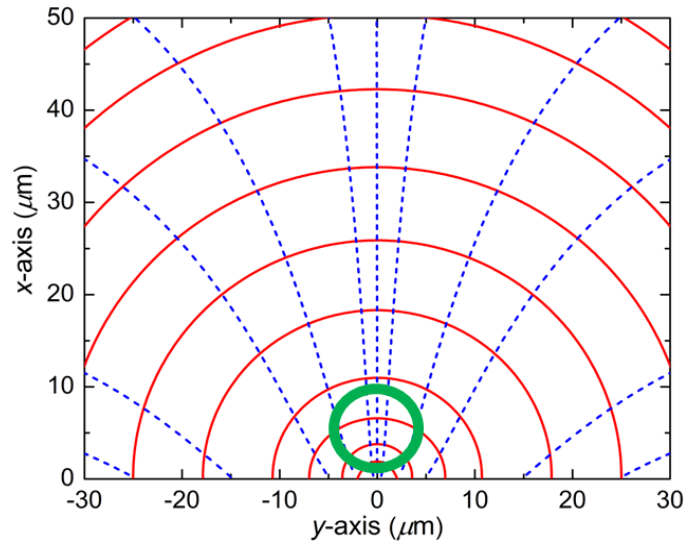
Fig. 5.9 Cross-sectional distributions of EM fields. Red semi-circle clusters: electric field; blue parabola clusters: magnetic field. The bold green circle indicates the location of the GUV particle (*x-y* plane corresponding to the cross section in Fig. 5.1, and the origin is selected at the center of the gap).

With the obtained RF field data and equations eqs. (2.17)-(2.20) in [5.1], equivalent circuit parameters *L*, *C*, *R* and *G* of the GUV loaded slotline can be obtained with a priori GUV properties. Corresponding $\gamma_{sol,solp}$ and *S*-parameters are obtained. This process is iterated with new GUV property values until the best match between the calculated and measured *S*-parameters is achieved. The time cost of this numerical iteration approach is significantly lower than that of full wave simulations of RF fields for each iteration step. The following are the main considerations.

The 10 μm diameter GUV sphere is divided into smaller elements using Wolfram Demonstrations Project [5.6], Fig. 5.10, which has 4,999 cubes with a side length of 0.5

μm, and 21 cubes along the diameter direction. A similar division is made for the carrier solution, not shown in Fig. 5.10.
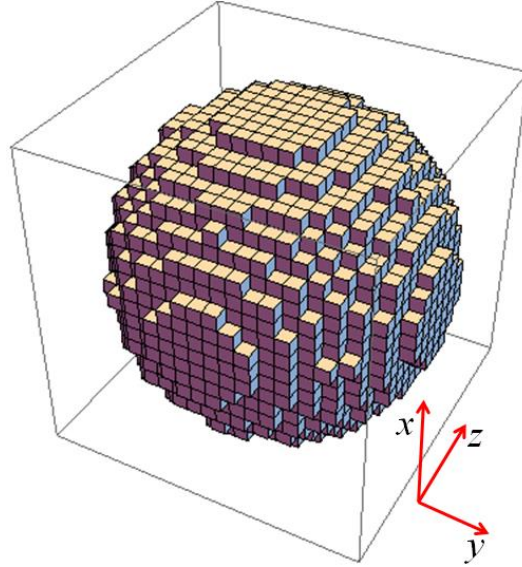
Fig. 5.10 Approximating a 10 μm diameter sphere with 4,999 cubes (x-y plane corresponding to the cross section in Fig. 5.1).

Along the z-axis direction, there are 21 layers. For layer i, the corresponding parameters L_i, C_i, R_i and G_i can be calculated once their ε and μ are given.

$$L_i = \frac{1}{|I_0|^2}\left(\sum_{N_i}\mu_{N_i}\,|H_{xy}|^2\Delta S_{N_i} + \sum_{M_i}\mu_{M_i}\,|H_{xy}|^2\Delta S_{M_i}\right) \qquad (5.21)$$

$$C_i = \frac{1}{|V_0|^2}\left(\sum_{N_i}\varepsilon_{N_i}\,'|E_{xy}|^2\Delta S_{N_i} + \sum_{M_i}\varepsilon_{M_i}\,'|E_{xy}|^2\Delta S_{M_i}\right) \qquad (5.22)$$

$$R_i = \frac{R_s}{|I_0|^2}\sum_{T_i}|H_{xy}|^2\,\Delta l_{M_i} \qquad (5.23)$$

$$G_i = \frac{\omega}{|V_0|^2}\left(\sum_{N_i} \varepsilon_{N_i}"|E_{xy}|^2\Delta S_{N_i} + \sum_{M_i} \varepsilon_{M_i}"|E_{xy}|^2\Delta S_{M_i}\right) \qquad (5.24)$$

where E_{xy} and H_{xy} are RF field intensities in the x-y plane, which are assumed to be

uniform within one element; parameters Δl and ΔS are the length and area of one element;

the subscript N_i describes a GUV element while subscript M_i for any non-GUV element,

including solution, substrate, channel, PDMS, and air; parameter T_i is determined by the

boundary lines on conductors in Fig. 5.1(c). In this example, Δl=0.5 μm, ΔS=0.25 μm^2,

T_i=6,400 (two 800 μm long conductors), and for the first layer, N_1= 37 (countable in Fig.

5.10), M_1 (channel part)=32,000-N_1=319,963 (for a 1600 μm $\times$ 50 μm channel); for other

layers, N_i and M_i can also be found accordingly. The definitions for other parameters are

the same as those in [5.1]. Then the propagation constant γ_i for each layer can be solved

by γ_i={$(R_i+j\omega L_i)(G_i+j\omega C_i)$}$^{0.5}$, and γ_{solp} for the microfluidic channel with single GUV can

be considered as a set of γ_i. So the term $\gamma_{solp}l_{solp}$ in eq. (5.2) can be expressed as

$$\gamma_{solp}l_{solp} = \sum_{i=1}^{21}\gamma_i\Delta l_i \qquad (5.25)$$

where Δl_i is the length of layer i along the z-axis, e.g., 0.5 μm in this example.

The results from eq. (5.25) are compared with measured results until the

following conditions are satisfied with a set of ε_p:

$$|\text{Re}(\gamma_{solp}l_{solp})_{measured} - \text{Re}(\gamma_{solp}l_{solp})_{calculated}| < \delta \qquad (5.26)$$

$$|\text{Im}(\gamma_{solp}l_{solp})_{measured} - \text{Im}(\gamma_{solp}l_{solp})_{calculated}| < \delta \qquad (5.27)$$

where δ, e.g., 0.0001, represents the error tolerance.

In addition to extracting cell particle properties, the models above can also be used to rapidly predict the required $|S_{21}|_{min}$ for a given RF interferometer to measure a given particle using

$$| S_{21,solp} - S_{21,sol} | = | e^{-\gamma_{solp}l_{solp}} - e^{-\gamma_{sol}l_{solp}} | \quad . \qquad (5.28)$$

Table 5.2 summarizes the estimations for different dielectric properties, where we choose ε_{carr}=76.05-j10.34 (glucose-water solution at 2.8 GHz [5.5]), and ε_p is changed from 74.55-j11.84 to 10-j1. The other parameters are given in Table 5.1. The results indicate reasonable agreement between HFSS full-wave simulation and model analysis. The effects of particle radius and vertical position on the required $|S_{21}|_{min}$ can also be evaluated. It should be pointed out that higher sensitivity (or lower $|S_{21}|_{min}$) in actual measurements is always required because of system losses (i.e., $|K_2|<1$ in eq. (5.2)) which is not considered in the above estimation.

TABLE 5.2
ESTIMATED MINIMUM REQUIRED $/S_{21}/_{min}$

ε_p	$/S_{21}/_{min}$ (dB)		
	Model #1	Model #2	HFSS
74.55-j11.84	-99.46	-106.99	-108.73
73.55-j12.84	-97.78	-102.55	-96.66
60-j25	-82.45	-86.78	-77.42
10-j1	-68.60	-77.04	-72.53

For Model #2, the RF electric and magnetic fields, as shown in Fig. 5.9, are simulated without the GUV. In reality, the GUV tends to change the field distribution around it due to the dielectric property difference between the GUV and the carrier solution. So $|S_{21}|_{min}$ calculated using Model #2 is always lower than that using Model #1.

Moreover, both Models #1 and #2 are based on the assumption of quasi-static TEM while HFSS is based on full-wave analysis. They tend to obtain different results.

The advantage of Model #2 is that there are no complex transformation expressions for conformal mapping, like eq. (1) and (2) in [5.3]. The FEM (finite element method)-based direct-current (DC) simulation to obtain the electric and magnetic fields $|E|$ and $|H|$ is relatively easy, even for some more complex structures for which there are no transformation expressions for conformal mapping. However, no closed-form analytical expression is obtained for Model #2 to describe effect of every structureal parameter, e.g., w, h_{PDMS}, h_{sub}, and h_{carr} in Fig. 5.1.

5.3 GUV Synthesis and RF Measurements

The electroformation method [5.7] is adopted for GUV synthesis. Chol (Cholesterol), POPC (16:0-18:1 PC 1-palmitoyl-2-oleoyl-sn-glycero-3-phosphocholine) and SM (16:0 Egg Sphingomyelin) in chloroform are mixed at different mole fractions to form coexisting liquid-ordered phase L_o and liquid-disordered phase L_α (L_o+L_α) (Group *I*), liquid-ordered phase L_o (Group *II*), and liquid-disordered phase L_α (Group *III*) [5.8], as shown in Fig. 5.11 obtained with an epi-fluorescence microscope with an ET-FITC/CY3 Filter. Two fluorescent labels, Rho-PE (2-dioleoyl-sn-glycero-3-phosphoethanolamine-N-(lissamine rhodamine B sulfonyl) (ammonium salt)) and DioC18 (3,3'-Dioctadecyloxacarbocyanine Percholorate) are used for liquid-disordered phase L_α and liquid-ordered phase L_o domains, respectively. Three groups of GUV particles are

synthesized with different molecular compositions (molar fraction) of POPC/SM/Chol: 2/1/1 (*I*), 1/2/2 (*II*), and 8/1/1 (*III*).
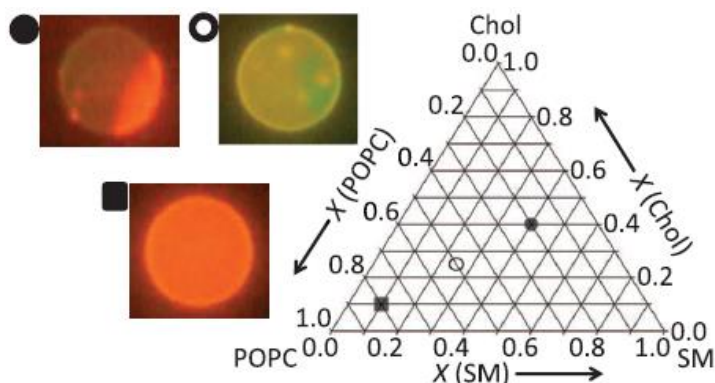
Fig. 5.11 Images of synthesized GUVs at different molecular compositions POPC/SM/Chol shown on a ternary composition diagram (hollow circle, *I*: 2/1/1; solid circle, *II*: 1/2/2; solid square, *III*: 8/1/1). Liquid-disordered phase L_α: red; liquid-ordered phase L_o: green.

The main electroformation steps are the following:

(1) Sample preparation

Before starting to preparation, all powered lipids should be solubilized by chloroform to be 10 mg/mL and stored in amber bottles with resistant cap at -20°C. Prior to GUV Synthesis, the bottles should be taken out from the storage freezer and place at the room temperature for 40~60 minutes. At the same time, clean several indium tin oxide (ITO)-coated glass slides using kimwipes rinsed by ethanol. One GUV sample needs two slides. To avoid possible scratching and stripping on the glass surface, some

harsh wipes, e.g., paper towels, should be not used. And, the conductive ITO-coated surface needs to be identified using a multimeter and then labeled, which will applies AC (alternating current) voltage in step (5). Place all slides face up on a 55°C hotplate for 15 minutes.

(2) Lipids mixing

Fill two glass test tubes, i.e., one for washing, and another one for lipids mixing (~75% full with chloroform). Then clean several Hamilton syringes with different ranges with chloroform. If the lipids-chloroform solutions are solubilized to be 10 mg/mL, as done in Step (1), add 120 μL chloroform into a single glass test tube for each sample. Then add appropriate mounts of lipids into the test tube. For every sample, a total lipids weight should be 350 μg. Taking the mentioned POPC/SM/Chol: 2:1:1 (Group #*I*) for example, from Table 5.3, one can calculate that the represent amounts for them are 20.39 μL, 9.43 μL, and 5.19 μL, respectively. Fluorescent labels (1 μL for each) should be also added at this step.

TABLE 5.3
CALCULATION OF LIPID AMOUNT

Lipid	Mixtures Mol wt (g/mol)	Mol %	Vol of each (μL)
16:0-18:1 POPC	760.1	50	20.39
16:0 SM	703	25	9.43
Chol	386.66	25	5.19

Drop 80 μL Chol/lipids/labels mixture chloroform solution onto the top 1/3 of one glass slide, then use a glass pipet to gently spread out the drop limited on the top 1/3 of

the slide. At this step, the lipid mixture between the pipet and the slide should be uniform from the left to the right. Before the chloroform is completely evaporated, stop the spreading job shortly. Then leave the slide onto the hotplate at 55°C for 15 minutes.

(3) Vacuum drying lipids-coated slides

Put all lipids-coated and dried slides from the hotplate into a vacuum desiccator at a pressure of 60~70 mm *torr* for 2 hours at least. The chamber should be completely covered in dark preventing lipid oxidation if one needs an overnight drying.

(4) Sandwiching of samples

Place a big O-ring rubber in the center of the coated lipid film surrounding by four fashion-like small O-rings. They are pressed down by a tweezer. These rubber rings should be cleaned by water and ethanol before. Then sucrose-water solution at 0.1 M concentration level is dropped inside the O-ring, which is sealed to form a chamber using a second vacuum-desiccated ITO glass. Alligator clips at the slide edge are used to fix them tightly. The excess sucrose solution should be wiped off using kimwipes. Then attach the ITO surface of two glass slides onto two aluminum bars using alligator clips.

(5) Electrowelling

These rubber-glass chambers need to be placed into an incubator at a miscibility transition temperature of ~60°C. A 1 V, 10 Hz sinusoidal wave is applied across the ITO electrodes. The button should be turned on before applying to the aluminum bars. Lipid bilayers will spontaneously vesiculate in 2 hours. In addition, a bottle 0.1 M glucose-water solution should be placed into the incubator to keep the same temperature with the sample.

(6) Harvesting

Take out the aluminum bars and the glucose solution from the incubator, and

draw 3 mL glucose-water solution into a glass tube for each sample. Remove all clips and

break the seal between two slides gently. GUVs are then suctioned up from the chamber

and dropped into the glucose-water solution for measurement. The density gradient of

sucrose and glucose concentrates GUVs [5.9].

5.4 RF Measurements

Glucose-water solutions at a 0.1 M concentration level with GUV particles are

first injected into the PDMS channel in Fig. 5.1. The sensor is tuned to a desired

sensitivity at each target frequency f_0, i.e., a desired $|S_{21}|_{min}$ level before a GUV passes

through the gap. Then a syringe pump is used to drive the GUV through the channel and

the slotline gap. The solutions are in a laminar flow and potential swirls of the fluid in the

channel contributing to possible tumbling motion of the GUV can be neglected. A

fluorescent microscope is used to observe the labeled GUV simultaneously. The

measurement setup is shown in Fig. 5.12. The GUV induced S-parameter changes are

recorded by the VNA. The S-parameter will return to the initial $|S_{21}|_{min}$ after the GUV

moves away from the slotline. Figure 5.13 shows two pairs (#1 and #2) of typical

measurement results for Group I at ~2.8 GHz. In each of the pairs, both the initial and

maximally changed (corresponding to the GUV right above the gap) $|S_{21}|$ are shown

together. The value of $|S_{21}|_{min}$ and its corresponding frequency changes with time, i.e.,

GUV position, are shown in Fig. 5.14. The figures show that our sensor is capable of

detecting a single GUV with good sensitivity. In Fig. 5.14, the maximum response occurs

when the GUV appears above the gap. Multiple frequency measurements can be achieved

to analyze GUV dielectric properties at different frequencies by adjusting phase shifters

and attenuators. The initial $|S_{21}|_{min}$s are adjusted between ~-100 dB and ~-105 dB. The

maximum responses are different for each set of GUV particles due to their different radii

and vertical positions in the channel.
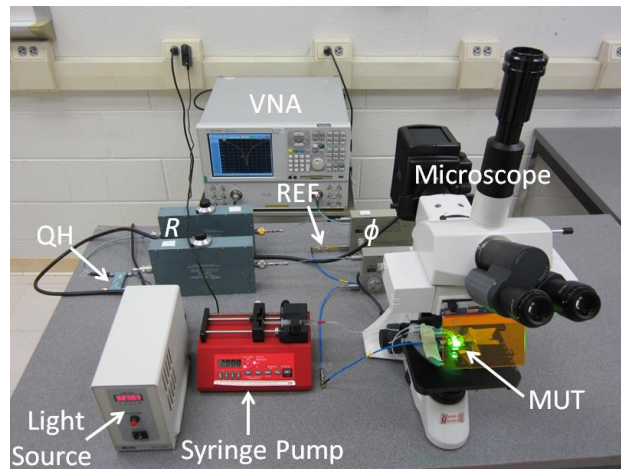
Fig. 5.12 Measurement setup for single GUVs.
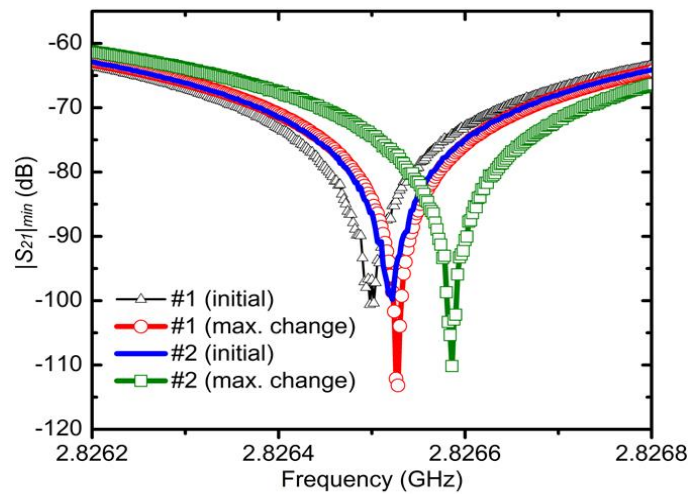
Fig. 5.13 Measured $|S_{21}|$ for Group *I* at ~2.8 GHz.
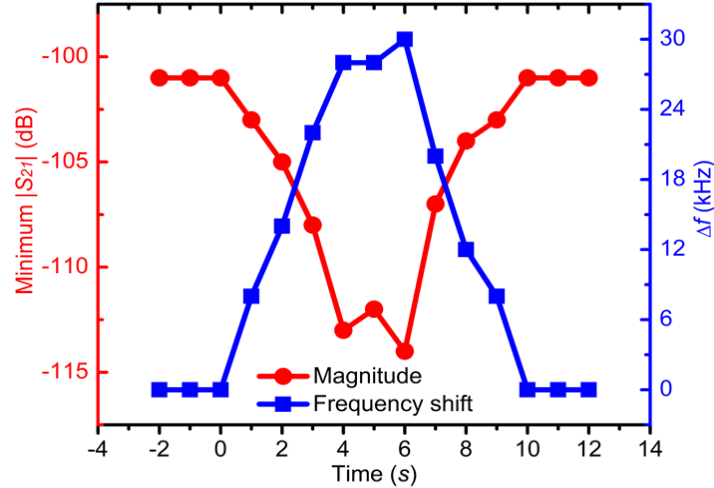
Fig. 5.14 Time-dependent $|S_{21}|_{min}$ and corresponding Δf (f_0: ~2.8 GHz) when single GUV passing through the slotline gap.

Figure 5.15 shows the extracted real and imaginary permittivity components of different GUV particles for each group at ~2 GHz, ~2.5 GHz, and ~2.8 GHz. Both models in the next section are used to obtain the permittivity values. The parameters for the calculations are listed in Table 5.1. Here, 5 μm and 6 μm are chosen as the GUV radius and vertical center position, respectively. The 5 μm average GUV radius value is estimated by comparing GUVs with the 50 μm wide PDMS channel observed under microscope. From microscope observations, it is also estimated that these GUVs are close to the slotline surface because the microscope is focused on the surface plane before the GUVs pass through the gap. Then the measured *S*-parameters are recorded when a GUV is observed to be close to the surface. The error bars indicate the distributions of five

repeated, but separate, measurements. In each group of the GUVs with the same compositions, the GUVs are synthesized and then measured on the same day. It shows that (*i*) the permittivity values of GUV particles are close to that of 0.1 M sucrose-water solution (ε'-$j\varepsilon''$=82.87-j7.83 (at 2 GHz), 82.43-j9.73 (at 2.5 GHz), 82.12-j10.85 (at 2.8 GHz) through [5.10]), which is reasonable and serves to verify the validity of the proposed extraction method; (*ii*) roughly the same results are obtained using the proposed Model #1 and #2. The differences between the models have been further reduced with the use of κ=0.67; (*iii*) the average ε' and ε'' also vary with frequencies, which may carry molecular dynamic process information. Further work is needed to understand the details.
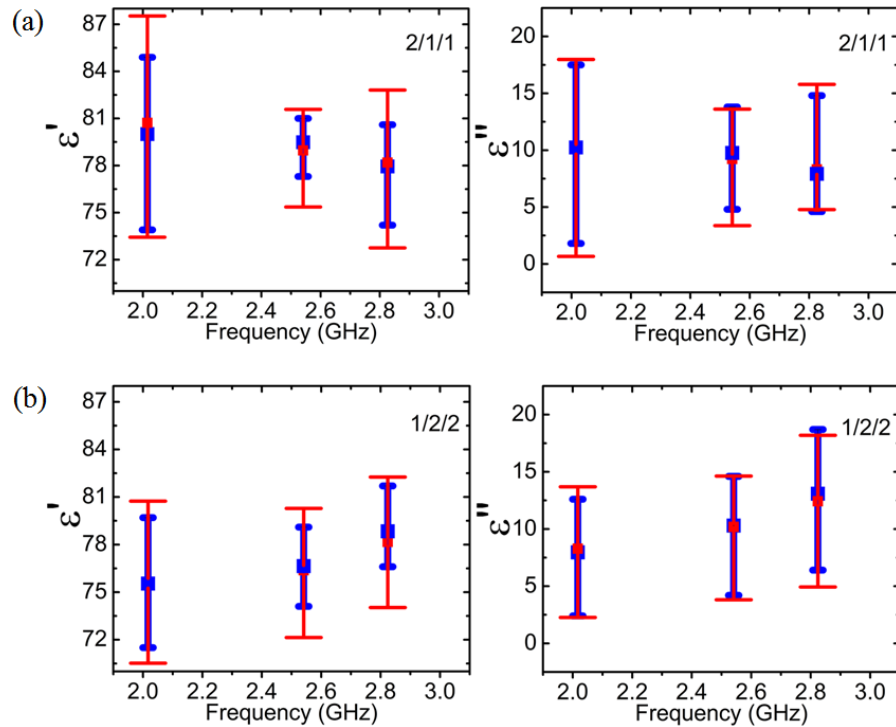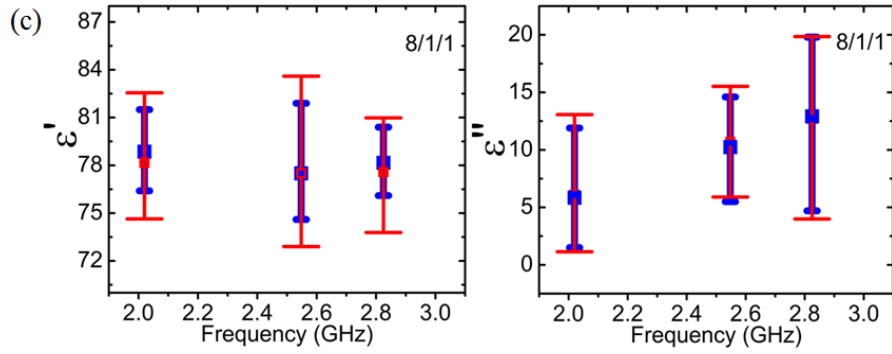
Fig. 5.15 The obtained real and imaginary permittivities ε' and ε'', of GUV particles for (a) Group *I* (POPC/SM/Chol: 2/1/1), (b) Group *II* (POPC/SM/Chol: 1/2/2), and (c) Group *III* (POPC/SM/Chol: 8/1/1) at different frequencies (blue bold lines and small caps are for Model #1; red thin lines and big caps are for Model #2).

TABLE 5.4
EXTRACTED PERMITTIVITIES AT DIFFERENT TIMES IN FIG. 5.15

Time (*s*)	ε_p (Model #2)
1	79.41-*j*16.16
2	79.41-*j*16.16
3	79.41-*j*16.16
4	79.42-*j*16.15
5	79.42-*j*16.12
6	79.43-*j*16.08
7	79.40-*j*16.14
8	79.41-*j*16.15
9	79.41-*j*16.16

The permittivity extraction and error range in Fig. 5.15 are from measuring five independent GUVs, which may have different diameters and vertical positions in the microfluidic channel. For each individual GUV particle, e.g., the one measured for Fig. 5.14, GUV size and vertical position are constant in the measurement process since the GUV only travels a very short distance. Using the measured *S*-parameters at each time

moment (i.e., longitudinal location), the obtained GUV permittivity with Model #2 is shown in Table 5.4. The almost identical GUV permittivity values, which are expected because GUV radius and vertical position do not induce relative error, further verify the validity of the model.

TABLE 5.5
EXTRACTED PERMITTIVITIES WHEN DIFFERENT RS, SCS, AND h_{bott}S ARE USED
(UNIT: μm FOR RS, SCS, AND h_{bott}S)

#	R	SC	h_{bott}	ε_p (Model #1)	ε_p (Model #2)
0	5	6	1	78.46-j14.46	79.43-j16.08
1	6	7	1	78.23-j14.56	79.10-j16.17
2	4	5	1	78.78-j15.93	79.91-j18.61
3	5	7	2	79.31-j15.89	80.89-j18.44
4	5	5.5	0.5	77.89-j15.68	77.30-j18.04
5	5	25	20	90.65-j25.05	93.10-j27.53
6	5	45	40	104.31-j44.58	106.91-j48.64
7	15	16	1	77.82-j14.37	78.71-j15.95
8	24	25	1	77.66-j14.19	78.53-j15.69

The high intensity electric field of the nanometer slotline strongly interacts with GUV particles so that significant changes of S_{21} in magnitude and phase can be observed. High sensitivity operations enable high measurement accuracies, which are critical for detecting and observing subtle biological and physical processes in cells and GUVs as well as for identifying potential markers. Nevertheless, a few factors, such as the uncertainties of GUV radius, shape, and vertical position (i.e., h_{bott} in Fig. 5.5), need to be addressed in the future. The estimated effects of these factors are listed in Table 5.5. The data show that the GUV vertical position has more significant effects than the uncertain radius on the interaction.

References

[5.1] D. M. Pozar, *Microwave Engineering*, 4th ed. New York: Wiley, 2012, pp. 50-52, 82.

[5.2] R. N. Simons, *Coplanar Waveguide Circuits, Components, and Systems*. New York: Wiley, 2012, pp. 331-332.

[5.3] J. Svačina, "Dispersion characteristics of multilayered slotlines–a simple approach," *IEEE Trans. Microwave Theory and Techn.*, vol. 47, no. 9, pp. 769-772, Sep. 1999.

[5.4] COMSOL Multiphysics. COMSOL, Inc., Burlington, MA, USA. [Online]. Available: http://www.comsol.com/

[5.5] H. Weingärtner, A. Knocks, S. Boresch, P. Hochtl, and O. Steinhauser, "Dielectric spectroscopy in aqueous solutions of oligosaccharides: experiment meets simulation," *J. Chem. Phys.*, vol. 115, no. 3, pp. 1463-1472, Jul. 2001.

[5.6] "Approximating Spheres with Boxes" from the Wolfram Demonstrations Project contributed by Jeremy Batterson. [Online]. Available: http://demonstrations.wolfram.com/ApproximatingSpheresWithBoxes/

[5.7] M. Angelova and D. S. Dimitrov, "A mechanism of liposome electroformation," *Progr. Colloid Poymr. Sci.*, vol. 76, pp. 59-67, 1988.

[5.8] I. V. Ionova, V. A. Livshits, and D. Marsh, "Phase diagram of ternary cholesterol/palmitoylsphingomyelin/palmitoyloleoyl-phosphatidylcholine mixtures: spin-label EPR study of lipid-raft formation," *Biophys. J.*, vol. 102, no. 8, pp. 1856-1865, Apr. 2012.

[5.9] P. J. Barrett, "Structural and cholesterol binding properties of the amyloid precursor protein C-terminal fragment C99 and the etiology of Alzheimer's disease," Ph.D. dissertation, Dept. Biochem., Vanderbilt Univ., USA, 2013, pp. 143.

[5.10] C. Reid, "Spectroscopic methods for medical diagnosis at terahertz wavelengths," Ph.D. dissertation, Dept. Medical Phys. Bioeng., Univ. College London, UK, 2009, pp. 128-129.

CHAPTER SIX

MICROWAVE SCANNING OF

GIANT UNILAMELLAR VESICLE MEMBRANE IN AQUEOUS SOLUTION

6.1 Principle of High Sensitivity of Split-ring Resonator

In Chapter V, a slotline-based sensing structure is used to detect single GUVs and analyze their dielectric properties, and the encouraging results have been obtained. However, to detect the GUV membrane heterogeneity formed by Phase L_o (35 Å thick) and Phase L_α (28 Å thick) [6.1]-[6.3], as shown in Fig. 6.1 [6.4], the sensitivity is required to be increased further.
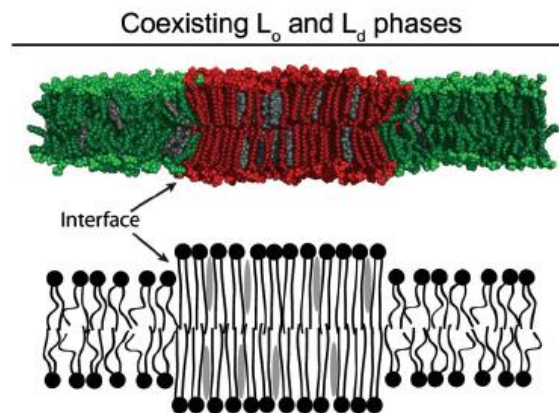
Fig. 6.1 Coexisting L_o and $L_d(L_\alpha)$ Phases demonstrating the GUV membrane heterogeneity [6.4]. Topper: molecular dynamics snapshot; lower: simplified molecular structural schematic. Green and disordered acyl chains: $L_d(L_\alpha)$; red and ordered acyl chains: L_o; grey and shadows: Chol.

The split-ring resonator (SRR) is a possible high-sensitive solution for the detection and analysis of GUV membrane, which was proposed by Pendry *et al* [6.5] in 1999 to obtained negative effective permeability in the microwave regime, and then was used as one component of composite "left hand" medium [6.6]. The SRR also demonstrates significant enhancement of the energy density of the electric field within the gap between the split rings at its resonant frequency (Figs. 12 and 17 in [6.5], re-printed as Fig. 6.2 in this dissertation) potentially for a strong microwave-MUT interaction.

To exhibit its performance on high sensitivity, a PCB-based SRR is fabricated on Duroid 5870 laminate [6.7], is shown in Fig. 6.3. The ring and ML are separated by a 500 μm gap, and the split on the ring is also created using the same dimension. Only 500 μm, rather than a smaller one, is gaped since the minimum size is limited for our milling machine shown in Fig. 2.4. The HFSS simulations demonstrate that the designed SRR has a narrow $|S_{21}|$ stop band and a narrow $|S_{11}|$ pass band around the first resonant frequency 3.05 GHz, as shown in Fig. 6.4.

(a)   (b)
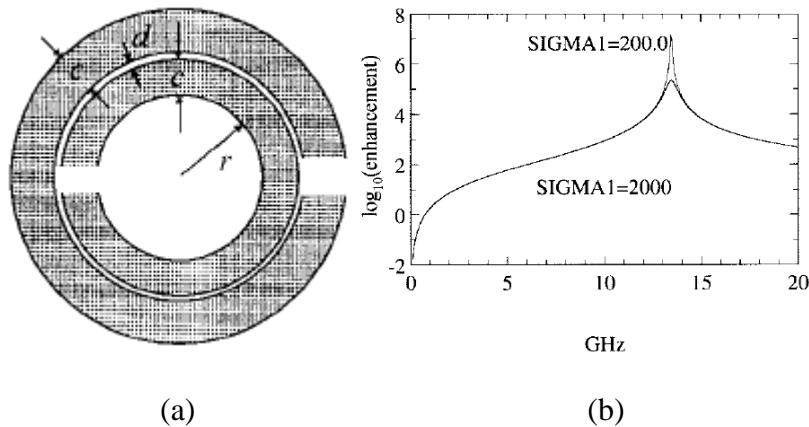
Fig. 6.2 (a) Plan view of the proposed SRR in [6.5] (b) Enhancement of the energy density of the electric field within the gap between the split rings for two different values of the resistivity of the metal sheet [6.5].
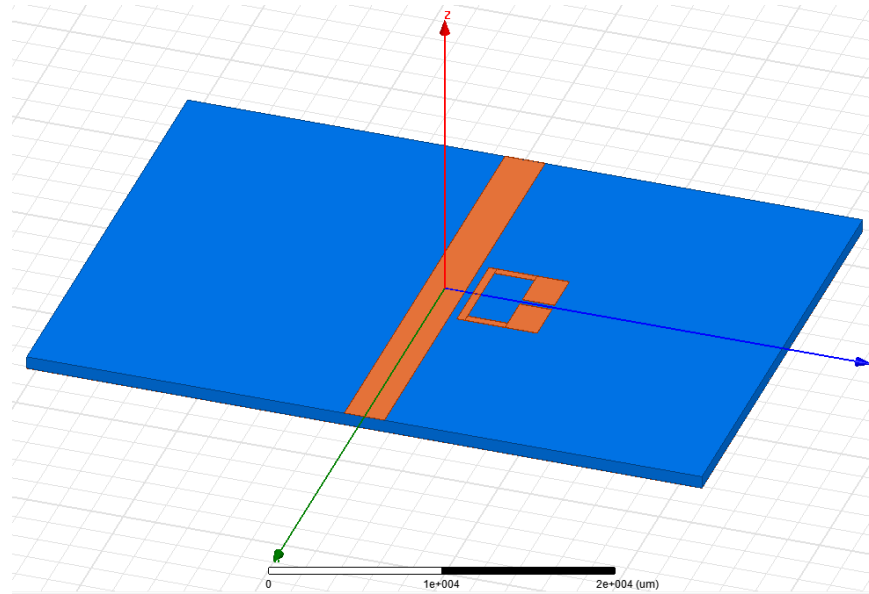
Fig. 6.3 Schematic of a PCB-based SRR in HFSS.

(a)   (b)
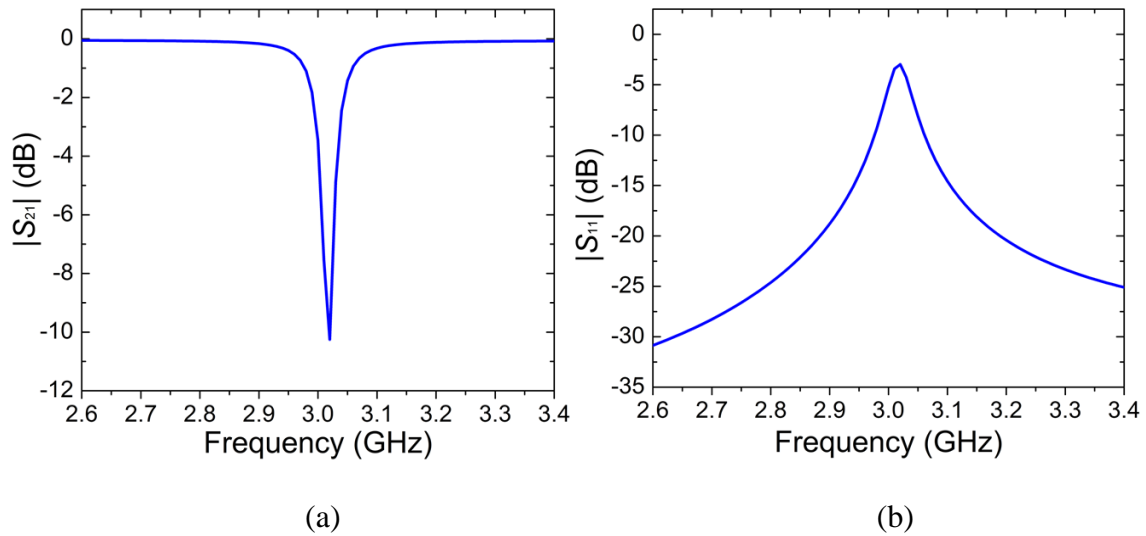
Fig. 6.4 Simulated (a) $|S_{21}|$ and (b) $|S_{11}|$ of the SRR in Fig. 6.3.

For the regular ML, the electric field always concentrates the edge of the line [6.8] for sensing in a wide range. After adding a ring aside, however, the electric field of the SRR concentrates only in the narrow split around the resonant frequency from the simulation in Fig. 6.5. The concentrated electric field in the split means that a part of energy is stored into the ring from the total microwave energy transmitting along the ML. Since there is no enough big inductance to store magnetic field, most energy coming from the ML has to be stored into the capacitor formed by the split. From Fig. 6.5, the percentage of the coupled energy from the ML into the ring can be calculated, as shown in Fig. 6.6. At the resonant frequency, ~40% energy is coupled. But only a part of the energy is stored and the other has to be dissipated by the ring resistor R. The quality factor Q is defined by [6.9]

$$Q = \omega \frac{\text{average energy stored}}{\text{energy loss/second}} = \omega \frac{W_e}{P_{loss}}$$

(6.1)

where W_e is the average electric energy stored in the capacitor, and P_{loss} is the power dissipated by the resistor R.

The electric field concentrating around the split is verified to be more sensitive than that around the gap between ML and ring, shown by Fig. 6.7. In the measurement, a 0.5 mm $\times$ 0.5 mm $\times$ 0.5 mm PDMS is loaded on the split and the gap, respectively, for a comparison. The result for air-load only (no PDMS) is also drawn together. From the figure, the PDMS placed at the split shifts the resonant frequency towards left ~75 MHz, and S_{21} in magnitude changes ~0.55. As another comparison, for a 4 mm $\times$ 2.5 mm $\times$ 2.0 mm PDMS, the fundamental resonant frequency of the two-stage RF interferometer with

the significantly improved sensitivity [6.10] only shifts ~3.2 MHz, and S_{21} in magnitude changes ~0.0012, re-printed as Fig. 6.8.
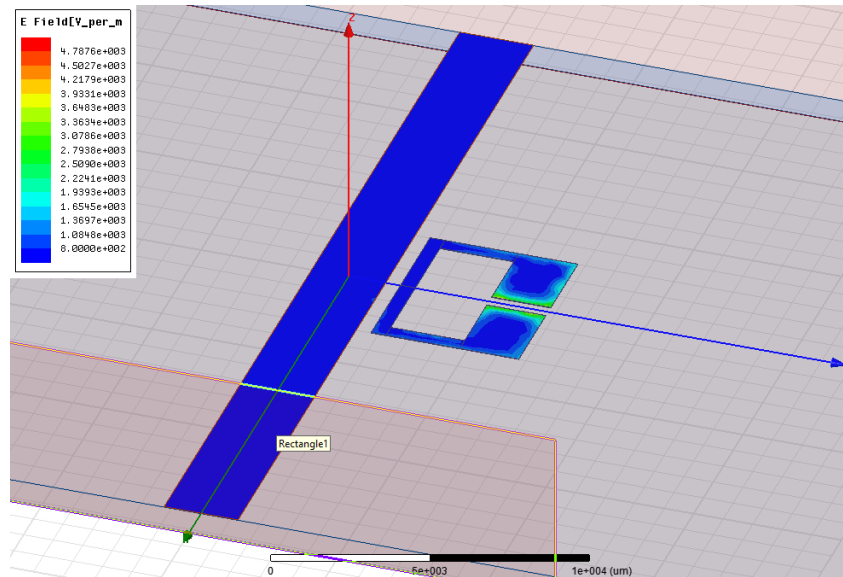
(a)
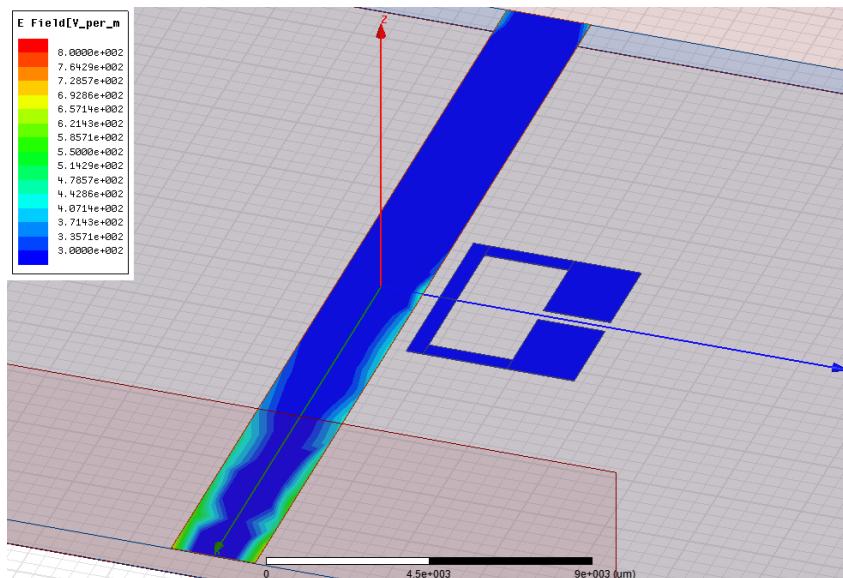
(b)

Fig. 6.5 Electric field distributions simulated (a) at 3 GHz and (b) at 2 GHz for the resonator in Fig. 6.3.
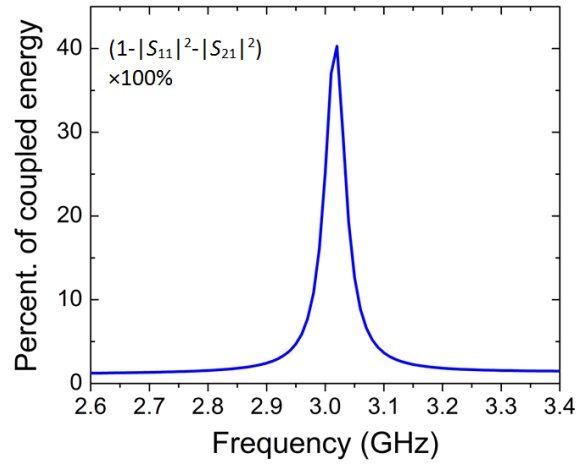
Fig. 6.6 Percentage of the coupled energy from the total microwave energy on the ML.
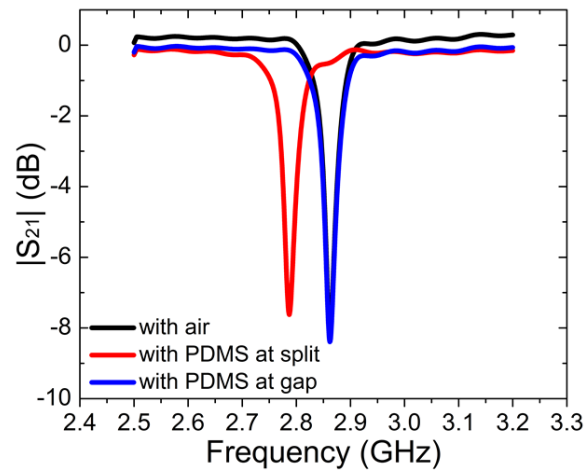
Fig. 6.7 Different $|S_{21}|$ responses around the resonant frequency without and with a PDMS at the split of ring and the gap between ML and ring.
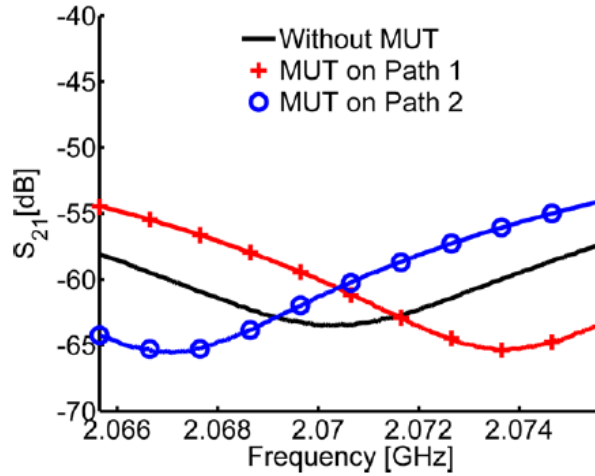
Fig. 6.8 Typical measured results of the two-stage interferometer using the PDMS as MUT [6.10].

We can see that the resonator, which can concentrate electric field within a limited region, causes that, without and with MUT there, the transmission of microwave is changed hugely. As a microwave component, SRRs have such properties: (*i*) coupling at specific frequencies (via 4 ports coupled lines, blue box in Fig. 6.9(a)) into a ring-shape structure for multiple-reflections; (*ii*) concentrate electric field via a narrow split (modeled by a π-network with three capacitors [6.11], green box in Fig. 6.9(a)). The design in Fig. 6.9(a) will be applied to a micromachined chip for the detection of GUV membrane later. For (*i*), the electromagnetic wave at a specific frequency undergoes multiple internal reflections along the ring and gives rise to a standing wave with significantly increased group delay; for (*ii*), a lot of microwave energy is stored into the split, of which capacitance can be significantly affected by slight permittivity change in the split caused by MUT. Figure 6.9(b) is the simulated $|S_{21}|$ (without considering a

91

solution in the capacitance) of the SRR in Fig. 6.9(a) using Advanced Design System (ADS) [6.12], displaying four resonant frequencies, i.e., 1st odd mode, 1st even mode, 2nd odd mode, and 2nd even mode, from 1 GHz to 12 GHz. The used structural dimension can be also modified to obtain resonances at other frequency points, e.g, to decrease the length of the coupled line to obtain higher resonant frequencies. From the detailed mathematic analysis in Section 6.4, only odd mode is related to the role of the property (*ii*). Great group delays are found at these resonant frequencies, as shown in Fig. 6.9(c), indicating that the standing wave formed by multi-reflections is able to interact more time with MUT. The schematic of the multi-reflections in SRR will be shown in Fig. 6.41 in Section 6.4. The schematic in Fig. 6.9(a) will be micromachined for the GUV detection in Section 6.2 and 6.3.

(a)

(b)

(c)
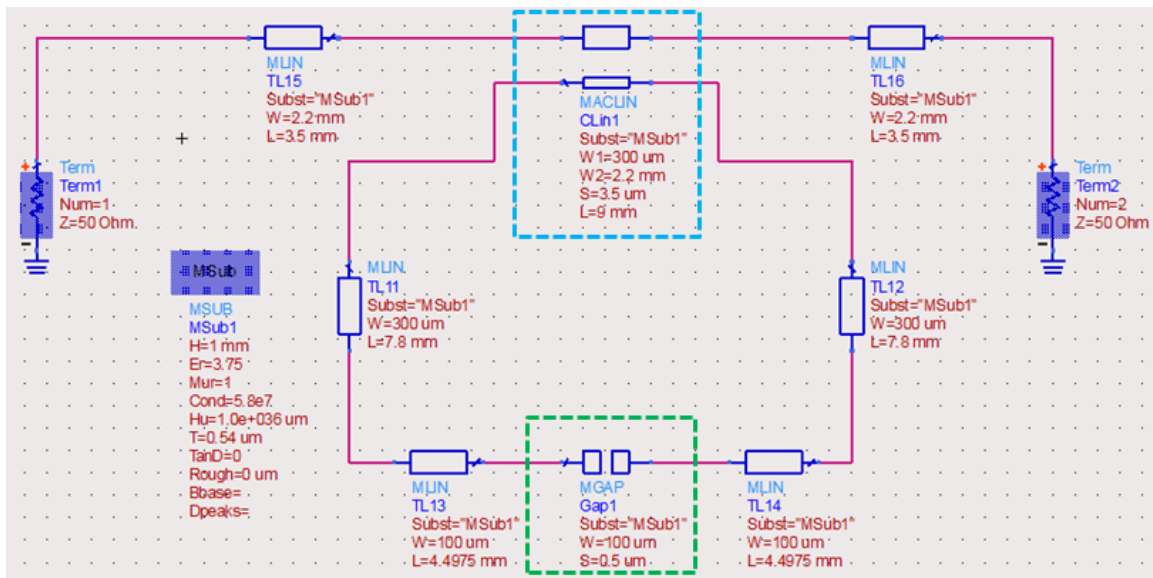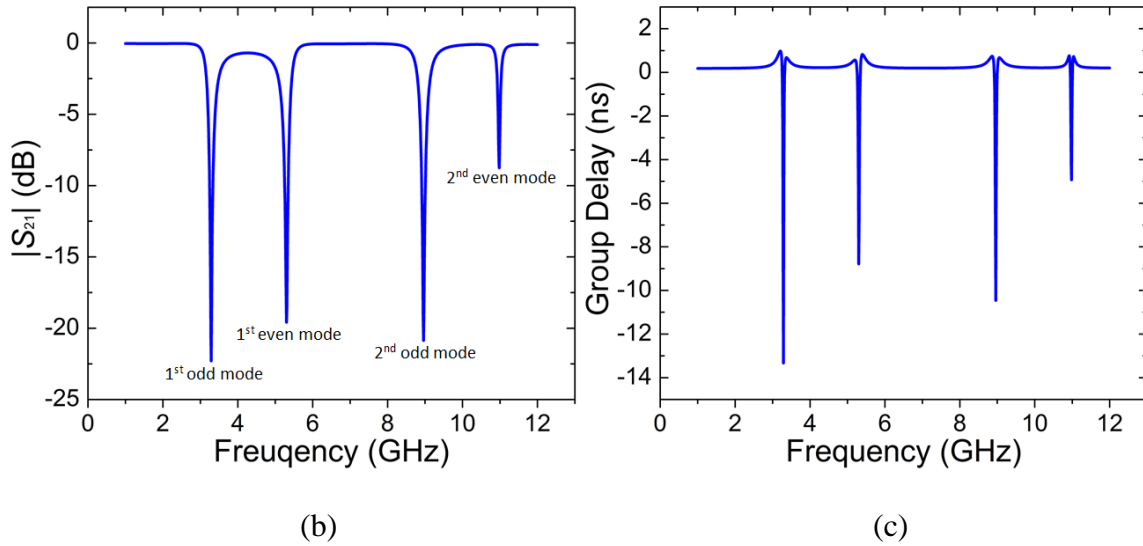
Fig. 6.9 (a) Schematic of the equivalent circuit of a SRR. Simulated (b) $|S_{21}|$ and (c) group delay of the SRR in (a) by ADS.

For (*i*), the similar idea has been also used in some optical resonators with ultra-high sensitivity, e.g., the coupled microtoroid cavity-nanoparticle system [6.13], as shown in Fig. 6.10. Here the fibre taper couples light into and out of the microtoroid in *a*, and a part of light at specific frequency is coupled into the microtoroid. Then two whispering-gallery-modes (WGMs) rise with opposite propagation directions in *b*, that is, clockwise and counter-clockwise modes. Thereafter, the interaction with MUT is enhanced by the standing wave mode (SWM). A potassium chloride (KCL) particle with a diameter of 80 μm can be detected, as shown in Fig. 6.11.
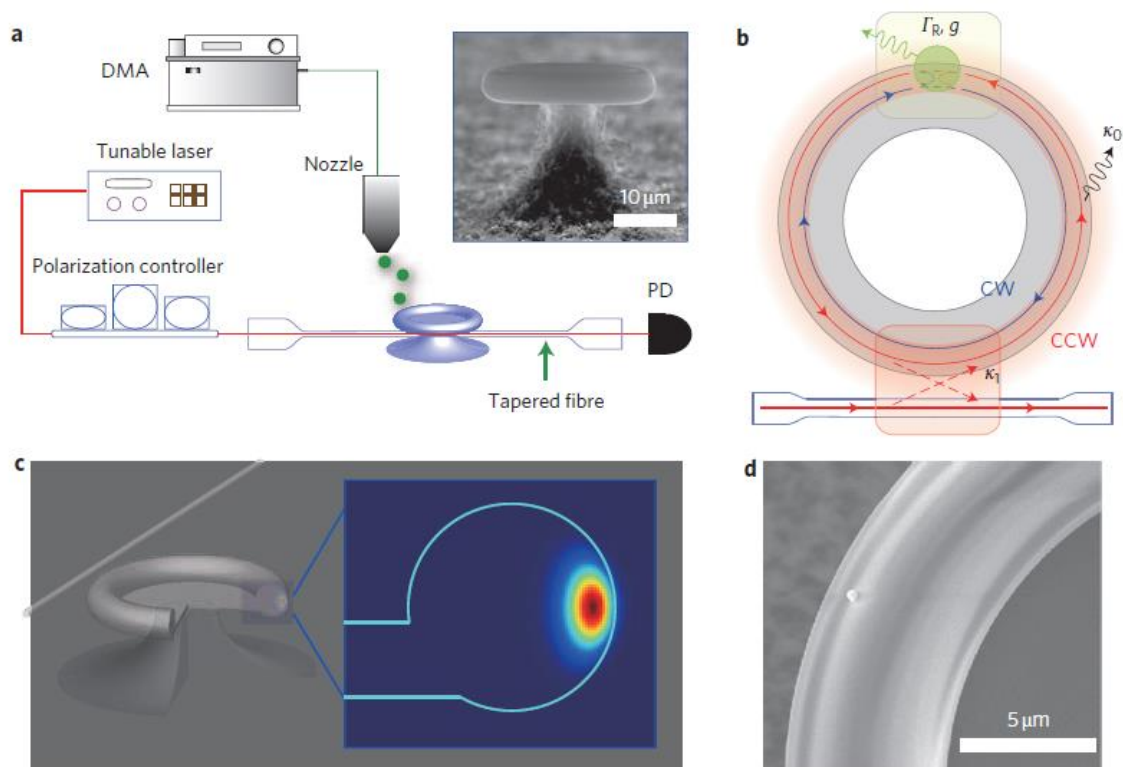
Fig. 6.10 Experimental set-up and coupled microtoroid cavity-nanoparticle system [6.13].
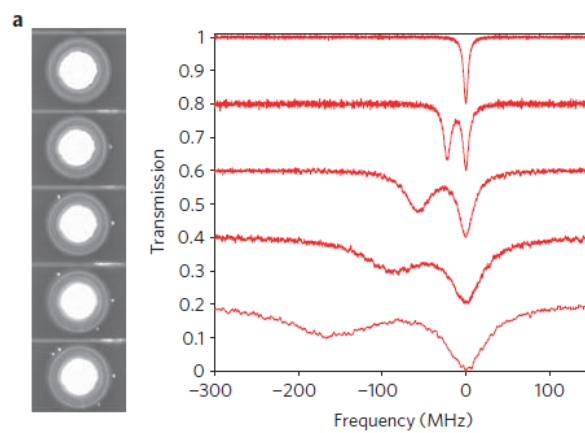
Fig. 6.11 Transmission spectra and the amount of splitting versus number of deposited

KCL particles with a diameter of 80 nm [6.13].

For (*ii*), the nanoscale-fabricated gaped metal for confining electric field has been also reported for the detection of nanoparticles [6.14], e.g., polystyrene with different diameters (51 nm, 75 nm and 117 nm), HIV (130 nm), and Hepatitis C (55 nm), as shown in Fig. 6.12. Here, nanoparticles in saline suspension flow in the direction of the arrows, and changes in the electrical potential of the fluid adjacent to the nanoconstriction built by a 250 nm $\times$250 nm $\times$290 nm gap are detected by the lithographed sensing electrode.
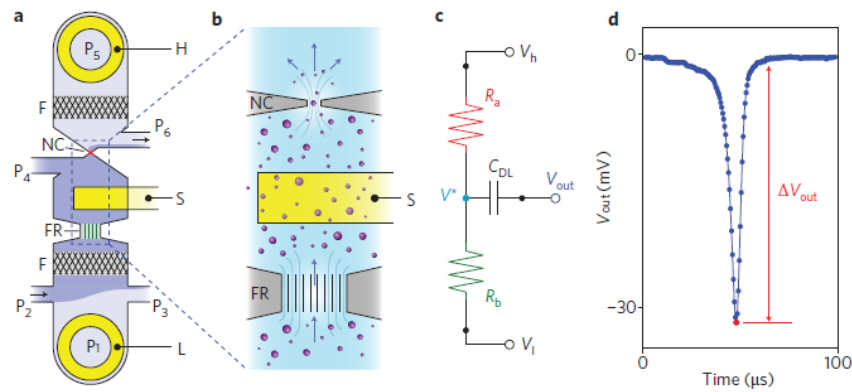
Fig. 6.12 Device schematics and detector response. (a) overall chip layout; (b) detail of boxed area in (a); (c) electrical equivalent circuit; (d) output voltage V_{out} as a function of time responded by a 117 nm polystyrene in diameter [6.14].

In a summary, the design in Fig. 6.9(a) collects two aspects of advantages in (*i*) multiple-reflections and (*ii*) confined electric field for the expectation of ultra-high sensitivity to detect GUV membrane.

Some people might have a question: if we can only build a split on a metal line, then apply a DC voltage to the split and measure the capacitance change between without

a GUV and with a GUV? This design shown in Fig. 6.13 looks simpler than the SRR.

However, even if a short DC pulse (μs to ms, 10^3 to 10^4 V/cm) has lead to the

electroporation on lipid membrane [6.15], even the cell death is caused [6.16]. For the

exhibited frequency range over 1 GHz in Fig. 6.9(b) and the following measurements in

Section 6.3, the time period of sinusoidal wave with the similar electric field intensity in

Fig. 6.15(a) is lower than 1 ns. So the proposed microwave technique is non-destructive.

Moreover, the used frequency range does not cause the deformation of GUV [6.17].

Another possible proposal is to design a ML like that in Fig. 6.13, which can operate at a

microwave frequency and concentrate electric field in the middle split. But the multi-

reflections cannot be achieved under this situation. According to a quick ADS schematic

simulation, for a same capacitance change from 30 fF to 31 fF, the $|S_{21}|$ change of the

SRR in Fig. 9(a) at 1st odd-mode resonant frequency is ~100 times larger than that

obtained by a well-matched middle-gaped ML at the same frequency.
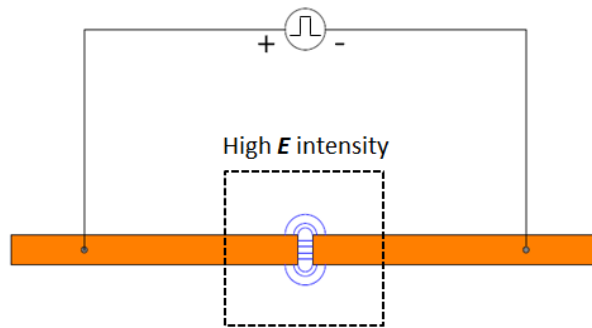
Fig. 6.13 Split in the middle of a metal line for DC measurement.

6.2 Micromachined Split-ring Resonator and Microfluidic Channel

To detect a single GUV membrane, the sensing area, i.e., the split gap, needs to be downsized to several microns even smaller to concentrate electric field there. The presented structure with a section of microfluidic channel (green color) is shown in Fig. 6.14(a), where the metal layer Ti/Cu/Ti: 20 nm / 500 nm / 20 nm is deposited onto the fused silica substrate with a thickness of 1 mm. The process is the same as that in Section 3.5. The split and the gap between ML and ring are reduced to 5 μm on the mask. After the lift-off process, they are ~3.5 μm measured by a microscope, but a narrower gap is more positive to enhance the coupling. Then Tungsten (W) will be deposited into the ~3.5 μm ring split to form a narrower 500 nm $\times 100$ μm. The HFSS simulation in Fig. 6.14(b) indicates that 1st and 2nd odd modes are at 2.70 GHz and 7.75 GHz, respectively. Because of the adoption of different solving methods, i.e., FEM for HFSS, analytical formula for ADS, the results in Fig. 6.14(b) are different from those in Fig. 6.9(b). The energy coupling from the ML is also calculated from the simulated $|S_{21}|$ and $|S_{11}|$, and shown in Fig. 6.14(c). Although the energy is also coupled from the ML under the even mode, i.e., 5.07 GHz and 11.08 GHz, the electric field streamline will start from the edge of the split and terminate at the bottom metal. For this situation, only limited streamline can penetrate MUT at the split, so it is not suitable for high sensitive measurement. The detailed analysis of odd and even modes will be stated in Section 6.4. Figure 6.15(a) shows the electric field distribution for 12.7 dBm input power (used in the following measurements), where we can see the electric field strongly concentrates around the split, i.e., 7.99×10^6 V/m and is at least 10-times larger than that at other most area. Besides, the

field in the gap is in parallel with GUV membrane and perpendicular to the field on the electrode surfaces. The field intensity variations in Fig. 15(b) show that (*i*) the microwave field is much stronger in and near the split gap than elsewhere; (*ii*) the top GUV membrane does not produce much signal due to very weak microwave fields; (*iii*) the vertical distributions of field intensity is different for 2.70 GHz (first odd mode) and 7.75 GHz (second odd mode). The only ~-6 dB minimum $|S_{21}|$ looks not so high compared to many published resonators [6.18], [6.19]. However, there is only one main reactance component formed by a nanoscale split in the proposed SRR, which stores the microwave energy. The lower $|S_{21}|$ in other resonators are always produced by a couple of inductors and capacitors. So that is a sum.
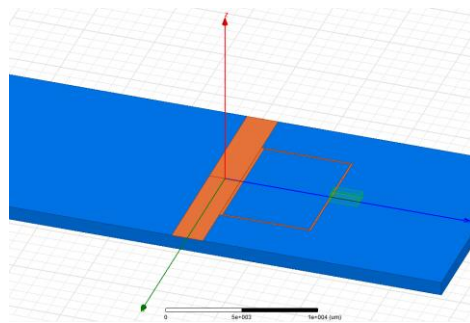
(a)
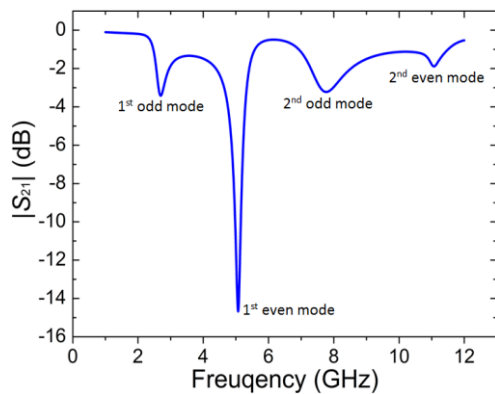
(b)
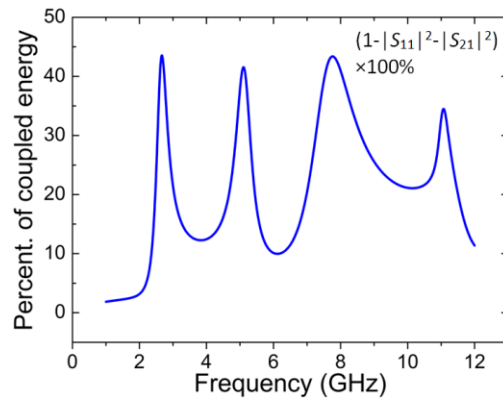
(c)

Fig. 6.14 (a) Schematic of the micromachined SRR with partial microfluidic channel in HFSS. Simulated (b) $|S_{21}|$ by HFSS and calculated (c) coupled energy from the total microwave energy.

(a)   (b)
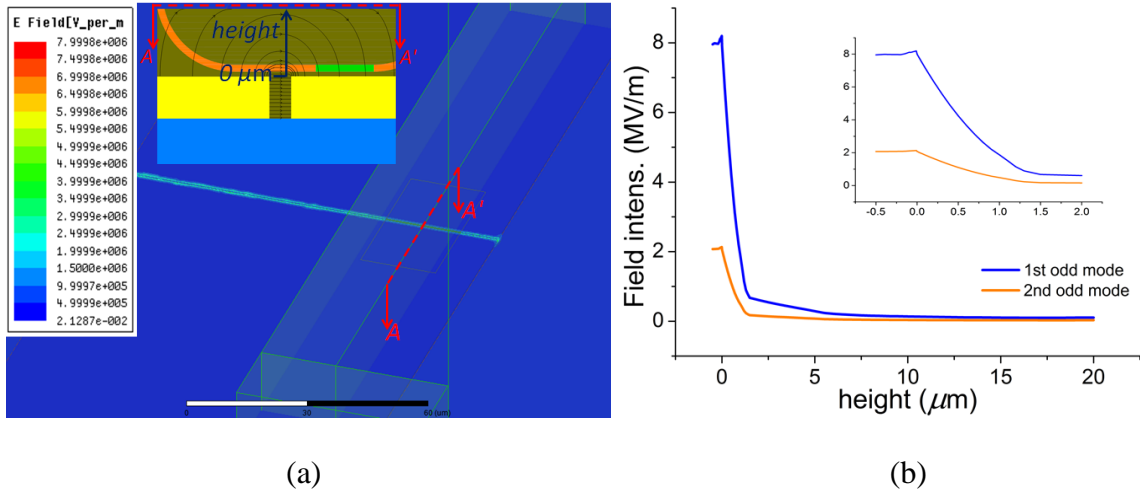
Fig. 6.15 Simulated (a) electric field distribution around the split gap at the resonant frequency of the first odd mode and (b) field intensity versus height using the top surface of metal layer set as origin at the first two odd modes, i.e., 2.70 GHz and 7.75 GHz.

As commented in Chapter I, the introducing of lossy material, e.g., DI water, can significantly decrease the quality factor of a resonator. To avoid this issue as far as possible, the PDMS mold for microfluidic channel transporting GUVs is designed to a combination of two layers with different thicknesses, as shown in Fig. 6.16. Figure 6.17 is a camera shot after the PDMS channel is assembled onto the sensing area, showing GUVs passed through the 18.8 μm-thick (measured by a profilometer) section under a

fluorescent microscope. We can see that there is only a short micro-channel with an 18.8 μm $\times 25$ μm cross section is attached to the metal layer.
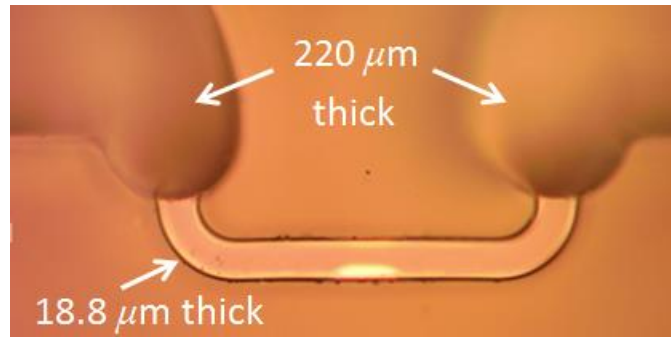
Fig. 6.16 Microscopy of the proposed SU-8 mold for PDMS channel.
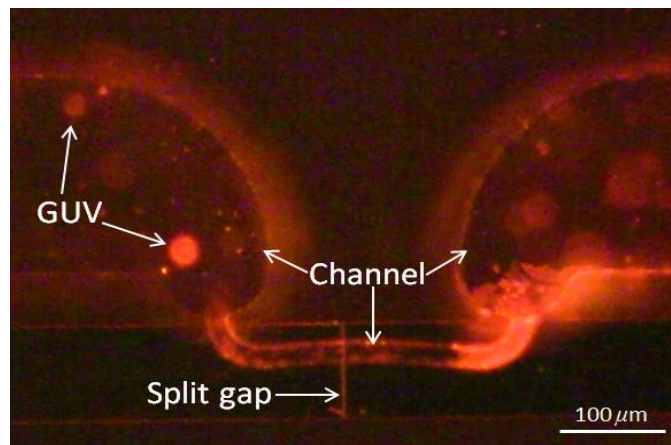
Fig. 6.17 PDMS channel assembled onto the sensing area, i.e., the split, transporting GUVs.

The following are fabrication steps and used recipes for the SU-8 mold in Fig. 6.16:

(1) Substrate preparation

Clean fused silica wafers by piranha first, then place them onto a hotplate with 150°C and 15 minutes for dehydration.

(2) Thin SU-8 layer coating

The 18.8 μm-in-thickness layer should be created prior to the 220 μm thick layer. Once the order is reversed, the distance between the optical mask and the thin SU-8 layer will be 220 μm when the wafer is ready to be exposed. So it is not contact lithography for the thin layer. A too long distance means that the severe diffraction will not make sure the desired feature size. For the thin layer, SU-8 GM 1060 [6.20] is coated by the recipe in Table 6.1. Then leave the wafer onto a hotplate at 100°C for 5 minutes for soft-baking. The exposure time 26.3 s (dose: 158 mJ/cm^2) is used for a soda lime mask under the UV intensity 6 mW/cm^2. Next, use 100°C for 5 minutes for post-baking. Then the wafer is immersed into SU-8 developer [6.21] for 4 minutes and needs to be shaken continuously. After development, the wafer should be rinsed in IPA solvent for several seconds.

TABLE 6.1
SPINNING RECIPE FOR SU-8 GM 1060

Step #	RPM	RPM/s	Time (s)
1	500	100	10
2	1000	100	10
3	1000	100	45
4	0	100	10

(3) Thick SU-8 layer coating

The thick SU-8 layer is coated using SU-8 2075 [6.22]. Table 6.2 is the spinning recipe. For soft-baking, use 100°C for 60 minutes. The exposure time 101.7s (dose: 385 mJ/cm^2) is used for a soda lime mask under UV intensity 5.68 mW/cm^2. The

development time 17 minutes in [6.22] are not sufficient to remove residual photoresist between some narrow gaps. More time, e.g. more 30 minutes, for developer shaking rinsing is required. Figure 6.18 compares the surface profiles after 17 minutes and 47 minutes rinsing times are used, respectively. Similarly, the wafer should be also rinsed in IPA solvent after development. The SRR in Fig. 6.14 and the mold in Fig. 6.16 are fabricated in Electrical and Computer Engineering Cleanroom at Clemson University [6.23].

TABLE 6.2
SPINNING RECIPE FOR SU-8 2075

Step #	RPM	RPM/s	Time (s)
1	500	100	10
2	1000	300	30
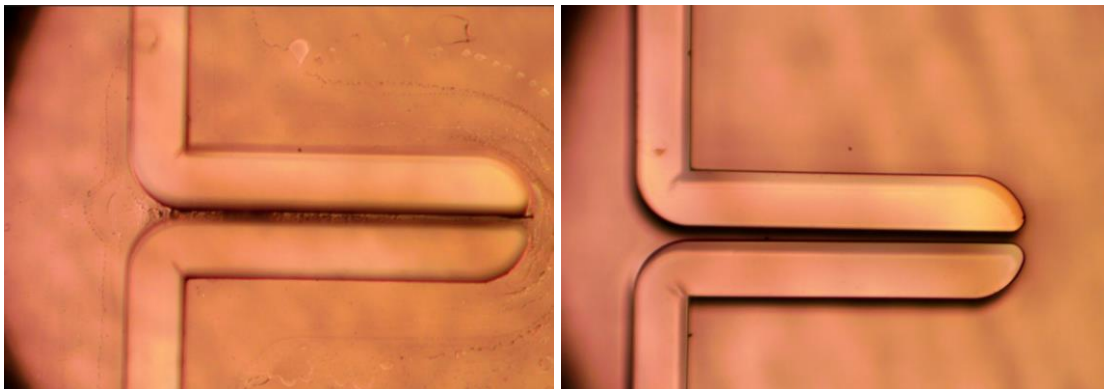
| (a) | (b) |

Fig. 6.18 Surface profiles after (a) 17 minutes and (b) 47 minutes developer rinsing time.

6.3 Time-domain Measurement of Single GUV Membranes

In the measurement, the micromachined SRR is loaded on a brass to eliminate the mechanical noise, as shown in Fig. 6.19. Two silicon tubings are assembled for solution

flow-in and -out. The measured $|S_{21}|$ and calculated percentage of the stored energy from the total microwave energy are also shown in Fig. 6.20 (a) and (b), respectively. During the measurement, the channel is filled with 0.1 M glucose-water solution, which is also used as the aqueous carrier medium of GUVs in the following. In Fig. 6.20(a), at the first and second odd mode resonant frequencies, locating at 2.7 GHz and 7.9 GHz, respectively, the time-domain detection of GUV membrane will be performed. The measured $|S_{21}|$ are -4.51 dB and -3.44 dB, and the percentages of the coupled energy are 45.74% and 45.53%, respectively.
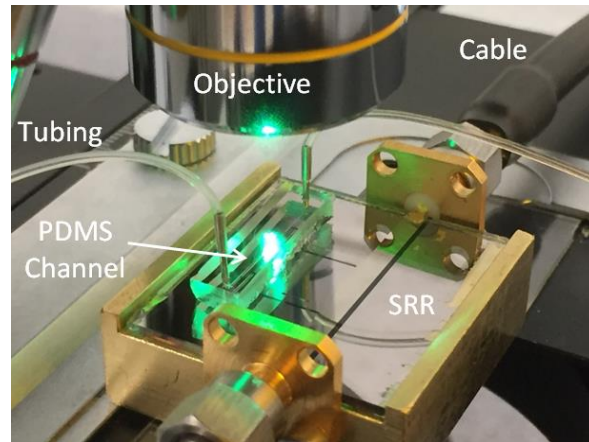
Fig. 6.19 Measurement setup for the detection of GUV membrane.

(a)   (b)
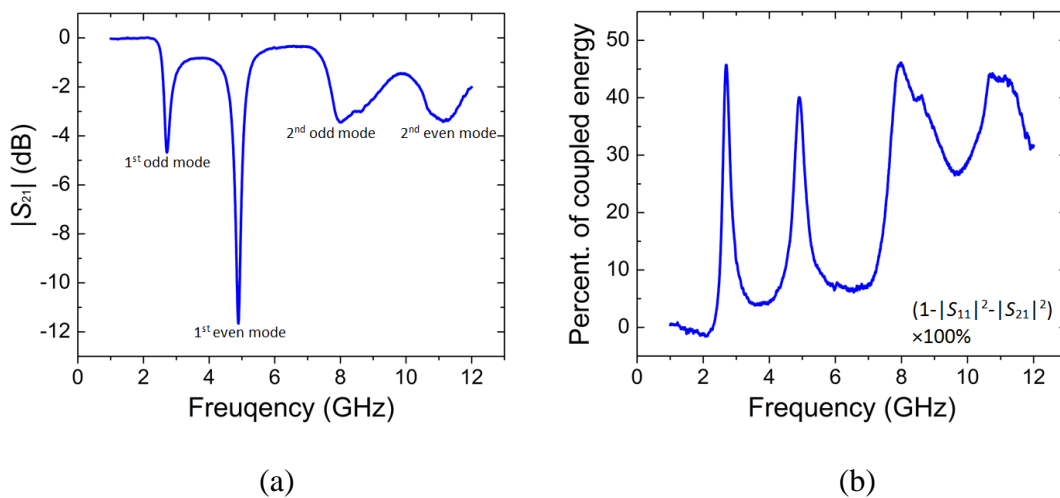
Fig. 6.20 (a) Measured $|S_{21}|$ and (b) percentage of the coupled energy from the total microwave energy from 1 GHz to 12 GHz for the SRR loaded with 0.1 M glucose-water solution.

To obtain signal response only caused by the membrane itself, the dielectric difference of different liquids inside and outside a GUV requires to be excluded. As a result, both the carrier medium and the solution in the GUV have to originate from the 0.1 M glucose-water solution in a same bottle. Other procedures for GUV synthesis are the same as those in Section 5.3. It is found that when the molar fraction 10/65/25 of POPC/SM/Chol is used during GUV synthesis, a lot of GUVs with significantly identifiable L_o and L_α phases rise, which can be clearly separated by two fluorescent labels, DioC18 and Rho-PE. So this recipe is used in the following experiment. The corresponding lipid amount is calculated, as shown in Table 6.3. It is noting that labels are reported to affect microwave membrane structures [6.24], [6.25]. But, it is expected that Rho-PE and DioC18 do not significantly affect measurement results since they only account for ~1% of membrane lipid molecules.

TABLE 6.3
CALCULATION OF LIPID AMOUNT

Lipid	Mixtures Mol wt (g/mol)	Mol %	Vol of each (μL)
16:0-18:1 POPC	760.1	10	4.23
16:0 SM	703	65	25.4
Chol	386.66	25	5.37

Using the measurement setup in Fig. 6.19, the solution with GUVs is transported through the silicone tubes into and out from the microfluidic channel by a syringe pump. The rate of 2 μL/min is selected for a relatively low flow during the measurement. Since the intensive electric field concentrates around the split, the bottom surface of a GUV passing through the channel is interacted effectively. When the bottom surface touches the split on the metal layer, the largest signal readout will be obtained. Two cables shown in Fig. 6.19 are connected to Agilent's VNA N5230A for *S*-parameter measurement. To conveniently record data, the VNA is connected to a laptop and controlled by Labview [6.26] using a graphic programming interface. The graphic codes are shown in Fig. 6.21. For the settings of the VNA, the intermediate frequency bandwidth (IFBW) 1 kHz is selected to obtain a good compromise between fast measurement and low noise, and the input power 12.7 dBm is used, which is the maximum value without an un-leveled prompt in this VNA. From the feedback of the VNA, the measurement time per point is 1.01 m*s*, so one-time 3000-points scanning costs 3.03 *s*. It is noting that Labview cannot read the calibrated *S*-parameters from the VNA. So a further processing on the uncalibrated data transferred to the laptop is required. In fact, the VNA also does the same processing in its interior [6.27]. The detailed process is introduced in Appendix A. All data existing in the main body of this dissertation have been calibrated.

Before starting detecting GUV membrane heterogeneity, some additional experiments are required to verify that the proposed sensor has sufficient sensitivity to distinguish L_o and L_α phases. In other words, the SM-rich domain (L_o) and the POPC-rich domain (L_α) should have a significant difference at permittivity. Therefore, two different

types of GUVs synthesized only with SM or POPC, respectively, are measured prior to the heterogeneity detection.
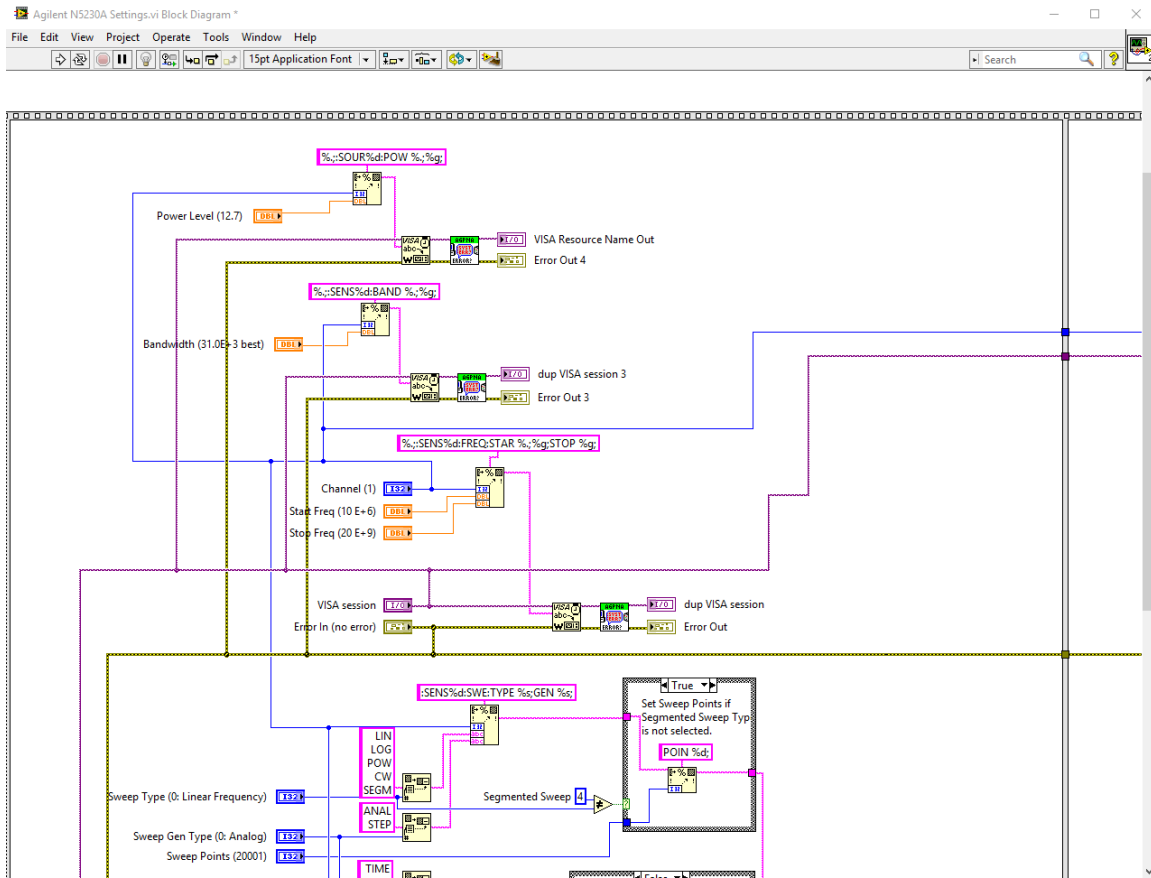
Fig. 6.21 Labview graphic codes for the control of the VNA and the data-recording.

Unfortunately, the size distribution of GUVs ranges widely. It is observed that too large GUVs will fold even rupture when they pass through the channel, while too small ones will pass through the channel without any shape reconstruction. These phenomena are consistent with the reported in [6.28]. For a too small GUV, the measurement result is subject to the uncertain vertical position. Even, there will be not any readout for a GUV

far away from the split region. For the GUV with a size between them, A. Yamada *et al*'s confocal microscopy images [6.28] indicate that the top and bottom surfaces are fattened against the microchannel walls, as shown in Fig. 6.22. But in the images, the GUV is not confined at *y*-direction, unlike the proposed 18.8 μm $\times 25$ μm PDMS microfluidic channel shown in Fig. 6.17, where *y*-direction is also confined like *z*-direction. Assuming that *x–y* plane profile in the proposed work is similar to the *x–z* plane in Fig. 6.22, it is reasonable to believe that an enough fitting GUV can almost completely fill in the whole 18.8 μm $\times 25$ μm cross section of the channel due to *y*-direction restriction. Thus, only GUVs with a diameter of ~25 μm at least are considered for the measurement. Such GUVs can produce enough big signal response and the almost completely filling is convenient to quantify the permittivity of the GUV membrane, which will be discussed further in Section 6.4.

To analyze the possible profile of a ~25 μm GUV in the proposed 18.8 μm $\times 25$ μm cross section, it is assumed that there is not a *y*-direction wall first, so that eqs. (2) and (3) in [6.28] apply to the *y–z* plane. Re-scaling R_0 versus Δx in Fig. 7 in [6.28] with an appropriate ratio, a GUV with 25 μm in diameter in the channel is shaped as Fig. 6.23(a), where the shape constants *b* and *c* are equal to 2.17 and 2. However, two walls on the left and right sides confine the horizontal length to be only 25 μm. The extrusion from the walls will make the GUV flatten further, as shown in Fig 6.25(b). Since the surface area of a squeezed GUV changes little (<2% in Fig. 7 [6.28]), it is reasonable to assume that the perimeter in Fig. 6.25 (a) and (b) keep consistent. The following eq. (6.2) will be used to calculate Δ_1 and Δ_2 in microns.

$$\Delta_1 + \Delta_2 + \sqrt{(7-\Delta_2)^2 + (9.4-\Delta_1)^2} = 9.4\pi \qquad (6.2)$$

As an estimation, let $\Delta_1 = \Delta_2$, then one can solve it is 4.9 μm. In other words, for the GUV

with a diameter of no smaller than 25 μm, the flatten area at the bottom surface is 20.8

μm at least. In eq. (6.3), the curve is treated approximately as a straight line to avoid the

complete elliptic integral of the second kind.
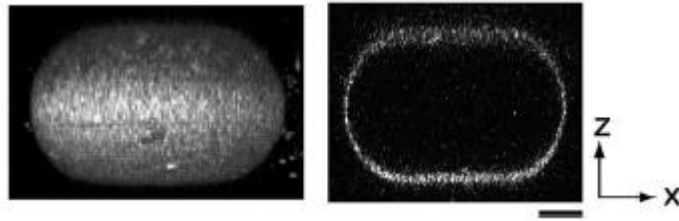
Fig. 6.22 Left: three dimensional reconstruction of the confocal microscopy image when

the GUV is confined in a channel; right: cross-section of the left image in an x–z plane.

Bar, 10 μm. [6.28]

Although we have the above estimation, the accurate dimension for each

individual GUV is still uncertain, i.e., the flatten area ranges from 20.8 μm to 25 μm but

more or less for different GUVs. To estimate the average signal response (S_{21}) for these

GUVs, 10-times independent and repeated experiments for each group of GUVs

discussed in the previous paragraph are performed to establish their representative sample

space. Then, the random variable, S_{21} change between without and with a GUV, is

modeled by a normal distribution, i.e., $\Delta S_{21} \sim N(\mu, \sigma)$. Here, the use of normal

distribution only produces the most conservative prediction and do not mean to imply that the analyzed random variable is normally distribution [6.29].

(a)

(b)
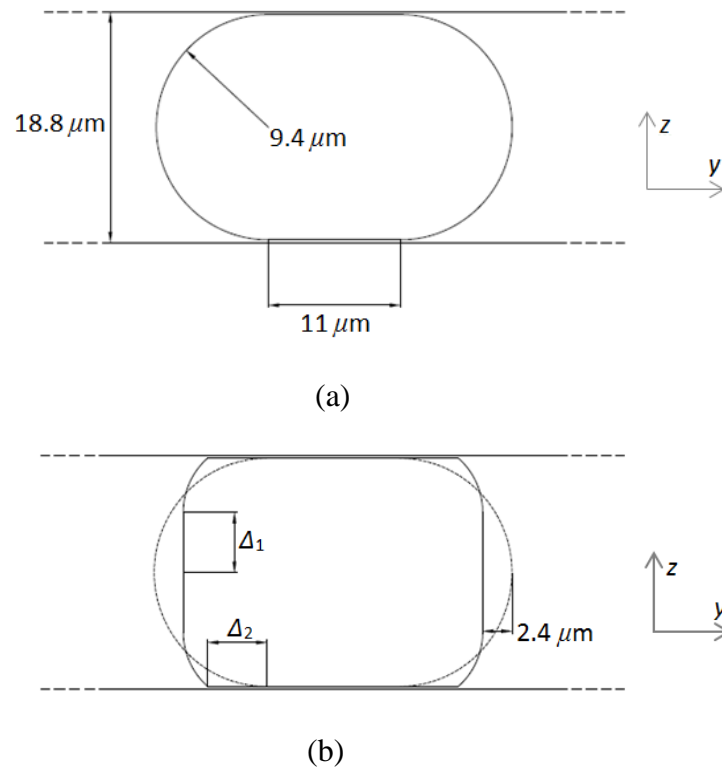
Fig. 6.23 Confined GUV in the microfluidic channel with an $18.8 \ \mu m \times 25 \ \mu m$ cross section: (a) only confined at z-direction, without y-direction restriction; (b) subject to z- and y-direction restriction, the profile in (a) is also drawn together (dash line) for comparison.

Figures 6.24 and 6.25 demonstrate several representative measurement results of the single GUV membrane made up by 100% SM and 100% POPC, respectively. We can see that the flatten area of these GUVs have to spend ~0.6 s to ~0.9 s (1.01 ms per

sampling point in all measurements) to pass through the sensing area (the 500 nm split) and then release themselves. The slightly larger noise at 7.9 GHz is likely from measurement system. More measurement results of S_{21} change between without and with a GUV, i.e., ($S_{21,\text{without}}$-$S_{21,\text{with}}$), are listed in Table 6.4 and 6.5, where the logarithmic unit in Fig. 6.24 and 6.25 are changed to the linear. The probability density functions (PDFs) of the data in magnitude for two types of GUVs at 2.7 GHz and 7.9 GHz are drawn in Fig. 6.26. Figure 6.26(a) indicates that the average S_{21} change from 95.45% (corresponding to $\pm 2\sigma$ away from the mean μ) of SM GUVs ranges from 5.87×10^{-4} to 12.10×10^{-4} and 95.45% of POPC GUVs ranges from 2.34×10^{-4} to 5.83×10^{-4}. Two PDFs in Fig. 6.26(b) are more far away from each than those in Fig. 6.26(a), demonstrating that the restriction is relaxed to $\pm 4\sigma$ away from the mean μ, corresponding to a probability of 99.99%. In other words, the average S_{21} change from 99.99% of SM GUVs ranges from 7.09×10^{-4} to 11.61×10^{-4} and 99.99% of POPC GUVs ranges from -0.755×10^{-4} to 6.97×10^{-4}. These results indicate that the membrane synthesized by SM causes larger $|S_{21}|$ change than POPC. The even-mode resonant frequencies are also tried in the measurement, but there is no significant response on S-parameters.

(a)   (b)

110
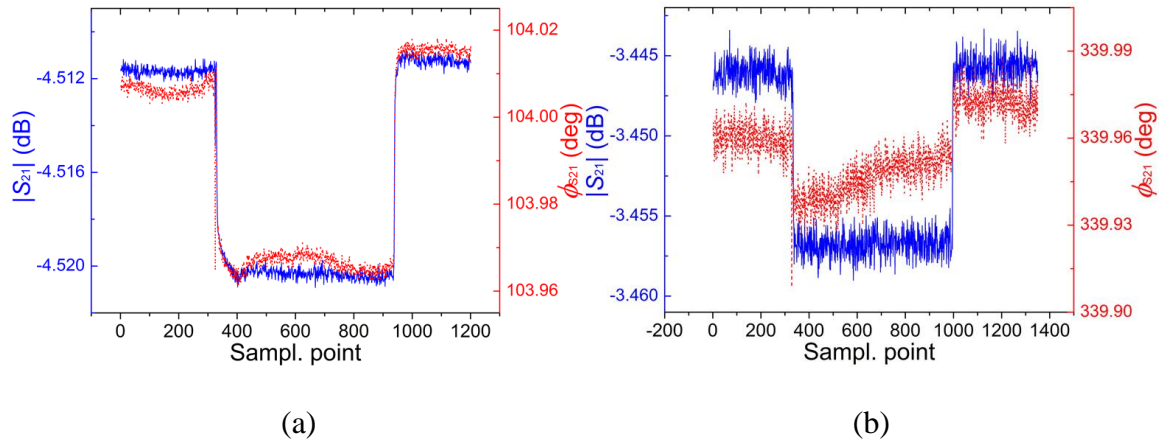
Fig. 6.24 Measurement result of the single GUV membrane made up by 100% SM at (a)

2.7 GHz and (b) 7.9 GHz. Blue solid line: magnitude; red dash line: phase.

(a)   (b)
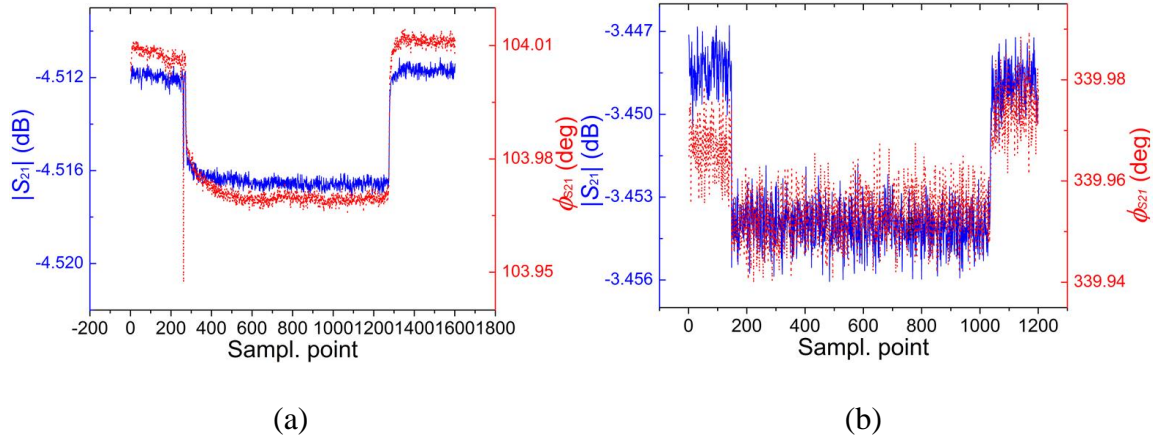
Fig. 6.25 Measurement result of the single GUV membrane made up by 100% POPC at

(a) 2.7 GHz and (b) 7.9 GHz. Blue solid line: magnitude; red dash line: phase.

TABLE 6.4
S_{21} CHANGE BETWEEN WITHOUT AND WITH A SM GUV

#	2.7 GHz $\mu=8.99\times10^{-4}$ $\sigma=1.56\times10^{-4}$	#	7.9 GHz $\mu=9.35\times10^{-4}$ $\sigma=0.57\times10^{-4}$
Fig. 6.24 (a)	$7.19\times10^{-4}\angle138.34^{o}$	Fig. 6.24 (b)	$8.39\times10^{-4}\angle349.71^{o}$
1	$9.78\times10^{-4}\angle142.16^{o}$	1	$9.32\times10^{-4}\angle358.48^{o}$
2	$10.74\times10^{-4}\angle141.84^{o}$	2	$10.03\times10^{-4}\angle356.59^{o}$
3	$10.41\times10^{-4}\angle142.43^{o}$	3	$9.63\times10^{-4}\angle356.92^{o}$
4	$8.38\times10^{-4}\angle144.04^{o}$	4	$9.38\times10^{-4}\angle355.01^{o}$
5	$8.20\times10^{-4}\angle142.27^{o}$	5	$9.18\times10^{-4}\angle356.00^{o}$
6	$9.93\times10^{-4}\angle139.94^{o}$	6	$10.38\times10^{-4}\angle358.44^{o}$
7	$6.34\times10^{-4}\angle144.12^{o}$	7	$9.08\times10^{-4}\angle4.04^{o}$
8	$10.78\times10^{-4}\angle140.71^{o}$	8	$8.88\times10^{-4}\angle357.62^{o}$
9	$8.10\times10^{-4}\angle142.45^{o}$	9	$9.19\times10^{-4}\angle356.26^{o}$

TABLE 6.5

S_{21} Change between without and with a POPC GUV

#	2.7 GHz $\mu=4.09\times10^{-4}$ $\sigma=0.87\times10^{-4}$	#	7.9 GHz $\mu=3.11\times10^{-4}$ $\sigma=0.97\times10^{-4}$
Fig. 6.25 (a)	$5.51\times10^{-4}\angle156.59^{\circ}$	Fig. 6.25 (b)	$4.58\times10^{-4}\angle6.44^{\circ}$
1	$3.17\times10^{-4}\angle153.11^{\circ}$	1	$2.06\times10^{-4}\angle3.41^{\circ}$
2	$4.49\times10^{-4}\angle155.47^{\circ}$	2	$4.34\times10^{-4}\angle8.62^{\circ}$
3	$4.75\times10^{-4}\angle157.04^{\circ}$	3	$4.13\times10^{-4}\angle7.95^{\circ}$
4	$4.72\times10^{-4}\angle156.15^{\circ}$	4	$3.65\times10^{-4}\angle7.01^{\circ}$
5	$3.15\times10^{-4}\angle153.46^{\circ}$	5	$2.85\times10^{-4}\angle6.39^{\circ}$
6	$4.57\times10^{-4}\angle156.36^{\circ}$	6	$2.29\times10^{-4}\angle5.23^{\circ}$
7	$4.16\times10^{-4}\angle154.29^{\circ}$	7	$2.50\times10^{-4}\angle3.35^{\circ}$
8	$2.87\times10^{-4}\angle154.17^{\circ}$	8	$2.40\times10^{-4}\angle358.59^{\circ}$
9	$3.46\times10^{-4}\angle157.11^{\circ}$	9	$2.29\times10^{-4}\angle10.33^{\circ}$

(a)　　　　　　　　　　　(b)
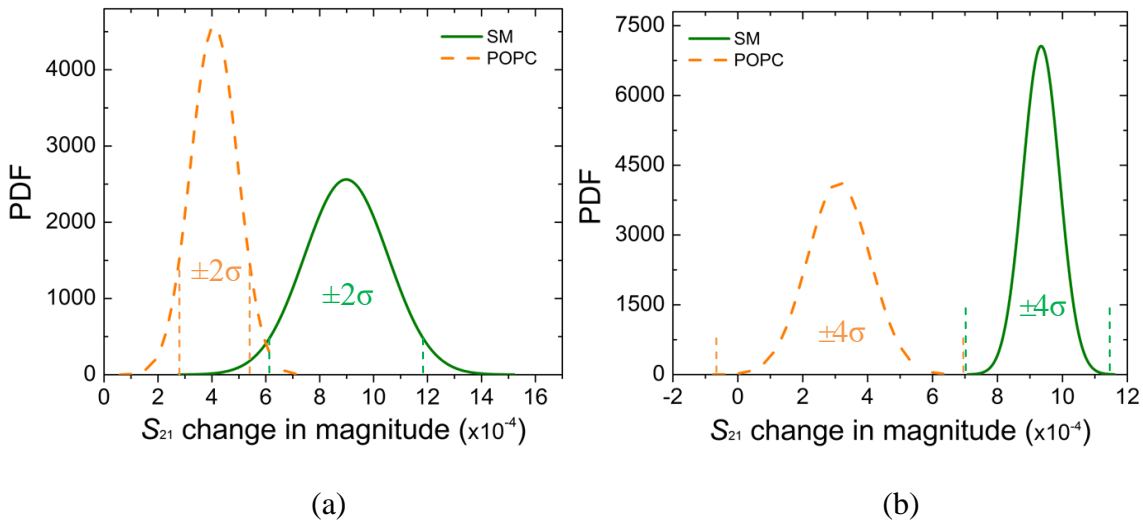
Fig. 6.26 Probability density functions (PDFs) for the average S_{21} change between without and with a SM or POPC GUV in magnitude at (a) 2.7 GHz and (b) 7.9 GHz.

To deserve to be mentioned that, the proposed sensor can also detect the folding of the GUV membrane, taking a SM GUV with a diameter of ~31 μm, as shown in Fig. 6.27(a). For a GUV with diameter smaller than the channel height, it is difficult to control

its vertical position in the channel. As a result, measured signals, as shown in Fig. 27(b), may vary significantly even for identical GUVs. This phenomenon is probably caused by the inconsistent velocities at the front and the back of the GUV when it suffers the friction force coming from the PDMS walls, which is helpful for the research on mechanical properties of lipid bilayer, e.g., elastic energy [6.28]. But these data are not recorded in Table 6.4 and 6.5 since such GUVs are not flatted, subject to more uncertainty in dimension, therefore.

(a)   (b)
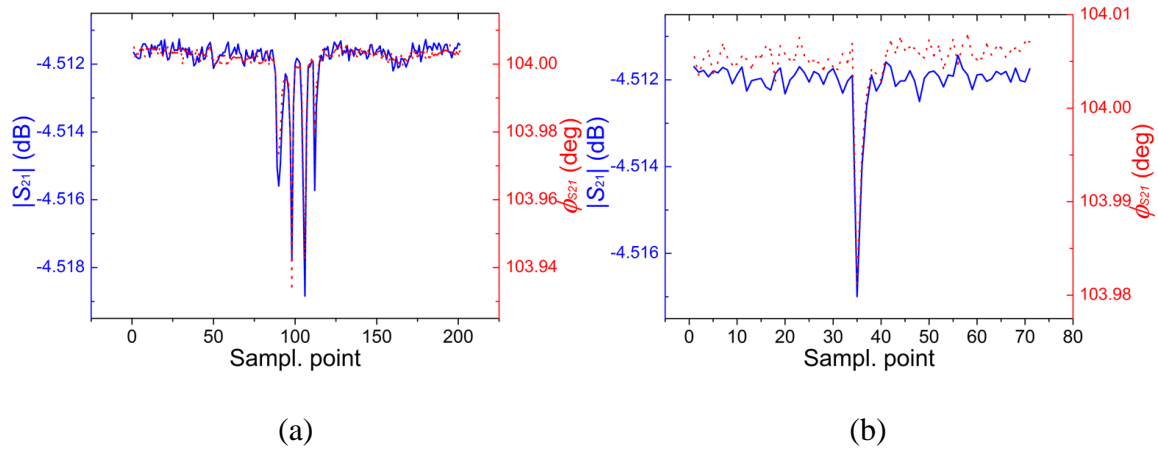
Fig. 6.27 $|S_{21}|$ response for (a) a folding SM GUV and (b) a GUV with diameter smaller than the channel height both at 2.7 GHz. Blue solid line: magnitude; red dash line: phase.

After making sure that there is enough significant dielectric difference between SM and POPC lipid membranes, the GUVs are re-synthesized using the recipe in Table 6.3 for the heterogeneity detection. The same measurement steps are also adopted for data-recording. Figure 6.28 shows some characteristic time-domain $|S_{21}|$ measurement results of attached single GUV membranes at 2.7 GHz and 7.9 GHz, where signal leaps

113

are produced by different domains. The imaging of GUVs in the channel is shot by a camera connected to the fluorescent microscope, which is focused to the surface of the metal layer for capturing the bottom surface of GUVs touching the split. At this time, the raft-like and non-raft domains with different colors are also shot. The imaging before the GUV in Fig. 6.28(a) enters the narrow channel (the 18.8 μm $\times$ 25 μm cross section) for sensing is shown in Fig. 6.29. It is observed that some "ghost" membranes tend to adhere around the inlet junction of narrow channel caused by too large GUVs passing early, which are always blocked there and then explode due to shear. This phenomenon was also observed in A. Yamada *et al*'s work [6.28]. However, these "ghost" membranes only float around the inlet junction and enough far ways the split on the metal line. So the disturbance from them is considered to be negligible. In the experiment, it is observed that the raft-like domain (green color) always locate at the front of a GUV in the microfluidic channel, like that in Fig. 6.29, probably caused by the moving outer fluid [6.28], [6.30]. When a GUV enters the narrow channel, it will be flattened at the walls and slowly pass through the narrow channel, like those in Figs. 6.24 and 6.25. Then the raft-like domain touches the split, as shown in Fig. 6.30(a), inducing the first $|S_{21}|$ falling, named as "Section *I*". Next, the non-raft domain touches the split shown in Fig. 6.30(b), inducing the second $|S_{21}|$ falling, named as "Section *II*". Table 6.6 summarizes S_{21} changes at Sections *I* and *II* corresponding to the GUVs in Fig. 6.28 (a)-(d), where all changes are relative to the S_{21} without GUVs. These values are also labeled in Fig. 6.26, which is now re-drawn as Fig. 6.31.

From the probabilities listed in Table 6.7, Section *I* is much more likely to be SM, and Section *II* is much more likely to be POPC. This also agrees with the fluorescent label indications in Fig. 6.28. So the proposed measurement is able to detect different domains on a GUV. It is worth noting that the addition of Chol does not significantly change $\Delta|S_{21}|$ for the SM response. A possible reason is that the dipole moment of Chol molecule is much smaller than that of lipid molecule, i.e., one order of magnitude as pointed out in [6.31].
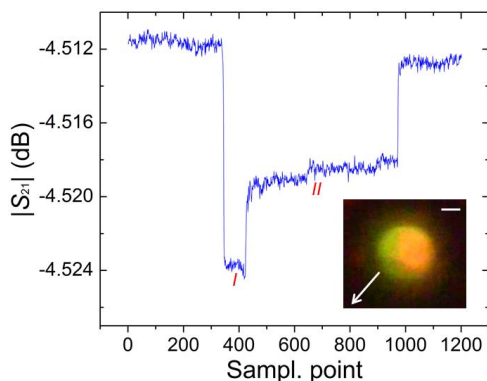
(a)
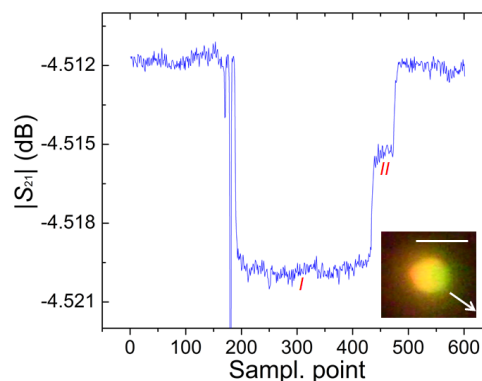
(b)
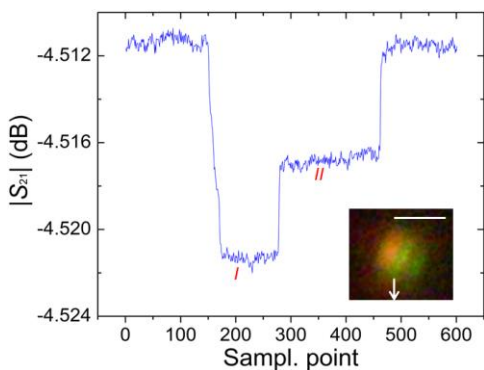
(c)
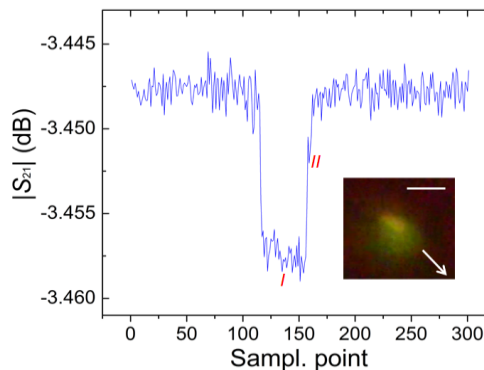
(d)

Fig. 6.28 Time-domain $|S_{21}|$ measurements of single GUVs passing through the split at
(a)-(c) 2.7 GHz and at (d) 7.9 GHz. The arrows indicate the flow directions before these
GUVs enter the narrow channel. Bar: 25 μm.
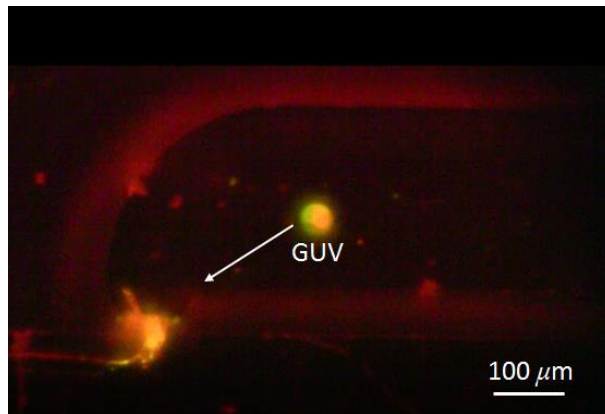
Fig. 6.29 Imaging before the GUV in Fig. 6.28(a) enters the narrow channel for sensing.
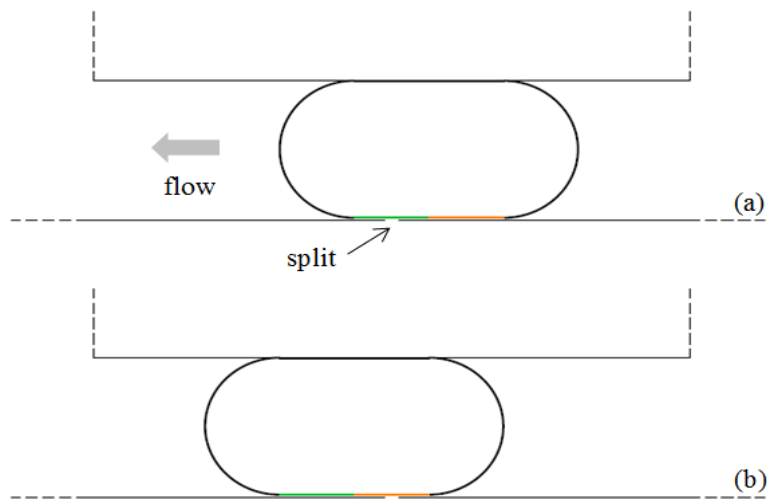
Fig. 6.30 Cross section of (a) raft-like or (b) non-raft domain on a GUV touching the split
in the channel.

(a)   (b)
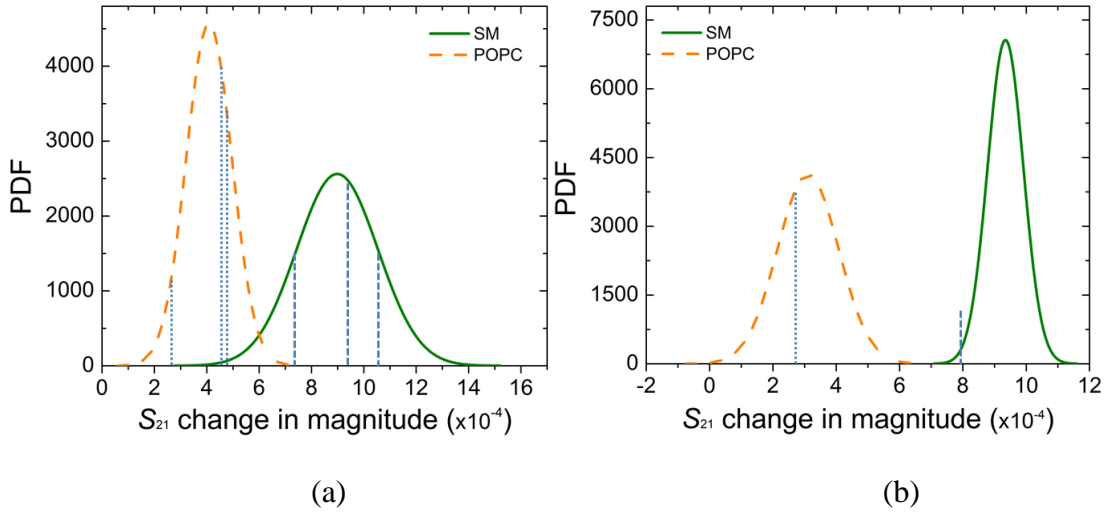
Fig. 6.31 PDFs for the average S_{21} change in magnitude at (a) 2.7 GHz and at (b) 7.9 GHz

with labeled values in Table 6.6. Straight dash line: Section *I*; straight dot line: Section *II*.

TABLE 6.6
S_{21} CHANGES AT SECTIONS *I* AND *II*
CORRESPONDING TO THE GUVS IN FIG. 6.28

#	Section *I*	Section *II*
(a)	$10.64 \times 10^{-4} \angle 144.16^{\mathrm{o}}$	$4.55 \times 10^{-4} \angle 140.68^{\mathrm{o}}$
(b)	$9.29 \times 10^{-4} \angle 146.09^{\mathrm{o}}$	$4.74 \times 10^{-4} \angle 144.50^{\mathrm{o}}$
(c)	$7.32 \times 10^{-4} \angle 144.56^{\mathrm{o}}$	$2.92 \times 10^{-4} \angle 142.38^{\mathrm{o}}$
(d)	$7.91 \times 10^{-4} \angle 356.32^{\mathrm{o}}$	$2.71 \times 10^{-4} \angle 0.82^{\mathrm{o}}$

Note: (a)-(c) at 2.7 GHz; (d) at 7.9 GHz.

TABLE 6.7
PROBABILITY RATIOS OF SM VS. POPC FOR
SECTIONS *I* & *II* IN 4 TYPICAL MEASUREMENTS

Section #	Label Color	Fig. 6.28 (#)	Probability[*] SM/POPC
I	Green	(a)	13.6%/0.27%
		(b)	34.1%/0.27%
		(c)	13.6%/0.27%
		(d)	2.14%/0.0031%
II	Orange	(a)	2.27%/34.1%
		(b)	2.27%/34.1%
		(c)	2.27%/13.6%
		(d)	~0%/34.1%

6.4 Analytical Model of the SRR

To analyze, design, and extract the permittivity of MUT locating at the split, an appropriate model of the proposed SRR is required. Some equivalent circuit-based models have been proposed to meet the demand [6.32]-[6.34]. However, these existing models have to fit and adjust lumped-element parameters to agree with the measured *S*-parameters. Moreover, these fitted parameters are not always unique, which brings a great uncertainty for permittivity extraction. To address this issue, in this dissertation, a novel analytical model is first proposed. Using the model, *S*-parameters of the SRR can be determined by necessary dimensions and dielectric information of substrate.

The proposed SRR can be modeled as shown in Fig. 6.32, which is composed of a coupled line and a gaped ML, discussed in Section 6.4.1 and 6.4.2, respectively. Then, using the even-odd mode analysis technique [6.35], they are combined together for the final 2-port *S*-parameters in Section 6.4.3. For the well-matched MLs on the left and right, they only shift the phase of the combined *S*-parameters. So the total phase of the SRR will be revised using the measurement result as reference.
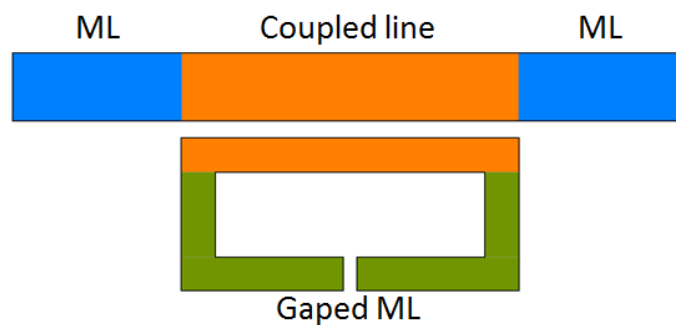
Fig. 6.32 Decomposition of the SRR. Blue: ML; orange: coupled line; green: gaped ML.

6.4.1 *S*-parameters of Asymmetric Coupled Line

For a four-port asymmetric coupled line made up by two adjacent MLs *a* and *b* with a spacing *s* and arbitrary widths W_1 and W_2 in Fig. 6.33, its *S*-parameters can be expressed as

$$[S]=\begin{bmatrix} S_{11} & S_{12} & S_{13} & S_{14} \\ S_{21} & S_{22} & S_{23} & S_{24} \\ S_{31} & S_{32} & S_{33} & S_{34} \\ S_{41} & S_{42} & S_{43} & S_{44} \end{bmatrix}=\begin{bmatrix} S_{11} & S_{21} & S_{31} & S_{41} \\ S_{21} & S_{11} & S_{41} & S_{31} \\ S_{31} & S_{41} & S_{33} & S_{43} \\ S_{41} & S_{31} & S_{43} & S_{44} \end{bmatrix} \tag{6.3}$$

where $S_{11}=S_{22}$, $S_{21}=S_{12}$, $S_{33}=S_{44}$, $S_{43}=S_{34}$, $S_{31}=S_{13}=S_{42}=S_{24}$, $S_{41}=S_{14}=S_{32}=S_{23}$, because of the symmetry and reciprocity [6.36].
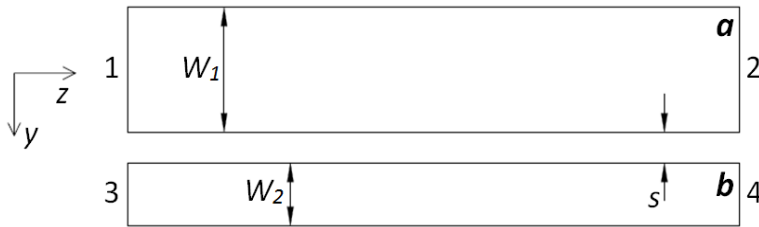
Fig. 6.33 Four-port asymmetric coupled line with a spacing *s* and arbitrary widths W_1 and W_2.

Under the assumption of transverse electromagnetic (TEM) propagation, the wave propagation along *y* direction in Fig. 6.33, is described by conventional transmission-line theory [6.37] as

$$\frac{d[V]}{dy} = -[z][I] \qquad (6.4)$$

where $[V] = [\begin{smallmatrix} V_1 \\ V_3 \end{smallmatrix}]$, $[I] = [\begin{smallmatrix} I_1 \\ I_3 \end{smallmatrix}]$, the elements V_i and I_i ($i=1, 3$) represent the voltage and current

at the port i of the network. And the impedance matrix is

$$[z] = [\begin{smallmatrix} z_{11} & z_{13} \\ z_{31} & z_{33} \end{smallmatrix}] = [\begin{smallmatrix} z_{11} & z_{31} \\ z_{31} & z_{33} \end{smallmatrix}] \qquad (6.5)$$

where $z_{13}=z_{31}$ because of the reciprocity [6.36]. Now we solve the following eigenvalue

equation for $[z]$:

$$([z] - \lambda[E])[x] = 0 \qquad (6.6)$$

where $[E]$ is the unity matrix, and $[x]$ corresponding to voltage modes is eigenvectors of

$[z]$, solved as

$$\overrightarrow{x_a} = [\begin{smallmatrix} m \\ 1 \end{smallmatrix}] = [\begin{smallmatrix} \dfrac{z_{11} + z_{33} - \sqrt{z_{11}^2 - 2z_{11}z_{33} + 4z_{31}^2 + z_{33}^2}}{2z_{31}} - \dfrac{z_{33}}{z_{31}} \\ 1 \end{smallmatrix}] \qquad (6.7)$$

$$\overrightarrow{x_b} = [\begin{smallmatrix} n \\ 1 \end{smallmatrix}] = [\begin{smallmatrix} \dfrac{z_{11} + z_{33} + \sqrt{z_{11}^2 - 2z_{11}z_{33} + 4z_{31}^2 + z_{33}^2}}{2z_{31}} - \dfrac{z_{33}}{z_{31}} \\ 1 \end{smallmatrix}] \qquad (6.8)$$

The eigenvalue $[\lambda]$ is also calculated as

$$\lambda_1 = \frac{z_{11} + z_{33} - \sqrt{z_{11}^2 - 2z_{11}z_{33} + 4z_{31}^2 + z_{33}^2}}{2} \qquad (6.9)$$

$$\lambda_3 = \frac{z_{11} + z_{33} + \sqrt{z_{11}^2 - 2z_{11}z_{33} + 4z_{31}^2 + z_{33}^2}}{2} \qquad (6.10)$$

Then, from the capacitance matrix $[\begin{smallmatrix} Q_1 \\ Q_3 \end{smallmatrix}] = [\begin{smallmatrix} c_{11} & c_{13} \\ c_{31} & c_{33} \end{smallmatrix}][\begin{smallmatrix} V_1 \\ V_3 \end{smallmatrix}] = [\begin{smallmatrix} c_{11} & c_{31} \\ c_{31} & c_{33} \end{smallmatrix}][\begin{smallmatrix} V_1 \\ V_3 \end{smallmatrix}]$, we have the

following static capacitances to ground per unit length for each conductor (a and b):

(1) Differential Mode (π)

$$C_{a\pi} = c_{11} + \frac{1}{m}c_{31} \tag{6.11}$$

$$C_{b\pi} = mc_{31} + c_{33} \tag{6.12}$$

(2) Common Mode (c)

$$C_{ac} = c_{11} + \frac{1}{n}c_{31} \tag{6.13}$$

$$C_{bc} = nc_{31} + c_{33} \tag{6.14}$$

where the self-capacitance coefficients c_{11}, c_{33} are solved using $c_p + 2c_f$ from eqs. (3)-(4) in

[6.38], the mutual-capacitance coefficients c_{31} for two adjacent asymmetric lines is

solved using $C_0^{ACPS} \cdot \varepsilon_{eff}^{ACPS}$ from eqs. (10) and (39) in [6.39].

To order to obtain the same modal impedances for two conductors, in the above

equations, $C_{a\pi} = C_{b\pi}$ and $C_{ac} = C_{bc}$ should be met. Then we have

$$m = \frac{-(c_{33} - c_{11}) - \sqrt{(c_{33} - c_{11})^2 + 4c_{31}^2}}{2c_{31}} \tag{6.15}$$

$$n = \frac{-(c_{33} - c_{11}) + \sqrt{(c_{33} - c_{11})^2 + 4c_{31}^2}}{2c_{31}} \tag{6.16}$$

It is worth noting that $mn = -1$, which will be used in some later calculations. For a

special case when the conductor a and b in Fig. 6.33 are the same, $m = -1$, $n = 1$. Then, the

mode impedances are written as

$$z_{a\pi} = \frac{1}{v_{a\pi} C_{a\pi}} = \frac{1}{v_{a\pi}(c_{11} + c_{31}/m)} \tag{6.17}$$

$$z_{b\pi} = \frac{1}{v_{b\pi} C_{b\pi}} = \frac{1}{v_{b\pi}(mc_{31} + c_{33})} \tag{6.18}$$

$$z_{ac} = \frac{1}{v_{ac} C_{ac}} = \frac{1}{v_{ac}(c_{11} + c_{31}/n)} \tag{6.19}$$

$$z_{bc} = \frac{1}{v_{bc} C_{bc}} = \frac{1}{v_{bc}(nc_{31} + c_{33})} \tag{6.20}$$

Because of $C_{a\pi} = C_{b\pi}$ and $C_{ac} = C_{bc}$, we have

$$Z_{\pi} = \frac{1}{v_{\pi}(c_{11} + c_{31}/m)} \tag{6.21}$$

$$Z_c = \frac{1}{v_c(c_{11} + c_{31}/n)} \tag{6.22}$$

The reflection and transmission coefficients of each mode in terms of

corresponding mode impedances and electrical lengths are expressed as

$$\Gamma_x = j[[\frac{Z_x}{Z_0} - \frac{Z_0}{Z_x}]/\sin\theta_x]/\phi_x \tag{6.23}$$

$$T_x = 2/\phi_x \tag{6.24}$$

$$\phi_x = 2\cos\theta_x + j(\frac{Z_x}{Z_0} + \frac{Z_0}{Z_x})/\sin\theta_x \tag{6.25}$$

For the asymmetric a and b (as a result, we use π and c instead of odd and even denoting

modes), these equations (6.23)-(6.25) have verified by V. K. Tripathi *et al* [6.40].
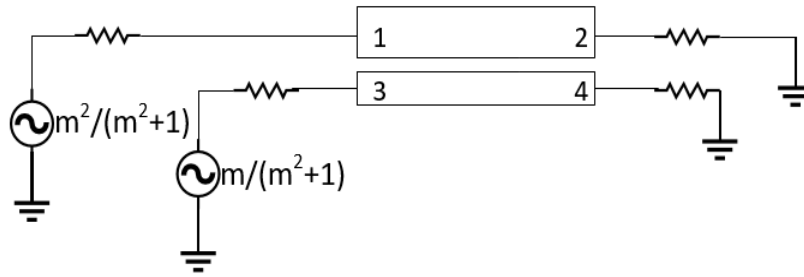
(a)
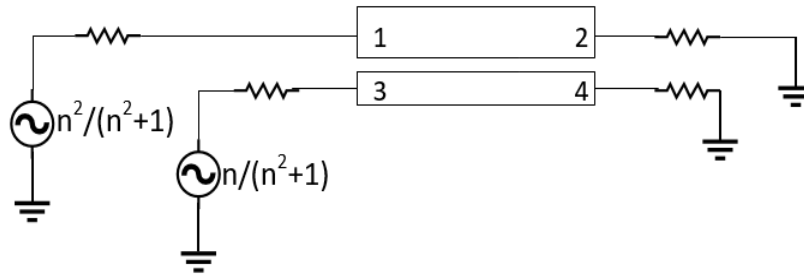
(b)

Fig. 6.34 System of generators for derivation of the S-parameters for an overall 1 V input signal at port 1: (a) π Mode; (b) c Mode.

S-parameters of this system can be solved using voltage generators at each matched port, e.g., S_{11}, S_{21}, S_{31} and S_{41} can be determined by the emerging voltage waves at all ports to an incident voltage wave at port 1, shown in Fig. 6.34.

For an applied 1 V voltage at Port 1, the voltages at two conductors can be solved as

(1) Differential Mode (π)

$$\frac{1}{1+(\frac{1}{m})^2} = \frac{m^2}{m^2+1} \quad \text{for port 1} \tag{6.26}$$

$$\frac{\dfrac{1}{m}}{1+(\dfrac{1}{m})^2} = \frac{m}{m^2+1} \quad \text{for port 3} \qquad (6.27)$$

(2) Common Mode (*c*)

$$\frac{1}{1+(\dfrac{1}{n})^2} = \frac{n^2}{n^2+1} \quad \text{for port 1} \qquad (6.28)$$

$$\frac{\dfrac{1}{n}}{1+(\dfrac{1}{n})^2} = \frac{n}{n^2+1} \quad \text{for port 3} \qquad (6.29)$$

One can easily prove that

$$\frac{m^2}{m^2+1} + \frac{n^2}{n^2+1} = 1 \qquad (6.30)$$

and $$\frac{m}{m^2+1} + \frac{n}{n^2+1} = 0 \qquad (6.31)$$

The reflection and transmission coefficients for each mode are the same on each of the conductor *a* and *b* since $z_{a\pi}=z_{b\pi}$ and $z_{ac}=z_{bc}$. Now we obtain

$$S_{11} = \frac{m^2}{m^2+1}\Gamma_{OE} + \frac{n^2}{n^2+1}\Gamma_{EE} \qquad (6.32)$$

$$S_{21} = \frac{m^2}{m^2+1}T_{OE} + \frac{n^2}{n^2+1}T_{EE} \qquad (6.33)$$

$$S_{31} = \frac{m}{m^2+1}\Gamma_{OE} + \frac{n}{n^2+1}\Gamma_{EE} \qquad (6.34)$$

$$S_{41} = \frac{m}{m^2+1}T_{OE} + \frac{n}{n^2+1}T_{EE} \qquad (6.35)$$

Similarly, to apply an overall 1 V voltage at Port 3, the distribution of voltages at two conductors shown in Fig. 6.35 can be solved:

(1) Differential Mode (π)

$$\frac{m}{m^2+1} \quad \text{for port 1} \tag{6.36}$$

$$\frac{1}{m^2+1} \quad \text{for port 3} \tag{6.37}$$

(2) Common Mode (c)

$$\frac{n}{n^2+1} \quad \text{for port 1} \tag{6.38}$$

$$\frac{1}{n^2+1} \quad \text{for port 3} \tag{6.39}$$
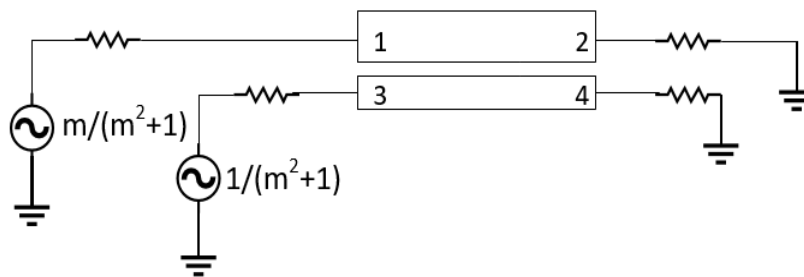
(a)
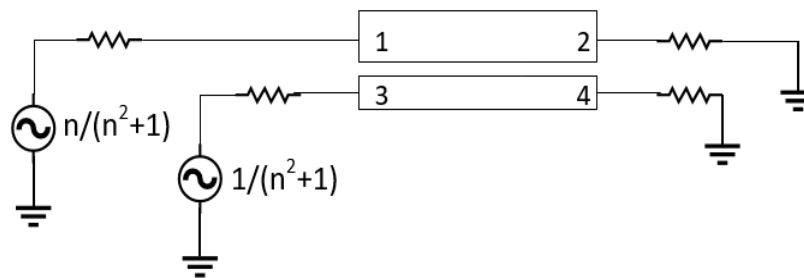
(b)

Fig. 6.35 System of generators for derivation of the *S*-parameters for an overall 1 V input signal at port 3: (a) π Mode; (b) *c* Mode.

Similarly, S_{13}, S_{33}, S_{43}, S_{23} can be also solved:

$$S_{13} = \frac{m}{m^2+1}\Gamma_{OE} + \frac{n}{n^2+1}\Gamma_{EE} \tag{6.40}$$

$$S_{33} = \frac{1}{m^2+1}\Gamma_{OE} + \frac{1}{n^2+1}\Gamma_{EE} \tag{6.41}$$

$$S_{43} = \frac{1}{m^2+1}T_{OE} + \frac{1}{n^2+1}T_{EE} \tag{6.42}$$

$$S_{23} = \frac{m}{m^2+1}T_{OE} + \frac{n}{n^2+1}T_{EE} \tag{6.43}$$

Let us go back to the matrix (6.3), we can find that all remaining *S*-parameters are also obtained therefore from $S_{11}=S_{22}$, $S_{21}=S_{12}$, $S_{33}=S_{44}$, $S_{43}=S_{34}$, $S_{31}=S_{13}=S_{42}=S_{24}$, $S_{41}=S_{14}=S_{32}=S_{23}$.

6.4.2 Reflection Coefficient of Gaped ML

Many publications have presented the modeling of the split area. The analytic mathematic expression is very complicated even for the simplest case that only includes necessary conductor and dielectric substrate [6.41]-[6.43]. These models do not consider a top dielectric layer above the metal, e.g., the microfluidic channel filled with a solution. In this section, a π-network of capacitors [6.44] shown in Fig. 6.36 will be used to model this area to obtain an effective and simple quantification.
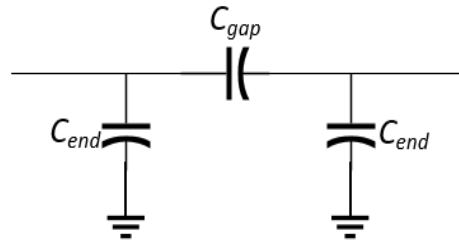
Fig. 6.36 π-network of capacitors for the equivalent circuit of the split.
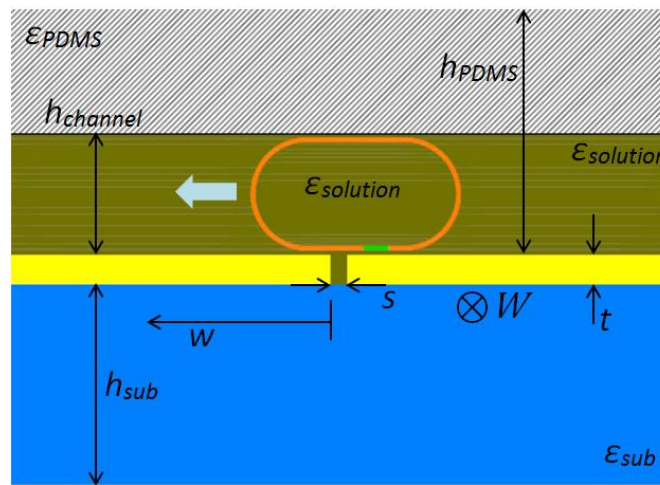
Fig. 6.37 Cross-section of the substrate/metal layer/GUV bottom surface/liquid inside the GUV/GUV top surface/PDMS/air system. The thickness of the GUV membrane is not drawn in an actual proportion to improve readability.

The following will introduce how to solve C_{end} and C_{gap} in Fig. 6.36, respectively. Although some fitting equations are reported [6.44], these equations are generally not applicable to the multiple layer system of substrate/metal layer/GUV bottom surface/solution inside the GUV/GUV top surface/PDMS/air shown in Fig. 6.37. So, some more practical and applicable to the multiple layer system for C_{gap} calculation

needs to be established. For C_{end}, however, most of electric fields emitted from edge only penetrate substrate material and terminate at the back conductor, rather than another conductor, so the fitting equation of C_{end} is applicable. According to [6.44],

$$C_{end} = 0.5\{12W(\frac{\varepsilon_{sub}}{9.6})^{0.9}(\frac{s}{W})^{0.8675}\exp(2.043(\frac{W}{h})^{0.12})\}(pF) \qquad (6.44)$$

where s is the gap width, ε_{sub} and h are the dielectric constant and thickness of the substrate, respectively, and W is the width of the ML, which is different from the length w and perpendicular to the cross section in Fig. 6.37.

As discussed in Section 6.3, when the GUV with a slightly larger diameter than the channel passes through the sensing split, the bottom/top area on the GUV touching split/PDMS channel can be treated approximately as a flattened surface with a thickness of h_{GUV}, i.e., 2.8 nm or 3.5 nm for different phases [6.1]-[6.3], as shown in Fig. 6.37. However, the conformal mapping technique [6.45] requires both the top and bottom surfaces to cover the whole metal layer. The requirement is not met. Provided that the GUV bottom surface is a thin sheet tightly attached on the metal layer, it can be approximately seen as a dielectric filled in the parallel-plate capacitor formed by the split. Using the conformal mapping in E. Chen et al's work [6.45], the total capacitance per unit length between two adjacent metals shown in Fig. 6.37 are written by

$$C_{channel}(\varepsilon_x = \varepsilon_x' - j\varepsilon_x'') = \varepsilon_0\varepsilon_{air}\frac{K(k_{air}')}{K(k_{air})}(1 + \frac{\varepsilon_{sub}-1}{2}\frac{K(k_{sub})}{K(k_{sub}')}\frac{K(k_{air}')}{K(k_{air})} + \frac{\varepsilon_{PDMS}-1}{2}\frac{K(k_{PDMS})}{K(k_{PDMS}')}\frac{K(k_{air}')}{K(k_{air})}$$
$$+ \frac{\varepsilon_{solution}-\varepsilon_{PDMS}}{2}\frac{K(k_{solution})}{K(k_{solution}')}\frac{K(k_{air}')}{K(k_{air})}) + \varepsilon_0(\varepsilon_{GUV}-\varepsilon_{solution})\frac{h_{GUV}}{s}$$

$$(6.45)$$

$$and \qquad\qquad k_{air} = \frac{s}{s+2w} \qquad\qquad (6.46)$$

$$k_{sub} = \frac{\sinh(\frac{\pi s}{4h_{sub}})}{\sinh(\frac{\pi(s+2w)}{4h_{sub}})} \qquad\qquad (6.47)$$

$$k_{PDMS} = \frac{\sinh(\frac{\pi s}{4h_{PDMS}})}{\sinh(\frac{\pi(s+2w)}{4h_{PDMS}})} \qquad\qquad (6.48)$$

$$k_{solution} = \frac{\sinh(\frac{\pi s}{4h_{solution}})}{\sinh(\frac{\pi(s+2w)}{4h_{solution}})} \qquad\qquad (6.49)$$

$$and \qquad\qquad k_x{}' = \sqrt{1-k_x{}^2} \qquad\qquad (6.50)$$

where *x=air*, *sub*, *PDMS*, and *solution*, *K* is incomplete elliptic integral of the first kind

with variables k_x and k_x'. It is worth to be mentioned that in Fig. 6.17 the microfluidic

channel does not cover the whole metal layer but only ~100 μm long on each side taking

the split as the center. So *w*=100 μm is selected for the calculations of eqs. (6.45)-(6.50).

From Fig. 6.17, the microfluidic channel is only 25 μm wide ($\otimes$ direction in Fig.

6.37), so most of the split is covered by PDMS, not solution. Similarly, the capacitance

C_{wall} per unit length for the cross section without the microfluidic channel is expressed as

$$C_{wall}(\varepsilon_x = \varepsilon_x{}' - j\varepsilon_x{}'') = \varepsilon_0\varepsilon_{air}\frac{K(k_{air}{}')}{K(k_{air})}(1 + \frac{\varepsilon_{sub}-1}{2}\frac{K(k_{sub})}{K(k_{sub}{}')}\frac{K(k_{air}{}')}{K(k_{air})} + \frac{\varepsilon_{PDMS}-1}{2}\frac{K(k_{PDMS})}{K(k_{PDMS}{}')}\frac{K(k_{air}{}')}{K(k_{air})})$$

$$(6.51)$$

Consequently, C_{gap} can be obtained as a shunt connection using $C_{channel}$ and C_{wall} in parallel:

$$C_{gap} = w_{channel}C_{channel} + w_{wall}C_{wall} \qquad (6.52)$$

where $w_{channel}$=25 μm is the width of microfluidic channel, and w_{wall}=75 μm is the width of electrodes covered by PDMS.

In eq. (6.45), the capacitance of the GUV bottom surface is in the form of a parallel-plate capacitance, rather than an elliptic function based on the conformal mapping technique like other layers, since the use of a thickness of 2.8 nm or 3.5 nm causes the calculation error, i.e., $K(k_{GUV})/K(k_{GUV}')$=0. The parameters k_{GUV} and k_{GUV}' can be obtained similarly from eq. (6.50) and any one from eq. (6.47) to (6.49). Figure 6.38 demonstrates the electric field distribution (blue lines) around the 500 nm-wide split. The used method to draw Fig. 6.38 is introduced in Appendix B. A flatten GUV membrane with ~3 nm thickness is also drawn together, where the membrane over the split is marked in red and other parts are marked in orange. We can see that the red part is approximately inside a parallel-plate capacitor. For the orange part, it is approximately between two long-distance parallel-plates aside the split. As rough estimations, provided that ε_{GUV}=73 and $\varepsilon_{solution}$=76, the capacitance change per unit length of the red part between without and with the membrane is

$$\varepsilon_0(\varepsilon_{solution} - \varepsilon_{GUV})\frac{h_{GUV}}{s} = (76-73)\varepsilon_0 \times \frac{3\times10^{-9}}{500\times10^{-9}} = 0.018\varepsilon_0 C/m \qquad (6.53)$$

For the total 1000 nm-long ($2l_{orange}$) orange parts aside the split, it is calculated as

$$\varepsilon_0 \varepsilon_{solution} \frac{l_{orange}}{curve} - \cfrac{1}{\cfrac{1}{\varepsilon_0 \varepsilon_{GUV} \cfrac{l_{orange}}{h_{GUV}}} + \cfrac{1}{\varepsilon_0 \varepsilon_{solution} \cfrac{l_{orange}}{(curve - h_{GUV})}}}$$

$$= 76\varepsilon_0 \times \frac{500 \times 10^{-9}}{1.35 \times 10^{-6}} - \cfrac{1}{\cfrac{1}{73\varepsilon_0 \times \cfrac{500 \times 10^{-9}}{3 \times 10^{-9}}} + \cfrac{1}{76\varepsilon_0 \times \cfrac{500 \times 10^{-9}}{(1.35 \times 10^{-6} - 3 \times 10^{-9})}}} \qquad (6.54)$$

$$= 0.00259\varepsilon_0 \, C/m$$

where the distance 1.35×10^{-6} m (symbolled by *curve*) between two parallel-plates is

obtained using the complete elliptic integral of the second kind. The halved ellipse

beginning at 9.9975×10^{-4} ending at 10.0075×10^{-4}, as shown in Fig. 6.39, is selected as the

average distance. More capacitance changes can be also calculated using the similar

equation, e.g., the next 1000 nm is calculated to be $0.000565\varepsilon_0$ C/m. That implies that the

farther away from the split, the smaller the capacitance change between with and without

the membrane. So the approximation of the parallel-plate capacitance in eq. (6.45) is

reasonable to evaluate the capacitance of the GUV bottom surface.

131
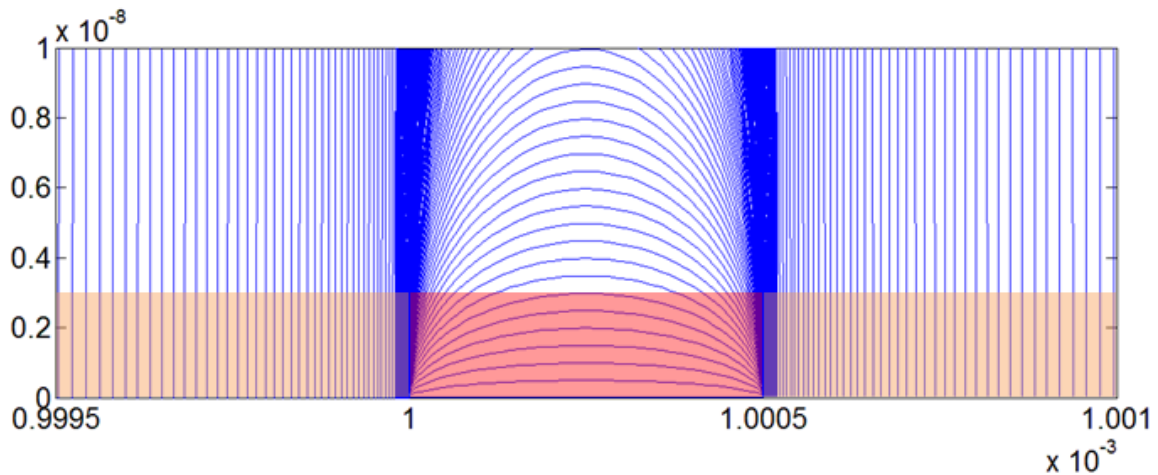
Fig. 6.38 Electric field distribution around the 500 nm-wide split (horizontal direction, from 1.0000×10^{-3} m to 1.0005×10^{-3} m). Red: the GUV membrane over the split; orange: other parts of the membrane aside the split.
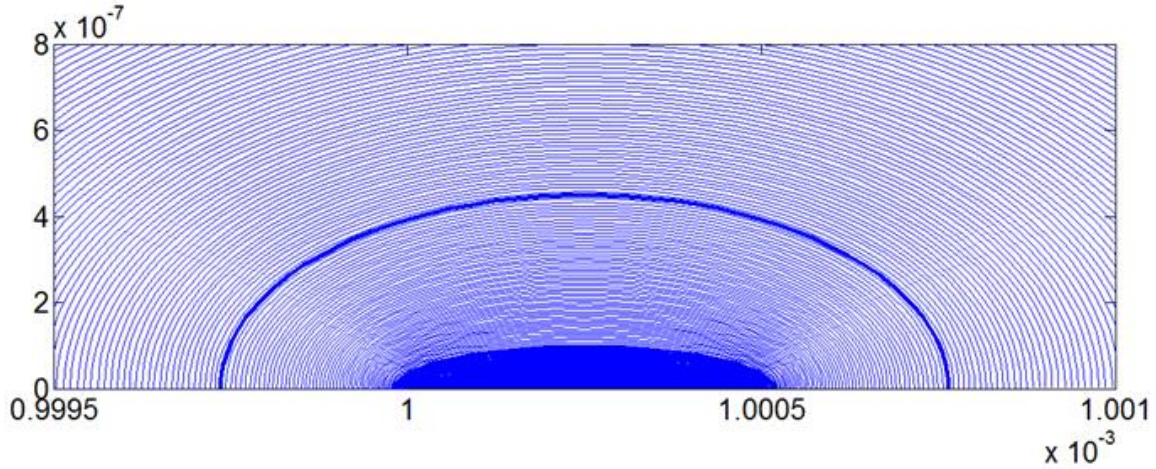
Fig. 6.39 A selected (bold) curve as the average distance between two 500 nm-long parallel-plates along horizontal direction. One plate: from 0.9995×10^{-3} m to 1.0000×10^{-3} m; another plate: from 1.0005×10^{-3} m to 1.0010×10^{-3} m.

6.4.3 Combination of Coupled Line and Gaped ML

The *S*-parameters of the symmetric SRR can be solved by analyzing its odd and even modes. Under odd and even mode excitations, it becomes to Fig. 6.40 (a) and (b) [6.35]. From Fig. 6.40(b), the capacitance C_{gap}, an equivalence of the split, does not play any role under the even-mode excitation.

We can solve the reflections $S_{11}{}^{o}$ and $S_{11}{}^{e}$ at Port 1 from Fig. 6.40 (a) and (b). The complete *S*-parameters of the SRR are expressed as

$$S_{11} = \frac{S_{11}{}^e + S_{11}{}^o}{2}$$

(6.55)

$$S_{21} = \frac{S_{11}{}^e - S_{11}{}^o}{2}$$

(6.56)
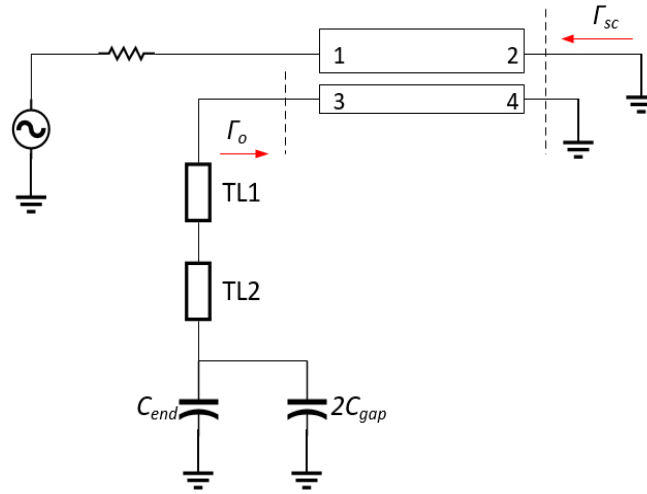
(a)
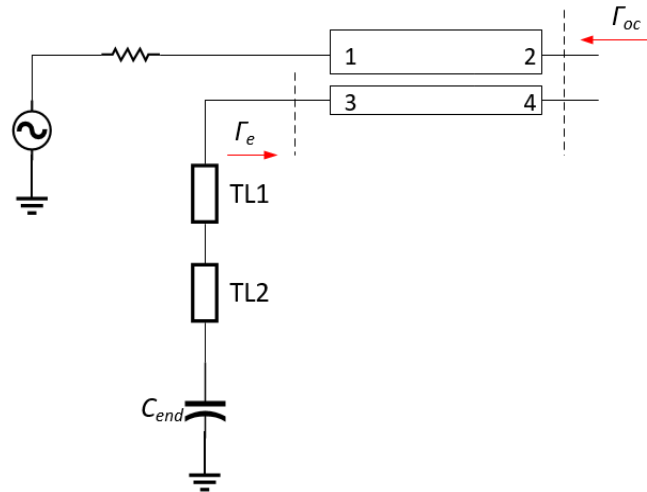
(b)

Fig. 6.40 Bisection of the circuit of the symmetric SRR under (a) odd-mode and (b) even-mode excitations. The length of the 4-port coupled line needs to be halved here.

The following will take the odd mode as an example to demonstrate how to solve $S_{11}{}^o$. The solving method of $S_{11}{}^e$ is similar to $S_{11}{}^o$. It is analyzed by the following signal flow [6.46], where $\Gamma_{sc}=-1$ for short-circuit.
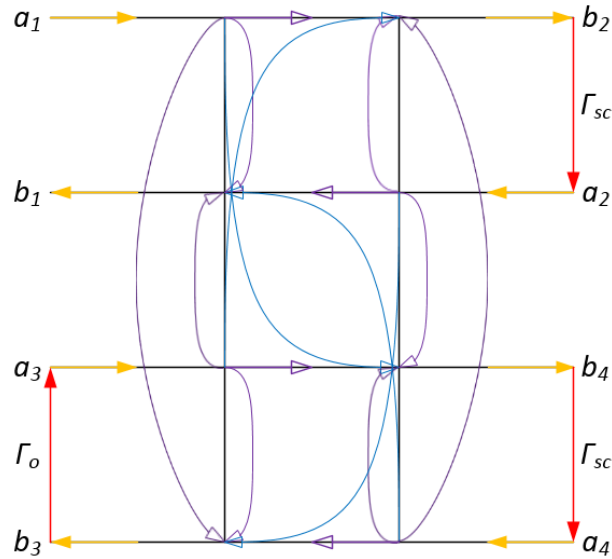
Fig. 6.41 Signal flow graph for the analysis of $S_{11}{}^o$.

(a)   (b)
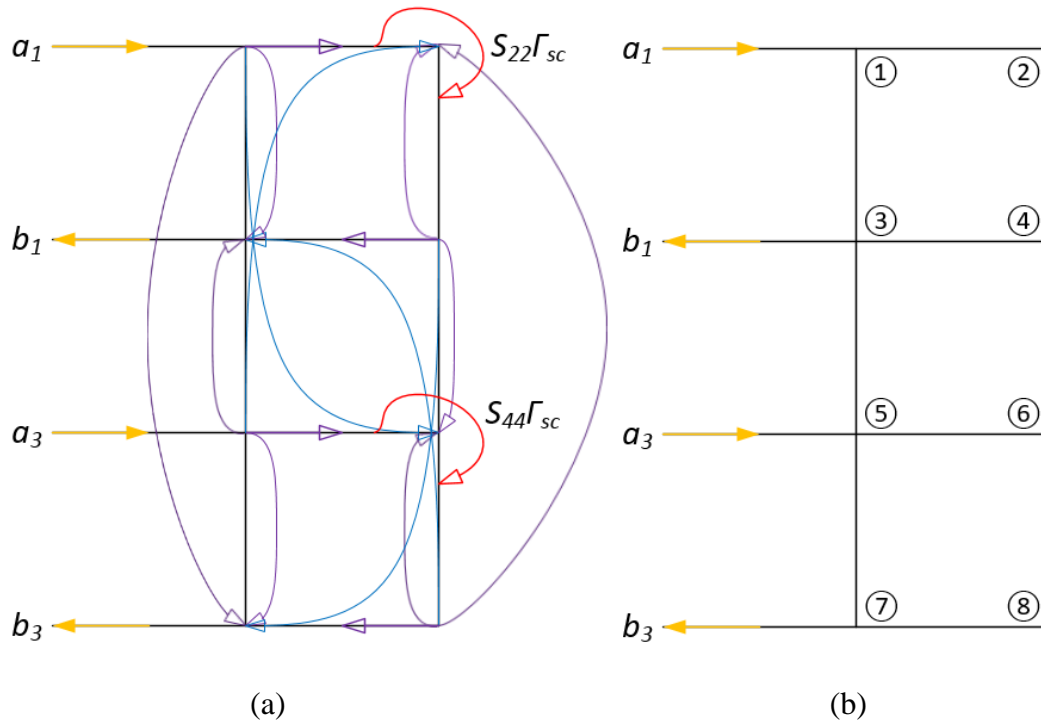
Fig. 6.42 (a) Signal flow graph for the analysis of $[S_{11}'\ S_{13}';\ S_{31}'\ S_{33}']$ and (b) numbering of the nodes in (a).

To write $S_{11}{}^o=b_1/a_1$ directly is still difficult, so an additional step is necessary, i.e., to match Port 3 (let $\Gamma_o=0$) and then solve the 2-port network $[S_{11}'\ S_{13}';\ S_{31}'\ S_{33}']$ first, as shown in Fig. 6.42.

For S_{11}', the signal flow from Node 1 to 3 may be 1→3, 1→2→4→3, and 1→6→8→3. The above three is the simplest. Further, 1243 and 1683 develop 1→2→4→6→8→3, 1→2→4→6→8→2→4→3, 1→2→4→6→8→2→4→6→8→3, 1→2→4→6→8→2→4→6→8→2→4→3, ... and 1→6→8→2→4→3, 1→6→8→2→4→6→8→3, 1→6→8→2→4→6→8→2→4→3, 1→6→8→2→4→6→8→2→4→6→8→3, ...

We can write the expression of S_{11}' using the sum of an infinitely proportional sequence:

$$S_{11}{}' = S_{11} + \frac{\dfrac{S_{21}{}^2\Gamma_{sc}}{1-S_{22}\Gamma_{sc}}}{1-\dfrac{S_{42}{}^2\Gamma_{sc}{}^2}{(1-S_{44}\Gamma_{sc})(1-S_{22}\Gamma_{sc})}} + \frac{\dfrac{S_{21}S_{42}S_{14}\Gamma_{sc}{}^2}{(1-S_{22}\Gamma_{sc})(1-S_{44}\Gamma_{sc})}}{1-\dfrac{S_{42}{}^2\Gamma_{sc}{}^2}{(1-S_{22}\Gamma_{sc})(1-S_{44}\Gamma_{sc})}}$$
$$+ \frac{\dfrac{S_{41}{}^2\Gamma_{sc}}{1-S_{44}\Gamma_{sc}}}{1-\dfrac{S_{24}{}^2\Gamma_{sc}{}^2}{(1-S_{22}\Gamma_{sc})(1-S_{44}\Gamma_{sc})}} + \frac{\dfrac{S_{41}S_{24}S_{12}\Gamma_{sc}{}^2}{(1-S_{44}\Gamma_{sc})(1-S_{22}\Gamma_{sc})}}{1-\dfrac{S_{42}{}^2\Gamma_{sc}{}^2}{(1-S_{44}\Gamma_{sc})(1-S_{22}\Gamma_{sc})}} \tag{6.57}$$

For S_{33}', the signal flow from Node 5 to 7 may be 5→7, 5→2→4→7, 5→2→4→6→8→7, 5→2→4→6→8→2→4→7, 5→2→4→6→8→2→4→6→8→7,

$5\rightarrow2\rightarrow4\rightarrow6\rightarrow8\rightarrow2\rightarrow4\rightarrow6\rightarrow8\rightarrow2\rightarrow4\rightarrow7$, …… and $5\rightarrow6\rightarrow8\rightarrow7$, $5\rightarrow6\rightarrow8\rightarrow2\rightarrow4\rightarrow7$,

$5\rightarrow6\rightarrow8\rightarrow2\rightarrow4\rightarrow6\rightarrow8\rightarrow7$, $5\rightarrow6\rightarrow8\rightarrow2\rightarrow4\rightarrow6\rightarrow8\rightarrow2\rightarrow4\rightarrow7$,

$5\rightarrow6\rightarrow8\rightarrow2\rightarrow4\rightarrow6\rightarrow8\rightarrow2\rightarrow4\rightarrow6\rightarrow8\rightarrow7$, …… Similarly, S_{33}' is in the form of

$$S_{33}' = S_{33} + \frac{\dfrac{S_{23}{}^{2}\Gamma_{sc}}{1-S_{22}\Gamma_{sc}}}{1-\dfrac{S_{42}{}^{2}\Gamma_{sc}{}^{2}}{(1-S_{44}\Gamma_{sc})(1-S_{22}\Gamma_{sc})}} + \frac{\dfrac{S_{23}S_{42}S_{34}\Gamma_{sc}{}^{2}}{(1-S_{22}\Gamma_{sc})(1-S_{44}\Gamma_{sc})}}{1-\dfrac{S_{42}{}^{2}\Gamma_{sc}{}^{2}}{(1-S_{22}\Gamma_{sc})(1-S_{44}\Gamma_{sc})}}$$

$$+ \frac{\dfrac{S_{43}{}^{2}\Gamma_{sc}}{1-S_{44}\Gamma_{sc}}}{1-\dfrac{S_{24}{}^{2}\Gamma_{sc}{}^{2}}{(1-S_{22}\Gamma_{sc})(1-S_{44}\Gamma_{sc})}} + \frac{\dfrac{S_{34}S_{24}S_{23}\Gamma_{sc}{}^{2}}{(1-S_{44}\Gamma_{sc})(1-S_{22}\Gamma_{sc})}}{1-\dfrac{S_{42}{}^{2}\Gamma_{sc}{}^{2}}{(1-S_{44}\Gamma_{sc})(1-S_{22}\Gamma_{sc})}} \qquad (6.58)$$

For S_{31}', the signal flow from Node 1 to 7 may be $1\rightarrow7$, $1\rightarrow2\rightarrow4\rightarrow7$,

$1\rightarrow2\rightarrow4\rightarrow6\rightarrow8\rightarrow7$, $1\rightarrow2\rightarrow4\rightarrow6\rightarrow8\rightarrow2\rightarrow4\rightarrow7$, $1\rightarrow2\rightarrow4\rightarrow6\rightarrow8\rightarrow2\rightarrow4\rightarrow6\rightarrow8\rightarrow7$,

$1\rightarrow2\rightarrow4\rightarrow6\rightarrow8\rightarrow2\rightarrow4\rightarrow6\rightarrow8\rightarrow2\rightarrow4\rightarrow7$, …… and $1\rightarrow6\rightarrow8\rightarrow7$, $1\rightarrow6\rightarrow8\rightarrow2\rightarrow4\rightarrow7$,

$1\rightarrow6\rightarrow8\rightarrow2\rightarrow4\rightarrow6\rightarrow8\rightarrow7$, $1\rightarrow6\rightarrow8\rightarrow2\rightarrow4\rightarrow6\rightarrow8\rightarrow2\rightarrow4\rightarrow7$,

$1\rightarrow6\rightarrow8\rightarrow2\rightarrow4\rightarrow6\rightarrow8\rightarrow2\rightarrow4\rightarrow6\rightarrow8\rightarrow7$, …… Similarly, S_{31}' is in the form of

$$S_{31}' = S_{13}' = S_{31} + \frac{\dfrac{S_{21}S_{32}\Gamma_{sc}}{1-S_{22}\Gamma_{sc}}}{1-\dfrac{S_{42}{}^{2}\Gamma_{sc}{}^{2}}{(1-S_{44}\Gamma_{sc})(1-S_{22}\Gamma_{sc})}} + \frac{\dfrac{S_{21}S_{42}S_{34}\Gamma_{sc}{}^{2}}{(1-S_{22}\Gamma_{sc})(1-S_{44}\Gamma_{sc})}}{1-\dfrac{S_{42}{}^{2}\Gamma_{sc}{}^{2}}{(1-S_{22}\Gamma_{sc})(1-S_{44}\Gamma_{sc})}}$$

$$+ \frac{\dfrac{S_{41}S_{34}\Gamma_{sc}}{1-S_{44}\Gamma_{sc}}}{1-\dfrac{S_{24}{}^{2}\Gamma_{sc}{}^{2}}{(1-S_{22}\Gamma_{sc})(1-S_{44}\Gamma_{sc})}} + \frac{\dfrac{S_{41}S_{24}S_{32}\Gamma_{sc}{}^{2}}{(1-S_{44}\Gamma_{sc})(1-S_{22}\Gamma_{sc})}}{1-\dfrac{S_{42}{}^{2}\Gamma_{sc}{}^{2}}{(1-S_{44}\Gamma_{sc})(1-S_{22}\Gamma_{sc})}} \qquad (6.59)$$

Now we can draw the signal flow of the 2-port network $[S_{11}'\ S_{13}';\ S_{31}'\ S_{33}']$ to solve $S_{11}{}^{o}$. It is obtained by eq. (6.60). Using the similar steps, $S_{11}{}^{e}$ can be also solved.

$$S_{11}{}^o = S_{11}{}' + \frac{S_{31}{}' S_{13}{}' \Gamma_o}{1 - S_{33}{}' \Gamma_o} \qquad (6.60)$$
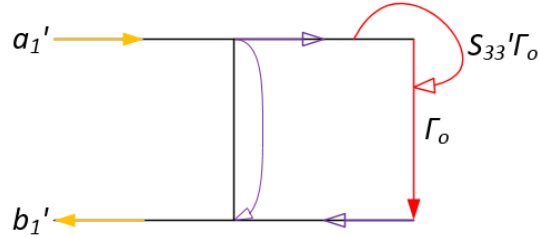
Fig. 6.43 Signal flow graph of the network $[S_{11}{}'\ S_{13}{}';\ S_{31}{}'\ S_{33}{}']$.
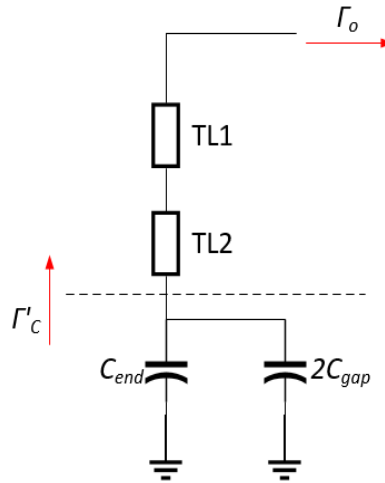
Fig. 6.44 1-port network decomposed from Fig. 6.40(a) for Γ_o.

The rest of the work is to solve the reflection coefficient Γ_o and Γ_e in Fig. 6.40 (a) and (b). Taking Γ_o for example, it is S_{11} of the 1-port network in Fig. 6.44, which is decomposed from Fig. 6.40(a). The 2-port S-parameters $[S_{11}"\ S_{12}";\ S_{21}"\ S_{22}"]$ of the transmission line TL1 and TL2 in series in Fig. 6.44 can be easily solved. The calculations of conductor loss and 45° mitered bend can be found in [6.47], [6.48]. Then,

S_{11} of the network, i.e., Γ_o, is expressed as eq. (6.61). The similar process is also used to obtain Γ_e.

$$\Gamma_o = S_{11}'' + \frac{S_{21}'' S_{12}'' \Gamma_C'}{1 - S_{22}'' \Gamma_C'} \tag{6.61}$$

where the reflection coefficient Γ_C' is

$$\Gamma_C' = \frac{1 - Z_0 j\omega(C_{end} + 2C_{gap})}{1 - Z_0 j\omega(C_{end} + 2C_{gap})} \quad . \tag{6.62}$$

For the SRR in Fig. 6.14(a), the calculated $|S_{21}|$ from 1 GHz to 12 GHz loading 0.1 M glucose-water solution using the proposed analytical model is shown in Fig. 6.45. The frequency-dependent complex permittivity of the solution [6.49] is used to calculate eq. (6.45). To analyze the respective resonant frequencies of odd-mode and even-mode, $|S_{11}^o|$ for odd-mode and $|S_{11}^e|$ for even-mode are also demonstrated, respectively, in Fig. 6.46 (a) and (b). We can see that 1st and 2nd resonant frequencies of the odd-mode, i.e., 2.68 GHz and 7.99 GHz, correspond to 1st and 3rd resonant frequencies of the complete SRR, i.e., 2.54 GHz and 7.54 GHz as shown in Fig. 6.45, whereas 1st and 2nd resonant frequencies of the even-mode, i.e., 5.08 GHz and 10.99 GHz, correspond to 2nd and 4th resonant frequencies of the complete SRR, i.e., 4.77 GHz and 9.90 GHz. The deviations are caused since only half of full length is calculated for $|S_{11}^o|$ and $|S_{11}^e|$, which is a requirement of the even-odd mode analysis technique [6.35]. It is also observed that the values at these frequencies for the combined $|S_{21}|$ are different from the single $|S_{11}^o|$ and $|S_{11}^e|$, due to the combination calculation in eq. (6.56).
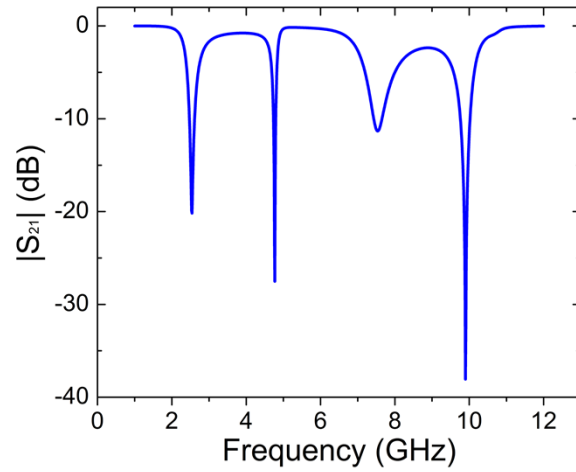
Fig. 6.45 Calculated $|S_{21}|$ from 1 GHz to 12 GHz loading 0.1 M glucose-water solution.

(a)   (b)
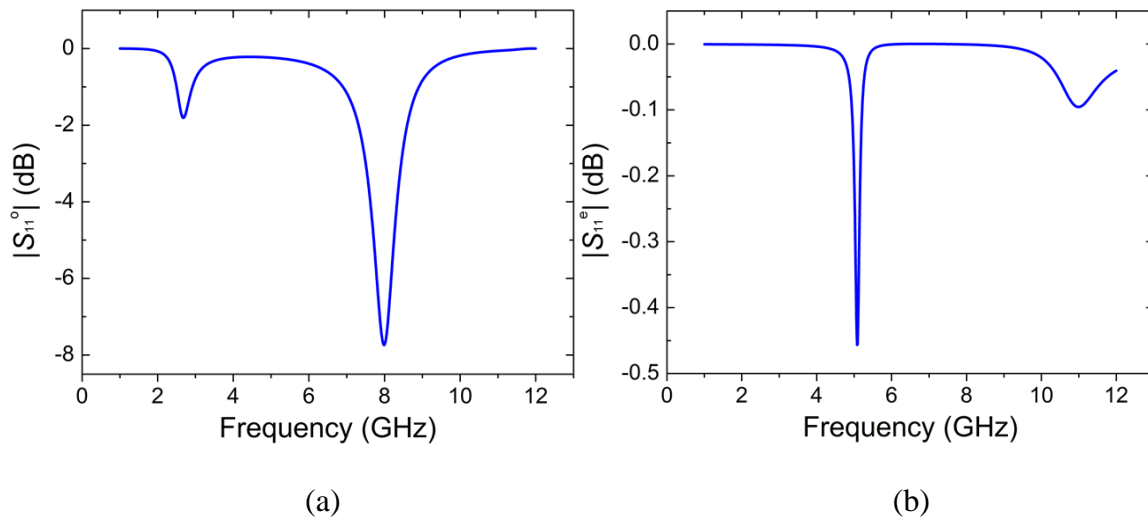
Fig. 6.46 (a) $|S_{11}^{o}|$ for the odd-mode and (b) $|S_{11}^{e}|$ for the even-mode.

6.5 Complex Permittivity Extraction of GUV Membrane

In Fig. 6.45, 1st frequency locates at 2.54 GHz with a $|S_{21}|$ of ~-20.17 dB, much lower than the measured ~-4.51 dB in Fig. 6.20(a), implying that the proposed coupled-line model has a stronger coupling between two adjacent MLs. The same thing also

affects other resonant frequencies. The reason is that the calculation of the mutual-capacitance coefficients c_{31} for two adjacent asymmetric lines uses the coplanar stripline (CPS)-based conformal mapping [6.38], but it is unlike two coplanar MLs of the SRR. For the CPS, almost all electric field streamlines emitted from an electrode terminate at another one; for two adjacent MLs of the SRR, a lot of electric field streamlines emitted from an electrode terminate at the back conductor [6.38]. So the calculated c_{31} is larger than what it should be. Moreover, the proposed model is derived based on the assumption of TEM propagation, which has to be used to meet the prerequisite of eq. (6.4), but it is only strictly satisfied in a homogeneous medium. Based on this assumption, the field distribution at any transverse plane perpendicular to z-direction in Fig. 6.33 can be treated as a linear combination of the proposed two fundamental TEM-modes, i.e., π Mode and c Mode in Section 6.4.1. Then the derivations in Section 6.4.1 can be further performed for a relatively simple and intuitive analysis of the SRR.

To extract the permittivity of the measured GUV membranes using the proposed model, some additional revisions are required. According to the above discussion, c_{31} is the main target. For s=3.5 μm (the spacing between two adjacent MLs), c_{31} is calculated to be ~95.60 pF, demonstrating a strong coupling in Fig. 6.45. If it is decreased to ~19.11 pF, the $|S_{21}|$ at 1st resonant frequency is close to the measured value, i.e., ~-4.51 dB. The minor frequency error is eliminated by decreasing the length of the coupled line. Then the corrected $|S_{21}|$ from 1 GHz to 12 GHz is re-drawn in Fig. 6.47(a). But, 2nd resonant frequency shifts to at 8.1 GHz with a $|S_{21}|$ of -1.53 dB, therefore. So the above adjustment is more suitable for permittivity extraction at 2.7 GHz, and c_{31} and the length of the

coupled line need to be adjusted again when extracting permittivity at 7.9 GHz. Figure 6.47(b) also demonstrates the corrected $|S_{21}|$ from 1 GHz to 12 GHz using a c_{31} of ~28.90 pF, which agrees with the measured $|S_{21}|$ at 7.9 GHz.

To verify the proposed model, it is necessary to measure another MUT with known permittivity and compare it with the calculated result. Replacing 0.1 M glucose-water solution with air ($\varepsilon_{air}{\approx}1{-}j0$), the calculated $|S_{21}|$s using 19.11 pF and 28.90 pF as c_{31}, respectively, for good agreement at 2.7 GHz and 7.9 GHz, are compared with the measured data together in Table 6.8. The relative errors at 2.7 GHz and 7.9 GHz from Table 6.8 are 1.00% and 1.90%, respectively, suggesting that the proposed model can obtain an accurate permittivity of MUT. It is worth noting that the above comparison is made for a wide permittivity range (from the solution to the air). In fact, for the minute permittivity change without and with a GUV membrane, the proposed model is expected to obtain a lower relative error.

(a)   (b)
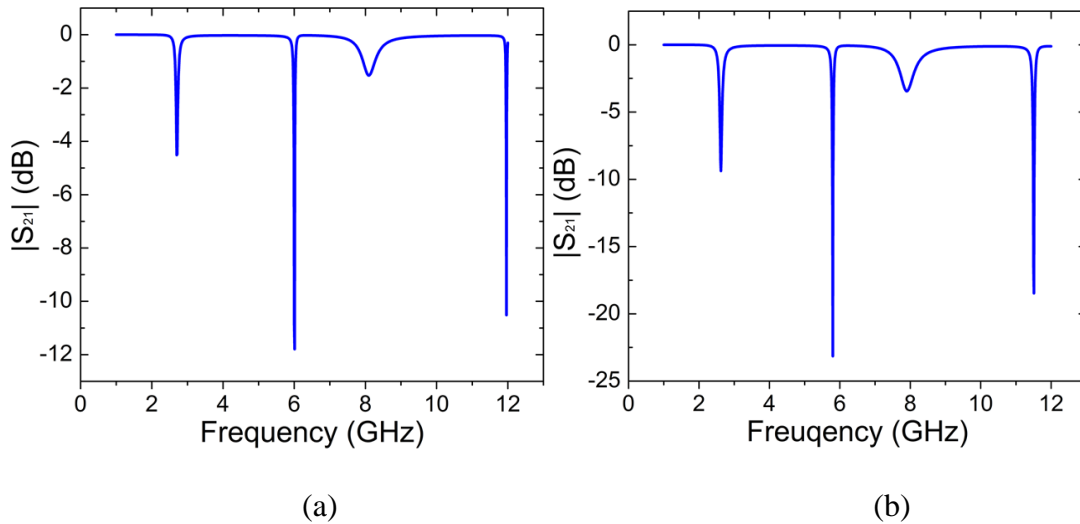
Fig. 6.47 Corrected $|S_{21}|$ from 1 GHz to 12 GHz loading 0.1 M glucose-water solution demonstrating a good agreement with the measurement at (a) 2.7 GHz and at (b) 7.9 GHz.

TABLE 6.8
COMPARISON BETWEEN THE CALCULATED AND THE MEASURED
$|S_{21}|$S USING AIR AS A MUT AT 2.7 GHz AND 7.9 GHz

Frequency	Calculated $|S_{21}|$	Measured $|S_{21}|$	Relative error[*]
2.7 GHz	-0.02526 dB	0.06129 dB[#]	1.00%
7.9 GHz	-0.04479 dB	-0.2079 dB	1.90%

[*]Relative error=|(Calculated-Measured)/Measured| ×100%, where the data is in linear format, rather than dB, for the calculation. [#]The value is slightly larger than 0 dB, caused by the calibration error of VNA.

Until this step, however, the additional phase shift induced by the left and right MLs in Fig. 6.32 is not taken into account. In Fig. 6.47, the S_{21} at 1st resonant frequency 2.7 GHz is 315.89°, which should be corrected to the measured angle, i.e., 104.01°. Then the data at 2.7 GHz in Table 6.4 to 6.6 can be transformed to corresponding complex permittivities. The same procedures are also done at 7.9 GHz. These extracted permittivities are listed in Table 6.9 to 6.11. In the transformation, the width of the flatten GUV membrane (along W direction in Fig. 6.37) w_{GUV} is selected as 25 μm. But, according to the discussion in Section 6.3, the possible w_{GUV} value ranges from 20.8 μm to 25 μm. For other possible choices of w_{GUV}, the extracted complex permittivities may demonstrate a slight deviation. Figure 6.48 shows a complete calculation flow graph for GUV membrane complex permittivity using the proposed model.

TABLE 6.9
EXTRACTED COMPLEX PERMITTIVITY OF THE SM GUVS IN TABLE 6.4

#	2.7 GHz μ=73.49-j2.27 σ_{real}=0.47, σ_{imag}=1.44	#	7.9 GHz μ=63.20-j3.28 σ_{real}=1.37, σ_{imag}=1.31
Fig. 6.24(a)	74.39-j3.74	Fig. 6.24(b)	66.10-j5.22
1	73.20-j1.66	1	62.63-j3.41
2	72.96-j0.83	2	63.09-j1.61
3	72.97-j1.14	3	63.10-j2.57
4	73.39-j2.94	4	63.94-j3.05
5	73.66-j3.01	5	63.63-j3.57
6	73.48-j1.43	6	62.16-j0.93
7	74.05-j4.66	7	60.71-j4.48
8	73.13-j0.13	8	63.15-j4.38
9	73.67-j3.11	9	63.53-j3.57

TABLE 6.10
EXTRACTED COMPLEX PERMITTIVITY OF THE POPC GUVS IN TABLE 6.5

#	2.7 GHz μ=73.64-j6.13 σ_{real}=0.61, σ_{imag}=0.79	#	7.9 GHz μ=63.97-j16.46 σ_{real}=1.23, σ_{imag}=2.66
Fig. 6.25(a)	72.67-j4.83	Fig. 6.25(b)	62.47-j12.31
1	74.33-j6.92	1	65.26-j19.33
2	73.40-j5.74	2	62.24-j13.16
3	73.11-j5.57	3	62.61-j13.70
4	73.20-j5.55	4	63.28-j14.98
5	74.33-j6.94	5	64.18-j17.19
6	73.28-j5.70	6	64.86-j18.73
7	73.68-j6.00	7	64.90-j18.06
8	74.46-j7.24	8	65.56-j18.21
9	73.93-j6.78	9	64.29-j18.95

TABLE 6.11
EXTRACTED COMPLEX PERMITTIVITY OF THE GUVS IN TABLE 6.6

#	Section *I*	Section *II*
(a)	72.62-j1.05	74.56-j5.11
(b)	72.81-j2.29	74.15-j5.03
(c)	73.68-j3.86	75.04-j6.90
(d)	63.99-j6.58	65.07-j17.37

Note: (a)-(c) at 2.7 GHz; (d) at 7.9 GHz.
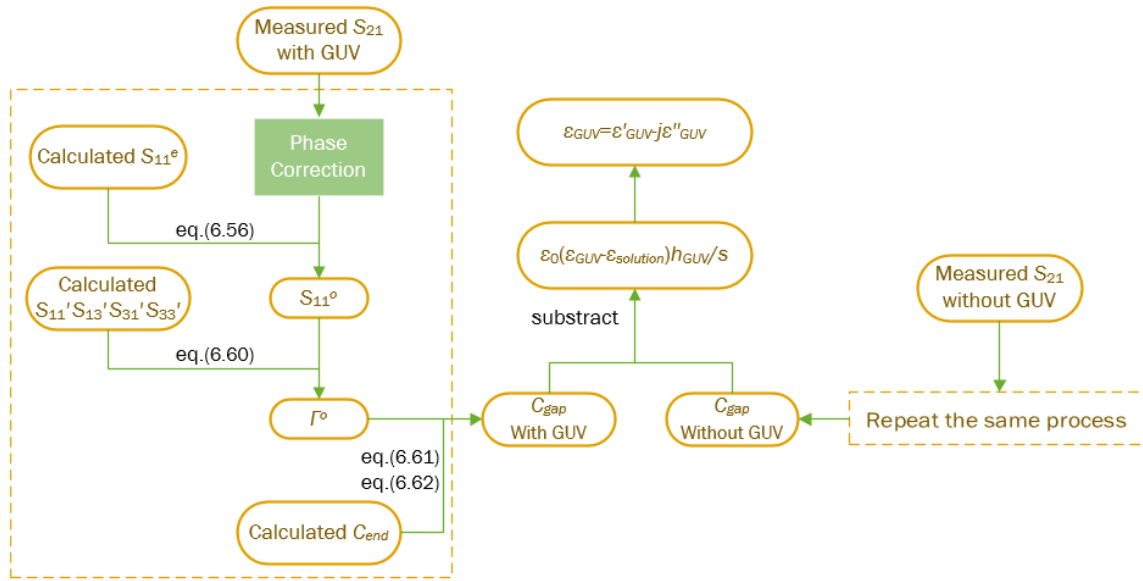
Fig. 6.48 Complete calculation flow graph for GUV membrane complex permittivity.

6.6 Discussions

According to Table 6.8 and 6.9, the PDFs of SM and POPC GUVs at 2.7 GHz and 7.9 GHz are drawn in Fig. 6.49. From Fig. 6.49 (a) and (c), the PDFs of the real component of SM and POPC GUVs highly overlap and only slightly shift a little, which suggests that their dipole moments are comparable. Figure 6.49(b) indicates that at 2.7 GHz, the imaginary relative permittivity of 86.6% SM GUVs ranges from 0.11 to 4.43, corresponding to $\pm 1.5\sigma$ away from the mean μ, but for 86.6% (μ-1.5σ, μ+1.5σ) POPC GUVs, it ranges from 4.95 to 7.32. From Fig. 6.49(d), at 7.9 GHz, the imaginary relative permittivity of 95.4% SM GUVs ranges from 0.66 to 5.90, corresponding to $\pm 2\sigma$ away from the mean μ, but for 95.4% (μ-2σ, μ+2σ) POPC GUVs, it ranges from 11.14 to 21.78. That means that the hydrated POPC membrane has larger dielectric loss than SM. The water-glucose-POPC system is able to absorb more microwave energy both at 2.7 GHz

144

and 7.9 GHz. It is probably caused by longer SM lipid molecules and corresponding thicker membrane. Moreover, from Fig. 6.50 [6.50], [6.51], POPC and SM have the same choline and phosphate molecules but different glycerol molecules, which may be responsible for the difference in the dielectric loss. The further investigation is required to explain this phenomenon.
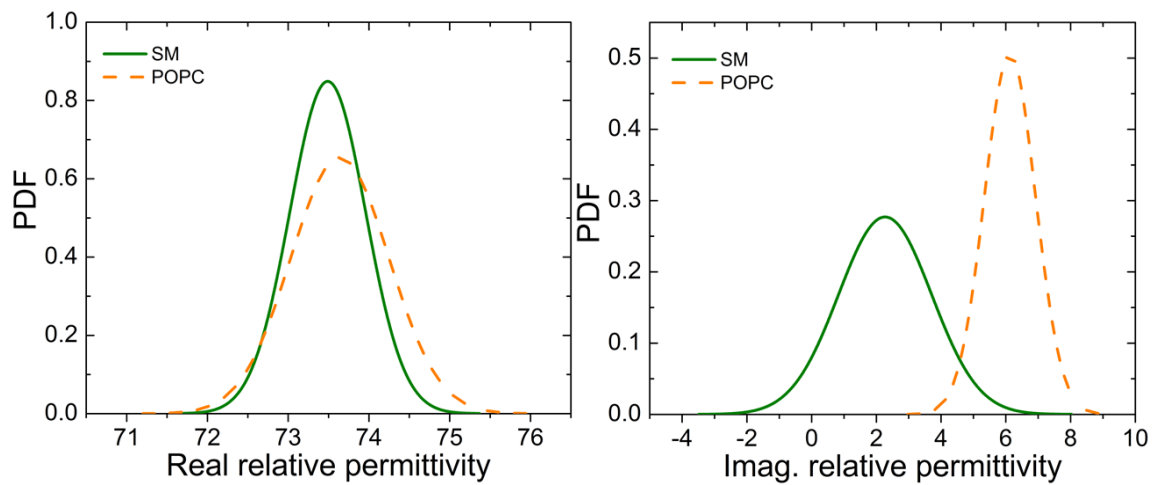
(a)

(b)
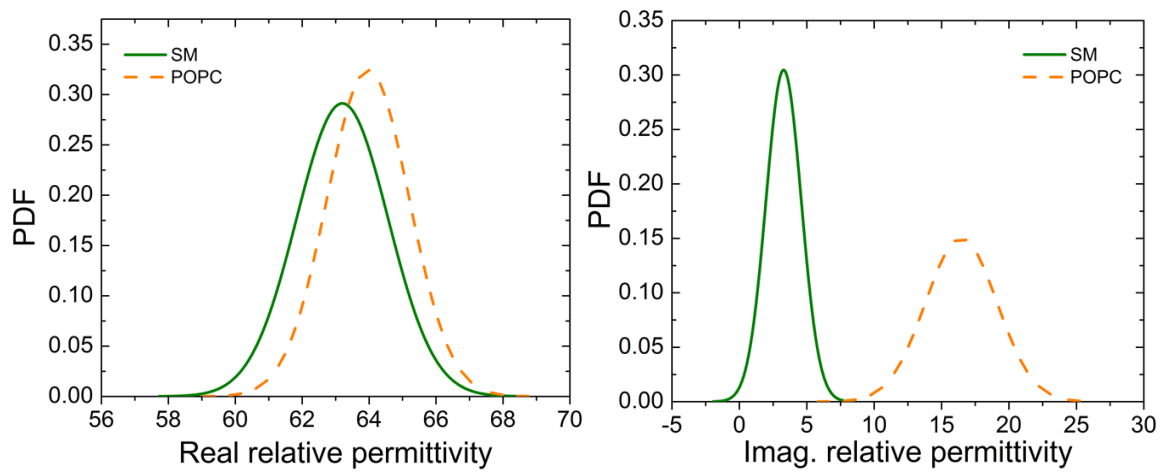
(c)

(d)

Fig. 6.49 PDFs for the real and imaginary relative permittivities of SM and POPC GUVs at (a)-(b) 2.7 GHz and at (c)-(d) 7.9 GHz.

(a)

(b)
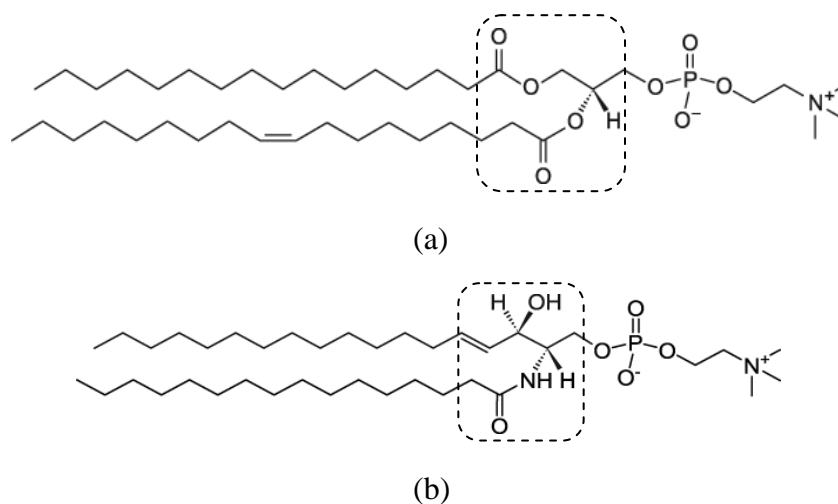
Fig. 6.50 Molecular structures of (a) 16:0-18:1 POPC [6.50] and (b) 16:0 SM [6.51]. Glycerol is enclosed by dashed box.

The obtained GUV membrane permittivity values in Fig. 6.49 are more than 10 times higher than that of the supported bilayers in air [6.52] and electrolyte [6.53] despite the fact that the lipid molecules used in these experiments are different and electrolyte reduces hydration water permittivity [6.54]. A possible reason is that the measured permittivity values in Fig. 6.49 are from lipid polarizations perpendicular to those in previous efforts. As shown in Fig. 6.15(a), the fields between the 500-nm wide split gap, $E_{\parallel}$, is parallel with the membrane surface plane while the fringing fields near the gap edge, $E_{\perp}$, is perpendicular to GUV membrane. But $E_{\parallel}$ is much stronger than $E_{\perp}$ and account for more than 90% of the electric field energy for GUV scanning. Thus, the lipid polarization

process for Fig. 6.49 is perpendicular to the process in scanning probe microscopy (SPM) efforts, i.e., Fig. 6.49 is for $\varepsilon_\parallel$ rather than $\varepsilon_\perp$ unlike that in Fig. 6.51 [6.53]. It is predicted that $\varepsilon_\parallel$ values are very high [6.55], much higher than $\varepsilon_\perp$, albeit the results are calculated at DC, not at GHz frequencies. Regardless, the proposed scanning technique provides a method to measure the permittivity values that are difficult to access by any of current technique. A second possible reason is data extraction uncertainty. To obtain GUV membrane permittivity values in Fig. 6.49, GUV membranes are assumed to be in contact with the smooth and flat electrode surfaces around the SRR split gap, as shown in Fig. 6.15(a). This assumption is questionable because there will be thin layers of liquids on electrode surface and GUV membrane outer surface, e.g. hydration water on GUV membrane. As a result, GUV membrane will be elevated above electrode surface by the liquid thin layers. It is estimated that a 100-nm elevation will result in a factor of 0.107 reduction of probing field intensity, as shown in the zoom-in figure of Fig. 6.15(a) and Fig. 6.15(b). As expected, the obtained GUV permittivity values (expectation μ) are lower, 73.17-j1.34 at 2.7GHz, 62.75-j0.65 at 7.9GHz for SM and 73.34-j5.66 at 2.7GHz, 63.61-j15.41 at 7.9 GHz for POPC. But the effects are not significant even though the exact GUV elevation height is still uncertain. Further complicating accurate data extraction are the uncertainties associated with the permittivity values of surface water and confined water, which are a subject of active investigation [6.56]-[6.59].

The spatial resolution of the proposed 1-D scanning is determined by the ~500 nm split gap. Engineering the split gap dimensions in both directions, a high resolution 2-D scanning can be achieved provided that measurement sensitivity is sufficient. The

scanning technique is intrinsically label-free even though fluorescent labels are used in this work for better visual guidance. The label-free characteristic is beneficial for various investigations since labels are known to affect membrane structures and functions [6.24], [6.25].
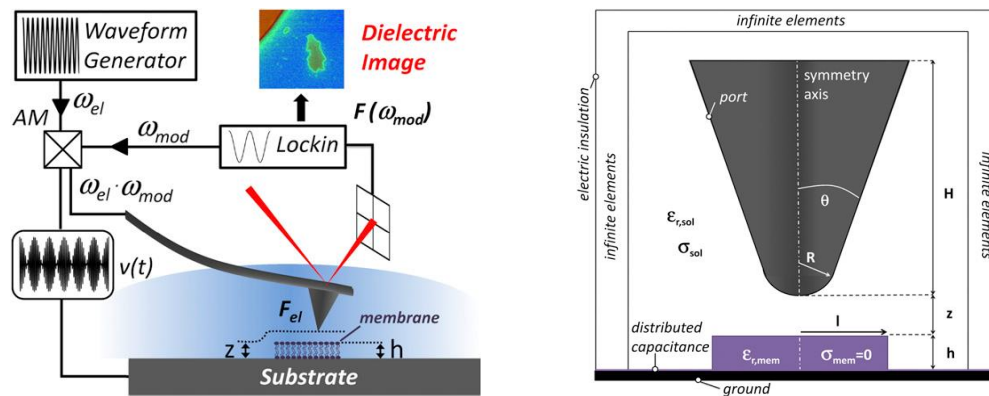
Fig. 6.51 (a) Electrostatic force microscopy setup and (b) AFM-tip for measuring local dielectric properties of materials in electrolyte solution [6.53].

References

[6.1] A. Pralle, P. Keller, E. -L. Florin, K. Simons, and J. Hörber, "Sphingolipid-cholesterol rafts diffuse as small entities in the plasma membrane of mammalian cells," *J. Cell Biol.*, vol. 148, no. 5, pp. 997-1008, Mar. 2000.

[6.2] K. Simons, and E. Ikonen, "Functional rafts in cell membranes," *Nature*, vol. 387, pp. 569-572, Jun. 1997.

[6.3] W. H. Binder, V. Barragan, and F. M. Menger, "Domains and rafts in lipid membranes," *Angew. Chem. Int. Ed.*, vol. 42, 5802-5827, Dec. 2003.

[6.4] R. A. Dick and V. M. Vogt, "Membrane interaction of retroviral Gag proteins," *Front. Microbiol.*, vol. 5, pp. 1-11, Apr. 2014.

[6.5] J. B. Pendry, A. J. Holden, D. J. Robbins, and W. J. Stewart, "Magnetism from conductors and enhanced nonlinear phenomena," *IEEE Trans. Microw. Theory Techn.*, vol. 47, no. 11, pp. 2075-2084, Nov. 1999.

[6.6] D. R. Smith, W. J. Padilla, D. C. Vier, S. C. Nemat-Nasser, and S. Schultz, "Composite medium with simultaneously negative permeability and permittivity," *Phys. Rev. Lett.*, vol. 84, no. 18, pp. 4184-4187, May 2000.

[6.7] RT/duroid® 5870 Laminates. Rogers Corporation, Rogers, CT, USA. [Online]. Available: https://www.rogerscorp.com/acs/products/31/RT-duroid-5870-Laminates.aspx

[6.8] R. Garg, I. Bahl, and M. Bozzi, *Microstrip Lines and Slotlines*, 3rd ed. Boston: ARTECH HOUSE, 2013, p. 4.

[6.9] D. M. Pozar, *Microwave Engineering*, 4th ed. New York: Wiley, 2012, pp. 272-274.

[6.10] J. Osterberg and P. Wang, " Two-stage radio-frequency interferometer sensors," *Appl. Phys. Lett.*, vol. 107, no. 17, pp. 172907, Oct. 2015.

[6.11] J. -S. Hong and M. J. Lancaster, *Microstrip Filters for RF/Microwave Applications*, John Wiley & Sons, 2001, pp. 89-92.

[6.12] Advanced Design System. Keysight Technologies, Inc., Santa Rosa, CA 95403, USA. [Online]. Available: http://www.keysight.com/en/pc-1297113/advanced-design-system-ads?cc=US&lc=eng

[6.13] J. Zhu, S. K. Ozdemir, Y. Xiao, L. Li, L. He, D. Chen and L. Yang. "On-chip single nanoparticle detection and sizing by mode splitting in an ultrahigh-Q microresonator, " *Nat. Photon.*, vol. 4, pp. 46-49, Jan. 2010.

[6.14] J. -L. Fraikin, T. Teesalu, C. M. McKenney, E. Ruoslahti and A. N. Cleland, "A high-throughput label-free nanoparticle analyser", *Nat. Nanotechnol.*, vol. 6, pp. 308-313, May 2011.

[6.15] J. C. Weaver, "Electroporation: a general phenomenon for manipulating cells and tissues," *IEEE Microw. Mag.*, vol. 51, no. 4, pp. 426-435, Apr. 1993.

[6.16] P. J. Canatella, J. F. Karr, J. A. Petros, and M. R. Prausnitz, "Quantitative study of electroporation-mediated molecular uptake and cell viability," *Biophys. J.*, vol. 80, no. 2, pp. 755-761, Feb. 2001.

[6.17] R. Dimova, K. A. Riske, S. Aranda, N. Bezlyepkina, R. L. Knorr, and R. Lipowsky, "Giant vesicles in electric fields," *Soft Matter*, vol. 3, pp. 817-827, May 2007.

[6.18] M. Pal and R. Ghatak, "A distinctive resonance: multiband bandpass filter design techniques using multimode resonators," *IEEE Microw. Mag.*, vol. 16, no. 11, pp. 36-55, Dec. 2015.

[6.19] J. Sor, Y. Qian, and T. Itoh, "Miniature low-loss CPW periodic structures for filter applications," *IEEE Trans. Microw. Theory Techn.*, vol. 49, no. 12, pp. 2336-2341, Dec. 2001.

[6.20] SU-8 GLM 1060. Gersteltec Sarl., Pully, Switzerland. [Online]. Available: http://www.gersteltec.ch/userfiles/1197841378.pdf

[6.21] SU-8 Developer. MicroChem, Corp., Westborough, MA, USA. [Online]. Available: http://www.microchem.com/pdf/SU-82000DataSheet2025thru2075Ver4.pdf

[6.22] SU-8 2075. MicroChem, Corp., Westborough, MA, USA. [Online]. Available: http://www.microchem.com/pdf/SU-82000DataSheet2025thru2075Ver4.pdf

[6.23] Electrical and Computer Engineering Cleanroom, 91 Technology Dr. Anderson, SC. 29625. [Online]. Available: https://www.clemson.edu/cecas/ece-clean-room/

[6.24] E. Sezgin, I. Levental, M. Grzybek, G. Schwarzmann, V. Mueller, A. Honigmann, V. N. Belov, C. Eggeling, Ü. Coskun, and K. Simons, "Partitioning, diffusion, and ligand binding of raft lipid analogs in model and cellular plasma membranes," *Biochim. Biophys. Acta*, vol. 1818, no. 7, pp. 1777-1784, Jul. 2012.

[6.25] A. Mashaghi, S. Mashaghi, I. Reviakine, R. M. Heeren, V. Sandoghdar, and M. Bonn, "Label-free characterization of biomembranes: from structure to dynamics," *Chem. Soc. Rev.*, vol. 43, pp. 887-900, Nov. 2014.

[6.26] Labview. National Instruments Corporation, Austin, TX 78759, USA. [Online]. Available: http://www.ni.com/labview/

[6.27] D. M. Pozar, *Microwave Engineering*, 4th ed. New York: Wiley, 2012, pp. 197-202.

[6.28] A. Yamada, S. Lee, P. Bassereau and C. N. Baroud, "Trapping and release of giant unilamellar vesicles in microfluidic wells, " *Soft Matter*, vol. 10, no. 32, pp. 5878-5885, Aug. 2014.

[6.29] E. T. Jaynes, *Probability Theory: The Logic of Science*, 1st ed. New York: Cambridge University Press, 2003, pp. 592-593.

[6.30] A. R. Honerkamp-Smith, F. G. Woodhouse, V. Kantsler, and R. E. Goldstein, "Membrane viscosity determined from shear-driven flow in giant vesicles," *Phys. Rev. Lett.*, vol. 111, pp. 038103, July 2013.

[6.31] C. Hofsäβ, E. Lindahl, and O. Edholm, "Molecular dynamics simulations of phospholipid bilayers with cholesterol," *Biophys. J.*, vol. 84, no. 4, pp. 2196-2206, Apr. 2003.

[6.32] J. D. Baena, J. Bonache, F. Mart ń, R. M. Sillero, F. Falcone, T. Lopetegi, M. A. G. Laso, J. Garc á–Garc á, I. Gil, M. F. Portillo, and M. Sorolla, "Equivalent-circuit models for split-ring resonators and complementary split-ring resonators coupled to planar transmission lines," *IEEE Trans. Microw. Theory Techn.*, vol. 53, no. 4, pp. 1451-1461, Apr. 2005.

[6.33] H. –J. Lee, H. –S. Lee, K. –H. Yoo, and J. –G. Yook, "DNA sensing using split-ring resonator alone at microwave regime," *Appl. Phys. Lett.*, vol. 108, no. 1, pp. 014908, Jul. 2010.

[6.34] C. –S. Lee and C. –L. Yang, "Single-compound complementary split-ring resonator for simultaneously measuring the permittivity and thickness of dual-layer dielectric materials," *IEEE Trans. Microw. Theory Techn.*, vol. 63, no. 6, pp. 2010-2023, Jun. 2015.

[6.35] J. Reed and G. J. Wheeler, "A Method of Analysis of Symmetrical Four-Port Networks," *IRE Trans. Microwave Theory Tech.*, vol. MTT-4, pp. 246-252, Oct. 1956.

[6.36] D. M. Pozar, *Microwave Engineering*, 4th ed. New York: Wiley, 2012, pp. 175-176.

[6.37] D. Pavlidis and H. L. Hartnagel, "The design and performance of three-line microstrip couplers," *IEEE Trans. Microw. Theory Techn.*, vol. MTT-24, no. 10, pp. 631-640, Oct. 1976.

[6.38] R. Garg and I. J. Bahl, "Characteristics of coupled microstriplines," *IEEE Trans. Microw. Theory Techn.*, vol. MTT-27, no. 7, pp. 700-705, Jul. 1979.

[6.39] G. Ghione, "A CAD-oriented analytical model for the losses of general asymmetric coplanar lines in hybrid and monolithic MICs," *IEEE Trans. Microwave Theory Tech.*, vol. 41, no. 9, pp. 1499-1510, Sep. 1993.

[6.40] V. K. Tripathi, and Y. K. Chin, "Analysis of the general nonsymmetrical directional coupler with arbitrary terminations," *Proc. Inst. Elect. Eng. —Microw., Antennas, Propag.*, vol. 129, no. 6, pt. H, pp. 360-362, Dec. 1982.

[6.41] M. Meada, "An analysis of gap in microstrip transmission lines," *IEEE Trans. Microw. Theory Techn.*, vol. MTT-20, no. 6, pp. 390-396, Jun. 1972.

[6.42] A. Farrar and A. T. Adams, "Matrix methods for microstrip three-dimensional problems," *IEEE Trans. Microw. Theory Techn.*, vol. MTT-20, no. 8, pp. 497-504, Aug. 1972.

[6.43] P. Benedek and P. Silvester, "Equivalent capacitances for microstrip gaps and steps," *IEEE Trans. Microw. Theory Techn.*, vol. MTT-20, no. 11, pp. 729-733, Nov. 1972.

[6.44] J. –S. Hong and M. J. Lancaster, *Microstrip Filters for RF/Microwave Applications*, 1st ed. New York: Wiley, 2001, pp. 89-92.

[6.45] E. Chen and S. Y. Chou, "Characteristics of coplanar transmission lines on multilayer substrates: modeling and experiments," *IEEE Trans. Microwave Theory Tech.*, vol. 45, no. 6, pp. 939-945, June 1997.

[6.46] D. M. Pozar, *Microwave Engineering*, 4th ed. New York: Wiley, 2012, pp. 194-197.

[6.47] R. A. Pucel, D. J. Masse, and C. P. Hartwig, "Losses in microstrip," *IEEE Trans. Microwave Theory Tech.*, vol. MTT-16, no. 6, pp. 342-350, June 1968.

[6.48] R. Kirschning, H. Jansen, and N. H. L. Koster, "Measurement and computer-aided modeling of microstrip discontinuities by an improved resonator method," *IEEE MTT-S Int. Microw. Symp.*, pp. 495-497, May 1983.

[6.49] H. Weingärtner, A. Knocks, S. Boresch, P. Höchtl, and O. Steinhauser, "Dielectric spectroscopy in aqueous solutions of oligosaccharides: experiment meets simulation," *J. Chem. Phys.*, vol. 115, no. 3, pp. 1463-1472, Jul. 2001.

[6.50] 16:0/18:1 PC. Avanti Polar Lipids, Inc., Alabaster, AL, USA. [Online]. Available: https://avantilipids.com/product/850457/

[6.51] 16:0 SM (d18:1/16:0). Avanti Polar Lipids, Inc., Alabaster, AL, USA. [Online]. Available: https://avantilipids.com/product/860584/

[6.52] L. Fumagalli, G. Ferrari, M. Sampietro, and G. Gomila, "Quantitative nanoscale dielectric microscopy of single-layer supported biomembranes," *Nano. Lett.*, vol. 9, no. 4, pp. 1604-1608, Mar. 2009.

[6.53] G. Gramse, A. Dols-Perez, M.A. Edwards, L. Fumagalli, and G. Gomila, "Nanoscale measurement of the dielectric constant of supported lipid bilayers in aqueous solutions with electrostatic force microscopy," *Biophys. J.*, vol. 104, no. 6, pp. 1257-1262, Mar. 2013.

[6.54] O. Teschke, G. Ceotto, and E. De Souza, "Interfacial water dielectric-permittivity-profile measurements using atomic force microscopy," *Phys. Rev. E*, vol. 64, no. 1, pp. 011605, Jul. 2001.

[6.55] H. A. Stern and S. E. Feller, "Calculation of the dielectric permittivity profile for a nonuniform system: application to a lipid bilayer simulation," *J. Chem. Phys.*, vol. 118, no. 7, pp. 3401-3412, Feb. 2003.

[6.56] P. Berntsen, C. Svanberg, and J. Swenson, "Interplay between hydration water and headgroup dynamics in lipid bilayers," *J. Phys. Chem. B*, vol. 115, no. 8, pp. 1825-1832, Feb. 2011.

[6.57] N. Nandi and B. Bagchi, "Anomalous dielectric relaxation of aqueous protein solutions," *J. Phys. Chem. A*, vol. 102, no. 43, pp. 8217-8221, Oct. 1998.

[6.58] D. A. Cherepanov, B. A. Feniouk, W. Junge, and A. Y. Mulkidjanian, "Low dielectric permittivity of water at the membrane interface: effect on the energy coupling mechanism in biological membranes," *Biophys. J.*, vol. 85, no. 2, pp. 1307-1316, Aug. 2003.

[6.59] S. Senapati and A. Chandra, "Dielectric constant of water confined in a nanocavity," *J. Phys. Chem. B*, vol. 105, no. 22, pp. 5106-5109, May 2001.

CHAPTER SEVEN

CONCULSION

In Chapter Two, it is demonstrated that the use of tunable attenuators and phase shifters for an interference-based RF sensor provides a simple and effective approach to build tunable and highly sensitive RF sensors. The obtained Q_{eff}, i.e., $\sim 3.8 \times 10^6$, is an order of magnitude higher than that of any previously published results. Lossy materials do not significantly reduce the achievable Q values. Thus the sensors are uniquely suited for biochemical material detection and analysis.

In Chapter Three, the mathematical models for extracting quantitative MUT properties from scattering parameters are introduced for commonly used CPW, GCPW, and ML sensing structures. Microfluidic channels are also included in the considerations. Furthermore, a quadrature-hybrid based interferometer is demonstrated to measure the glucose-water solution at a concentration level that is 10 times lower than the previous publication [7.1]. DNA solutions at a concentration level of 10 ng/mL are also measured with ~ 1 nL MUT volume. The demonstrated RF sensitivity is close to the reported highest result so far [7.2]. Composition analysis of ternary mixtures is also demonstrated through high-sensitivity measurements with a power divider based system. These results show that the proposed interferometers have wide application potentials in many scientific and technological areas.

In Chapter Four, it is demonstrated that infusing or withdrawal liquid to or from a well can achieve high resolution attenuation tuning. The obtained Q_{eff} of the interferometer is up to $\sim 1 \times 10^8$. When MUT sample is used, the automatic tuning process

154

also self-calibrates the measurement system and yields MUT permittivity values. Methanol-water solution is measured down to 5×10^{-5} mole fraction concentration level, which is 100 times lower than that in [7.3].

In Chapter Five, an interferometer based RF sensor with 100 nm slotline is presented. The sensor is highly sensitive and tunable in both operating frequency and sensitivity. Models are established and verified to obtain the RF properties of particles in carrier solution from measured scattering parameters. GUVs with different molecular compositions are synthesized, tested and analyzed with the sensor. The results show that the sensor can detect and scan GUVs at multiple frequency points, and the average dielectric properties of the GUV particles extracted with the two models agree with each other reasonably well.

In Chapter Six, the SRR provides strong microwave probing fields near its split gap for GUV membrane dielectric property 1-D scanning. It is shown that floating SM and POPC lipid bilayers have significantly different dielectric properties. The properties also depend on measurement frequencies. Thus, GUV domains, which are mainly formed with different lipid molecules, are also clearly identified from microwave scanning. The obtained GUV dielectric property values, based on algorithms developed for the scanning technique, are much larger than those obtained from other techniques. Nevertheless, the permittivity is from molecular polarizations parallel to GUV surface. Currently, there is no other technique that can probe such polarizations. Further investigation is needed to clarify the accuracy of the obtained permittivity values, increase scanning resolutions, analyze membrane dynamics, and determine membrane molecular compositions.

References

[7.1] M. Hofmann, G. Fischer, R. Weigel, and D. Kissinger, "Microwave-based noninvasive concentration measurements for biomedical applications," *IEEE Trans. Microwave Theory and Techn.*, vol. 61, no. 5, pp. 2195-2204, May 2013.

[7.2] I. F. Cheng, S. Senapati, X. Cheng, S. Basuray, H.-C. Chang, and H.-C. Chang, "A rapid field-use assay for mismatch number and location of hybridized DNAs," *Lab Chip*, vol. 10, no. 7, pp. 828-831, Feb. 2010.

[7.3] T. Sato, A. Chiba, and R. Nozaki, "Hydrophobic hydration and molecular association in methanol–water mixtures studied by microwave dielectric analysis," *J. Chem. Phys.*, vol. 112, no. 6, pp. 2924-2932, Feb. 2000.

APPENDICES

Appendix A

Processing of Uncalibrated *S*-parameters

Figure A1 demonstrates the Block diagram of a vector network analyzer (VNA) measurement of a two-port device. The matrix $[A^m B^m C^m D^m]$ is what the VNA records in its memory. But it is subject to the interference from the error box $[ABCD]$. So the measured $[A^m B^m C^m D^m]$ versus the realistic $[A'B'C'D']$ of a device under test (DUT) is expressed as

$$\begin{bmatrix} A^m & B^m \\ C^m & D^m \end{bmatrix} = \begin{bmatrix} A & B \\ C & D \end{bmatrix}\begin{bmatrix} A' & B' \\ C' & D' \end{bmatrix}\begin{bmatrix} D & B \\ C & A \end{bmatrix} \qquad (A.1)$$

$$\text{or} \quad \begin{bmatrix} A' & B' \\ C' & D' \end{bmatrix} = \begin{bmatrix} A & B \\ C & D \end{bmatrix}^{-1}\begin{bmatrix} A^m & B^m \\ C^m & D^m \end{bmatrix}\begin{bmatrix} D & B \\ C & A \end{bmatrix}^{-1} \qquad (A.2)$$
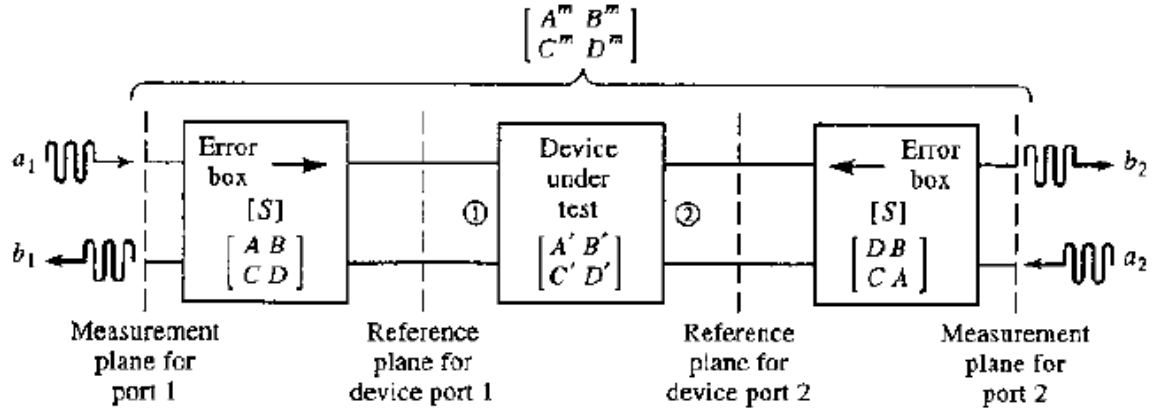

Fig. A1 Block diagram of a network analyzer measurement of a two-port device [A.1].

For the SRR with 0.1 M glucose-water solution, the measured data before calibration corresponds to $[A^m B^m C^m D^m]$, and the measured data after calibration corresponds to $[A'B'C'D']$. Using $[A^m B^m C^m D^m]$ and $[A'B'C'D']$, the error matrix at a selected frequency, e.g., 2.7 GHz or 7.9 GHz can be solved, respectively. Next, applying eq. (A.2) with the

uncalibrated measurement data and the error box, the calibrated [$A'B'C'D'$] for MUT can be

obtained, which is then transformed to S-parameters [A.2].

References

[A.1] D. M. Pozar, *Microwave Engineering*, 4th ed. New York: Wiley, 2012, pp. 197-202.

[A.2] D. M. Pozar, *Microwave Engineering*, 4th ed. New York: Wiley, 2012, p. 192.

Appendix B

Electric Field Distribution around the Split

The electric field (EF) distribution can be drawn using the equations in [B.1], [B.2]. For the EF above the substrate, they are

$$x = \frac{a \sin \beta \sqrt{1 - k'^2 \sin^2 \alpha}}{\cos^2 \alpha + k^2 \sin^2 \beta \sin^2 \alpha} \qquad (B.1)$$

and

$$y = \frac{a \sin \alpha \sqrt{1 - k^2 \sin^2 \beta}}{\cos^2 \alpha + k^2 \sin^2 \beta \sin^2 \alpha} \qquad (B.2)$$

For the EF inside the substrate, they are

$$x = \frac{h}{2\pi} \ln \frac{(1+A)^2 + B^2}{(1-A)^2 + B^2} \qquad (B.3)$$

and

$$y = \frac{h}{\pi} \arctan \frac{2B}{1 - A^2 - B^2} \qquad (B.4)$$

where all definitions of parameters in (B.1)-(B.4) can be found in the reference.

Although the target of these equations is the conductor-backed coplanar waveguides, they are still applicable around an enough small split. For Figs. 6.37 and 6.38, the parameters a and b are determined so that the split is from 1.0000×10^{-3} m to 1.0005×10^{-3} m along the horizontal direction.

References

[B.1] M. Gillick, I. D. Robertson, and J. S. Joshi, "An analytical method for direct calculation of E & H-field patterns of conductor-backed coplanar waveguides," *IEEE Trans. Microwave Theory and Techn.*, vol. 41, no. 9, pp. 1606-1610, Sep. 1993.

[B.2] V. Khemka and S. Prasad, "Comments on "An Analytical Method for Direct Calculation of E- and H-Field Patterns of Conductor Backed Coplanar Waveguides","" *IEEE Trans. Microwave Theory and Techn.*, vol. 42, no. 9, pp. 1721-1722, Sep. 1994.